Discovering the Size Effects in Nanoporous Structures: Theoretical Analysis and Computational Investigation

A thesis submitted in fulfilment of the requirements for

the degree of Doctor of Philosophy

Dingjie Lu

Master of Science, University of Chinese Academy of Sciences

School of Engineering

College of Science, Engineering, and Health

RMIT University

April 2017

Declaration

I certify that except where due acknowledgement has been made, the work is that of the author alone; the work has not been submitted previously, in whole or in part, to qualify for any other academic award; the content of the thesis/project is the result of work which has been carried out since the official commencement date of the approved research program; any editorial work, paid or unpaid, carried out by a third party is acknowledged; and, ethics procedures and guidelines have been followed.

Dingjie Lu

28th April, 2017

Acknowledgements

I would like to take this opportunity to express my appreciation to all who have supported, inspired and expedited me to complete the study of my Ph.D.

First and foremost, I want to appreciate Dr. Shiwei Zhou, who is not only my supervisor but also my best friend for the unreserved support he has given to me in the past three and a half years. His seasoned guidance has inspiring me to keep exploring the unknown fields which looks normal superficially but is full of interest actually. He is an example for me to be a good researcher and a person of excellent personalities.

I am extremely thankful to Prof. Mike Xie for his advice, guidance, and constant encouragement which allow the accomplishment of my study. He is a respected predecessor in structural topology optimisation, and a kindly gentleman enlightening all students in the Centre for Innovative Structures and Materials as well. It has been an honor and a privilege to study in his group and I am forever in his debt for his guidance, motivation, and immense support. I am also extremely gratitude to Prof. Xiaodong Huang for his valuable suggestions, encouragement and hearty support in both work and life throughout my study. He is such a critical thinker and it is always pleasant and productive to discuss with him.

I would like to express my special appreciation to Prof. Qing Li at University of Sydney for his valuable suggestions, encouragement and detailed feedback for my publications.

My sincere thanks also go to Dr. Shanqing Xu, Dr. Jianhu Shen, Dr. Sen Lin and all members in the centre who shared their valuable research experience and provided precious suggestions and encouragements in the past memorable days. I would also like to express my deepest gratitude to my love, my soulmate, Miss Yangfan Li, who has been and always will be the power source of my life. I am the happiest man in the world because of your accompany. Thank you for your constant supporting and love and your indispensable efforts in my research and life for the past nine years.

My time at RMIT was enjoyable due to the help and guidance received throughout my candidature from the adminstrational staff of our school, Ms. Marlene Mannays, Mr. Michael Jacobi, Mr. Luke Weston. I am grateful for the time spent with my football buddies at Merri Park, especially Mark Close, for the relaxation between research work and many other people

and memories as well.

Last but not the least, I would like to thank my family: my parents and my sister for their support, confidence, and encouragement throughout my life.

Résumé

Dingjie Lu

Education

September 2013 - present

Ph.D. candidate in Civil Engineering RMIT University

September 2010 - July 2013

M.Sc. in Geotechnical Engineering University of Chinese Academy of Sciences

September 2006 - July 2010

B.Sc. in Hydropower Engineering Wuhan University

Publications

1. **Lu, Dingjie**, Yi Min Xie, Qing Li, Xiaodong Huang, and Shiwei Zhou. *"Towards Ultra-Stiff Materials: Surface Effects on Nanoporous Materials."* Applied Physics Letters 105, no. 10 (2014): 101903. http://dx.doi.org/10.1063/1.4895582.

2. **Lu, Dingjie**, Yi Min Xie, Qing Li, Xiaodong Huang, and Shiwei Zhou. *"Investigating Size Effects of Complex Nanostructures through Young-Laplace Equation and Finite Element Analysis."* Journal of Applied Physics 118, no. 20 (2015): 204301. http://dx.doi.org/10.1063/1.4935819.

3. **Lu, Dingjie**, Yi Min Xie, Qing Li, Xiaodong Huang, Yang Fan Li, and Shiwei Zhou. *"A Finite-Element Approach to Evaluating the Size Effects of Complex Nanostructures."* Royal Society Open Science 3, no. 12 (2016). http://dx.doi.org/10.1098/rsos.160625.

4. **Lu, Dingjie**, Yi Min Xie, Qing Li, Xiaodong Huang, and Shiwei Zhou. *"Size effect on arbitrary structures: a numerical analysis in terms of Young-Laplace equation."* ACCM2015. Brisbane, QLD, Australia.

5. **Lu, Dingjie**, Yi Min Xie, Qing Li, Xiaodong Huang, and Shiwei Zhou. *"The extended Timoshenko beam element in finite element analysis for the investigation of size effects."* ICCM2016. Berkeley, CA, USA

Contents

Abbreviations

2D	Two dimensional space
3D	Three dimensional space
BESO	Bidirectional evolutionary structural optimaztion
ESO	Evolutionary structural optimaztion
FEA	Finite element analysis
FEM	Finite element method
H-S bound	Hashin and Shtrikman bound
M/NEMS	micro- and nano- electrical and mechanical system
npAu	nano porous gold
PBC	Periodic boundary condition
PUC	Periodic unit cell
RUC	Representative unit cell
RVE	Representative volume element
SEM	Scanning electron microscope
SIMP	Solid Isotropic Material with Penalisation

Nomenclature

$(EI)^*$	The effective flexural sitffness
(h_1, h_2, h_3)	The curvilinear orthonormal basis vectors
$\alpha, \beta, \gamma, \zeta$	The micropolar moduli
$\mathbf{B}$	The strain displacement matrix
$\mathbf{K^e}$	The element stiffness matrix
$\mathbf{N}$	The interpolation matrix
$\delta\varepsilon$	The virtual strain
δU	The virtual displacement
δW_E	The total virtual external work
δW_I	The total virtual internal work
δW_{EC}	The conventional part of virtual external work
δW_{ES}	The surface effect part of virtual external work
δW_{IC}	The conventional part of virtual internal work
δW_{IS}	The surface effect part of virtual internal work
δ	The thickness of the surface layer of material
δ_{kl}	The Kronecker delta
γ	The shear angle of Timoshenko beam
κ	The curvature at a point of an interface
λ, μ	The Lame constant

ν	The Poisson's ration of the constituent material
∂V	The surface of the volume domian occupied by the solid
ϕ_k	The microrotation
ρ	The mass density of the porous or composite material
ρ_0	The mass density of the constituent material
σ^i	The conventional stress tensor in the inner side of an interface
σ^o	The conventional stress tensor in the outer side of an interface
σ_0	The residual stress
σ_{kl}	The conventional stress tensor
$\tau^s_{0\_\alpha\beta}$	The initial surface tension
τ	The nonlocal factor
$\tau^s_{\alpha\beta}$	The surface stress tensor
θ_z	The rotation angle of Timoshenko beam
$\triangle\sigma_{ij}$	The stress jump across the interface
$\varepsilon^s_{\alpha\beta}$	The surface strain tensor
A	The cross-sectional area of the beam
a	The internal characteristic length
b	The width of the a micro/nano beam
D	The diameter of a circular cross-sectional beam
E	The Young's modulus of the constituent material

E'	The Young's modulus of the surface layer
E^*	The effcctive Young's modulus of a structure
e_0	The constant for nonlocal theory
E_s	The surface stiffness of the surface layer
e_{klm}	The permutation symbol
F	The reaciton force
f^b	The body force
f^e	The element noda force vector
F^i	The concentrated force
f^s	The surface traction
G	The shear modulus of the constituent material
G	The surface energy in the global coordinate system
H	The additional surface load
h	The thickness of the a micro/nano beam
I	The second moment of inertia
L	The length of the a micro/nano beam
l	The external characteristic length
m_{kl}	The couple stress in micropolar
$n = (n_x, n_y, n_z)$	The base vector in 3D
N_r	The longitudinal force caused by residual stress

q_c	The distributed load
t	A time point
t_{kl}	The nonlocal stress tensor
$u = (u_x, u_y, u_z)$	The displacement vector in 3D
$U_{bending}$	The strain energy caused by bending
U_r	The strain energy caused by residual stress
V	The volume domian occupied by the solid
w	The deflection of beam
$\mathbf{u}^e$	The nodal displacement vector
Note:	Specific notations are defined by various subscripts or superscripts; see the definitions in the text.

List of Figures

Abstract

Structures exhibit uncommon physical properties such as ultra-high quality factor, nonlinear damping, and the abrupt change of Young's modulus when their size approaches 1 nm to 100 nm. Such amazing properties upon the length scale is the so-called size effects. Though previous experimental studies reveal that the nanostructures do not comply with the classical continuum theories at nano-scale, their inherent mechanism is still unclear yet. The work in this dissertation aims to develop a computational method to predict the size effects for nanoporous materials and introduce the method of structural topology optimisation into the utilization of size effects in micro/nano-electrical/mechanical system, ultra-high sensitive sensor, lightweight structure and high-strength material. To achieve the aforementioned aims, a framework in terms of the combination of surface elasticity theory and the generalized Young-Laplace equation is established to evaluate the size effects. By modelling the nanoporous gold as a complex cellular architecture in theoretical analysis, the abrupt change in Young's modulus at nano-level is formulated and can be verified in previous experiments. Subsequently, an iterative algorithm based on finite element analysis is developed to allow this method applicable to the nanostructures in an arbitrary shape. The proposed computational method clearly shows that size effects are highly dependent on the structural shape and topology at the nanoscale. By assuming the complex structures as a system of interconnected beams, I proposed a beam element to incorporate the size effects in finite element analysis. This general method paves the way to apply the method of structural topology optimisation in the design of nanoporous structures. Its versatile and powerful functions will fuel up the utilization of size effects in future.

List of Publications

The contents of this thesis have been presented through the following publications.

Journal papers

1. **Lu, Dingjie**, Yi Min Xie, Qing Li, Xiaodong Huang, and Shiwei Zhou. *"Towards Ultra-Stiff Materials: Surface Effects on Nanoporous Materials."* Applied Physics Letters 105, no. 10 (2014): 101903. http://dx.doi.org/10.1063/1.4895582.

2. **Lu, Dingjie**, Yi Min Xie, Qing Li, Xiaodong Huang, and Shiwei Zhou. *"Investigating Size Effects of Complex Nanostructures through Young-Laplace Equation and Finite Element Analysis."* Journal of Applied Physics 118, no. 20 (2015): 204301. http://dx.doi.org/10.1063/1.4935819.

3. **Lu, Dingjie**, Yi Min Xie, Qing Li, Xiaodong Huang, Yang Fan Li, and Shiwei Zhou. *"A Finite-Element Approach to Evaluating the Size Effects of Complex Nanostructures."* Royal Society Open Science 3, no. 12 (2016). http://dx.doi.org/10.1098/rsos.160625.

Conference papers

1. **Lu, Dingjie**, Yi Min Xie, Qing Li, Xiaodong Huang, and Shiwei Zhou. *"Size effects on arbitrary structures: a numerical analysis in terms of Young-Laplace equation."* ACCM2015. Brisbane, QLD, Australia.

2. **Lu, Dingjie**, Yi Min Xie, Qing Li, Xiaodong Huang, and Shiwei Zhou. *"The extended Timoshenko beam element in finite element analysis for the investigation of size effects."* ICCM2016. Berkeley, CA, USA

CHAPTER 1

INTRODUCTION

1.1 Challenges in micro and nano scale applications

Nanomaterials are materials with any external or internal dimension in the nanoscale, which is defined as: “Size range from approximately 1 nm to 100 nm.” (Poole Jr and Owens, 2003) Since characteristic length overlap with the critical length scales in materials (Abazari et al., 2015), the mechanical, electrical, thermal and magnetic properties of nanomaterials become different from their macroscale counterpart. This dependence of material properties upon the length scale is the so-called size effects. Many cases of mechanical properties tests on materials at micro and nano scale indicate that material response in a different way from the predictions of classical continuum theories like beam theories and Hooke’s law.

Due to the small sizes, nanomaterials hold great potential to build novel, versatile micro- and nano- electrical and mechanical system (M/NEMS) applications, such as ultra-high sensitive mass, force and bio-detectors (Anja et al., 2011; Arlett et al., 2011; ChasteJ et al., 2012; Hanay et al., 2012; MoserJ et al., 2013), high performance lightweight structure, high strength material, efficient catalysis, and actuating (Jung et al., 2007; Lu et al., 2014; Meza et al., 2014).

Apart from the extreme performance, the low dimension and power consumption of nanomaterials are inherent advantages for implementation and miniaturization of M/NEMS devices. The key to the successful M/NEMS applications is the ability to predict the devices’ characteristics (Abazari et al., 2015), which implies that one should have the ability to predict and control the mechanical response of materials at such small length scale.

As the size decreasing, deviations of material’s characteristic from the one at macroscale have been observed in resistivity (Durkan and Welland, 2000; MoserJ et al., 2013), thermal

conductivity (Boukai et al., 2008), and mechanical properties. In terms of mechanical properties, it will introduce uncommon nonlinear response (Villanueva et al., 2013), ultra high quality factor (Villanueva and Schmid, 2014), nonlinear damping (EichlerA et al., 2011), and the variation of the Young's modulus.

This requires a thoroughly understanding of the structural and mechanical properties of materials at low dimensions. A proper theoretically model that is capable of providing quantitative understanding and predictions of the abnormal mechanical phenomena at micro nano scale is of vital importance.

1.2 Size effects of Young's modulus

As a fundamental mechanical property that determines the response of structures, Young's modulus is considered as a bulk material property that independent of size at macroscale. At the nanoscale, however, it has been observed that the mechanical behavior of structures is not consistent with the predictions of macroscopic theory, which take Young's Modulus as a constant value. Indeed, Young's Modulus exhibits the size-dependence in many cases.

Extensive literatures exist that report size effects of Young's modulus by different experiment method and on different materials. There are mainly two categories of testing method. The most straightforward one is direct test on the material sample, such as indentation test or tension test. Though this kind of method is intuitive and concise theoretically, it is hard to implement and eliminate those factors that will influence the experiment due to the fact that the sample is extremely small. The most majority experimentally obtained Young's modulus on nanomaterials is the so-called effective Young's modulus obtained by analyze the rigidity of different test samples in bending test, such as point load deflection or frequency related test, like resonant frequency test.

The pioneering experimental attempt on the size effects of Young's modulus was the indentation tests on micron size Mo and W single crystals, which were studied by the scanning tunneling microscopy (Stelmashenko et al., 1993). Size dependence of Young's modulus was reported from the resonant frequency test on ZnO nanowires with diameters ranging from 17 to 550 nm, the measured modulus increased dramatically with the decreasing diameters (Chen et al., 2006a). This increasing trend was reported by bending tests with different boundary

conditions as well (Andrew and Jonathan, 2005; Chen et al., 2006a; Fleck et al., 1994; Lam et al., 2003; Liang et al., 2008; Mathur and Erlebacher, 2007; Volkert et al., 2006).

With recent progress on micro- and nano-manufacturing and additive production, experiments at smaller size and on different materials are able to implement and reveal the increasing of Young's modulus with shrinking size (Chen et al., 2007b; Cuenot et al., 2004; Poncharal et al., 1999; Shin et al., 2006). Actually, this tendency is the prevailing result for most of the cases.

Meanwhile, Young's modulus can show the opposite tendency with decreasing size, or remaining constant as at macro scale (Gavan et al., 2009; Nilsson et al., 2004; Wu et al., 2005). It is also worthwhile to mention that for some materials all three types of the aforementioned tendencies have been observed experimentally, such as ZnO (Chen et al., 2007b) and GaN (Stan et al., 2007).

1.3 Theoretical models for size effects of Young's modulus

The discrepancy between the aforementioned experimental works and the prediction from classical continuum theory motivated the development of new theories. The predominant theories to explain these size effects are reviewed hereafter.

1.3.1 Nonlocal theory of elasticity

Most conventional elastic theories are based on hyperelastic constitutive relations under the assumption that the stress at a point is only functions of strains at that point. The nonlocal theory of elasticity proposed by Eringen (Eringen, 1972, 1983, 2002), however, assumes that the stress at a point is a function of strains in a region near that point in the continuum. This theory includes information of long-range interactions, such as interactions between charged atoms or molecules in a solid between points in a continuum. A parameter that can account for the effects of changing scale is introduced into this theory and makes the nonlocal theory of elasticity a candidate for size effects.

The basic equations of linear homogeneous and isotropic elastic solids under nonlocal

continuum theory are:

$$t_{kl,k} + \rho(f_l^b - \ddot{u}_l) = 0 \tag{1.1}$$

$$t_{kl}(\mathbf{x}) = \int_V \alpha(|\mathbf{x}' - \mathbf{x}|, \tau)\sigma_{kl}(\mathbf{x}')dv(\mathbf{x}') \tag{1.2}$$

$$\sigma_{kl}(\mathbf{x}') = \lambda e_{rr}(\mathbf{x}')\delta_{kl} + 2\mu e_{kl}(\mathbf{x}') \tag{1.3}$$

$$e_{kl}(\mathbf{x}') = \frac{1}{2}(\frac{\partial u_k(\mathbf{x}')}{\partial x_l'} + \frac{\partial u_l(\mathbf{x}')}{\partial x_k'}) \tag{1.4}$$

where t_{kl}, ρ, f^b, and u_l are, respectively, the stress tensor, mass density, body force density, and the displacement vector at a reference point $\mathbf{x}$ at time t and $\sigma_{kl}(\mathbf{x}')$ is the macroscopic (classical) stress tensor at point $\mathbf{x}$ which is related to the linear strain tensor at any point $\mathbf{x}'$ in the body at time t, with λ and μ being the Lame constants. $\alpha(|\mathbf{x}' - \mathbf{x}|, \tau)$ is the nonlocal modulus that introduce the nonlocal effects at point $\mathbf{x}$ produced by local strain at point $\mathbf{x}'$. $|\mathbf{x}' - \mathbf{x}|$ is the Euclidean distance, and $\tau = e_0 a/l$ is defined with a the internal characteristic length, l the external characteristic length and $e_0 = 0.39$ (Eringen, 1983). The field equation for nonlocal theory of elasticity can be obtained by using divergence theorem and integration by parts combining equation (1.1), as:

$$\begin{aligned} &- \int_{\partial V} \alpha(|\mathbf{x}' - \mathbf{x}|, \tau)\sigma_{kl}(\mathbf{x}')n_k' da(\mathbf{x}') \\ &+ \int_V \alpha(|\mathbf{x}' - \mathbf{x}|, \tau) \times \sigma_{kl,k} dv(\mathbf{x}') + \rho(f_l^b - \ddot{u}_l) = 0 \end{aligned} \tag{1.5}$$

The first integral integrates over the surface of the body, represents the surface stresses. Consequently, nonlocal theory of elasticity accounts for surface physics which is missed from classical theories. Together with the ability to account for the size effects, these advantages makes the nonlocal theory of elasticity an effective way of simulating the nanomaterials. The integration of nonlocal theory with beam and shell models have been widely employed in the static (Pradhan and Murmu, 2010; Zhang et al., 2005, 2009) and dynamic (Wang et al., 2007; Wang and Hu, 2005; Zhang et al., 2005) problems of nanomaterials. However, the form of the small-scale parameter depends on boundary condition, chirality and the nature of motions. How to determine this parameter and its validation by experimental tests remain open question. More studies are needed to fully evaluate the nonlocal continuum models to analyze behaviors of nanomaterials with various boundary conditions, dimension, and loadings (Arash and Wang,

2012).

1.3.2 Micropolar theory of elasticity

The micropolar theory of elasticity, also known as couple stress theory, comes into being due to the common understanding that classical continuum mechanics do not incorporate any intrinsic material length scale, and are insufficient to describe the behaviors of materials with microstructures. This theory incorporates a local rotation of points in the material as well as the translation assumed in classical elasticity and is realized by introducing a torque per unit area (couple stress) as well as a force per unit area as the conventional stress in classical elasticity (Cosserat and Cosserat, 1907; Fleck and Hutchinson, 2001). It derives from the fact that material points of the continuum with a microstructure will not only deform macroscopically but also microstructurally which will produce the size effects. That is to say for materials that are not ideally homogeneous, the behavior of such materials is dependent on additional microscale length parameters and microstructural degrees of freedom (Eringen, 1965; Mindlin, 1964).

In micropolar theory of elasticity the force stress and couple stress of a deformed body depend on strain ε and microrotation ϕ. The constitutive relations for linear micropolar theory can be written as (Lakes, 1991):

$$\sigma_{kl} = \lambda\varepsilon_{rr}\delta_{kl} + (2\mu + \zeta)\varepsilon_{kl} + \zeta e_{klm}(r_m - \phi_m) \tag{1.6}$$

$$m_{kl} = \alpha\phi_{r,r}\delta_{kl} + \beta\phi_{k,l} + \gamma\phi_{l,k} \tag{1.7}$$

where σ_{kl} is the force stress, m_{kl} is the couple stress, $\epsilon_{kl} = (u_{k,l} + u_{l,k})/2$ denotes the small strain, u_k denotes the displacement and e_{klm} is the permutation symbol. The microrotation ϕ_k is kinematically distinct from the macrorotation $\varphi_k = (e_{klm}u_{m,l})/2$ obtained from the displacement gradient. λ and μ are the two Lame's constants in classical elasticity, ζ, α, β and γ are new micropolar constants that introduce the couple stress effects. k, l, m and r are indices that vary from 1 to 3, representing the variables in x, y, z directions in Cartesian coordinates, respectively.

For a micro/nano beam with L, b and h respectively as length, width and thickness. The size dependent Young's modulus E^* can be calculated by considering the strain energy and the

kinetic energy of the beam as (Abazari et al., 2015):

$$E^* = E + 24\frac{E}{1+\nu}\Big(\frac{l}{h}\Big)^2 \tag{1.8}$$

where l is the material length scale parameter and ν is the Poisson's ratio.

According to equation (1.8), the micropolar theory is capable of predicting a strengthening effects with reducing size. It is consistent with the observation that some structures would show a strengthening behavior in bending experiments. However, how to determine the length scale parameter and whether it is size dependent is unknown. More importantly, the micropolar theory can not explain the softening effects reported in the experiment.

1.3.3 Grain boundary theory

Grain boundary theory accounts for the size effects in materials based on the fact that grain boundaries have different mechanical properties compared with the core of the grains. Due to different residing conditions, molecules on grain boundaries have different orientation and energy level compared with its internal counterpart, which leads to different mechanical properties (Lian et al., 2013).

It models a grain of diameter a by a thin surface layer (of thickness δ) with Young's modulus E_{gb}, and the core part of the grains with Young's modulus of E. Considering a micro/nano beam with the same dimensions as in section 1.3.2 and assuming the grain size remains constant with change of size. An approximate formula for the effective Young's modulus for bending can be derived using composite theory as (Abazari et al., 2015):

$$E^* = \frac{24}{h^3}\Big[\frac{c_1}{a}(\frac{h}{2a}) + c_2 a\sum_{n=1}^{h/2a}(n-\frac{1}{2})^2\Big] \tag{1.9}$$

where:

$$c_1 = \frac{\pi}{8}\big[\delta(a^3 - 3\delta a^2)E_{gb} + \frac{a}{8}(a^3 + 24a\delta^2 - 8\delta a^2)E\big] \tag{1.10}$$

$$c2 = \pi\big[\delta(a-\delta)E_{gb} + \frac{a}{4}(a-4\delta)E\big] \tag{1.11}$$

for $\delta \ll a$, grain boundary theory will predict a dependence with the thickness of the type

$E^* \propto 1/h^2$ and a strengthening effects with decreasing of size will be predicted.

1.3.4 Residual stress theory

Residual stress theory, as it states, accounts for the influence of residual stress in the material to the stiffness. Residual stress exists ubiquitously in different fabrication processes. It remains in the structures with fixed boundary conditions, like clamped-clamped beams and is observed in many literatures (Karabalin et al., 2009; Lachut and Sader, 2009, 2012; Pini et al., 2011; Schmid and Hierold, 2008; Verbridge et al., 2007; Wilmsen et al., 1972; Wilson et al., 2009). It is inevitable to consider the residual stress when modelling the mechanical response of the structures.

For the case of a fixed-fixed beam with the same dimension as mentioned in section 1.3.2, the size dependent Young's modulus can be obtained by energy method. The total elastic energy when it is deformed can be written as the sum of the energy contributions from bending and residual stress.

The bending energy $U_{bending}$ can be expressed as:

$$U_{bending} = \int_0^L \frac{M(x)^2}{2EI} dx = \frac{EI}{2} \int_0^L w''(x)^2 dx \tag{1.12}$$

where E is the Young's modulus, I is the moment of inertia, M denotes the bending moment and w is the deflection.

The energy U_r caused by residual stress is defined as:

$$U_r = \int_0^L N_r d(\Delta L) \approx \frac{\sigma_0 bh}{2} \int_0^L w'(x)^2 dx \tag{1.13}$$

where σ_0 is the residual stress and $N_r = \sigma_0 bh$ is the longitudinal force caused by residual stress.

And the effective Young's modulus of this clamped beam is:

$$E^* = E + \frac{\sigma_0 bh}{I} \frac{\int_0^L w'(x)^2 dx}{\int_0^L w''(x)^2 dx} = E + 12 \frac{\sigma_0}{h^2} \frac{\int_0^L w'(x)^2 dx}{\int_0^L w''(x)^2 dx} \tag{1.14}$$

With a concentrated force F acting at the center of the clamped beam, the integral in

equation (1.14) can be calculated with the corresponding deflection solution as:

$$E^* = E + \frac{3}{10}\sigma_0(\frac{L}{h})^2 \tag{1.15}$$

As can be seen that boundary conditions have a significant impact on the prediction made by this theory. The stress-related term has a coefficient of $(L/h)^2$, which implies different size effects will occur for different aspect ratio, and with a negative or positive value of σ_0 strengthening and softening effects can be predicted.

1.3.5 Surface stiffness theory

Surface stiffness theory accounts for material in a core-shell manner. Similar to grain boundary theory, this theory considers material as the composite of a thin exterior shell (with a thickness of δ) that has a Young's modulus of E_s and the conventional internal bulk solids E (Nilsson et al., 2004).

Due to the different equilibrium conditions between atoms at the surface and inside the material (Zhan and Gu, 2012), the coordination number of atoms close to the surface is lower than that for bulk atoms. When the size is reduced down to nanometers, the surface to volume ratio increases dramatically, and the effects of the difference between surface and internal bulk becomes prominent.

Accordingly, the aforementioned similar effective Young's modulus for bending can be calculated as follow:

$$E^* = E + E_s\Big[(\frac{12}{h^2} + \frac{12}{bh})\delta - (\frac{8}{h^3} + \frac{24}{bh^2})\delta^2 + \frac{16}{bh^3}\delta^3 - \frac{2}{b}\Big] \tag{1.16}$$

where E_s is the surface stiffness with units of N/m and it is defined as: $E_s = \delta\dot{(}E - E')$ calculated as. The value of E_s indicates which one has larger Young's modulus between the surface layer and the internal bulk solids.

In the extreme case that the shell is very thin compared with the size of the structure. Equation (1.16) can be simplified to:

$$E^* = E - 6S_s\frac{1}{h} \tag{1.17}$$

For this theory, the surface stiffness related term has a coefficient of $(1/h)$, which implies a different rate of size effects will occur compared with the residual stress theory. Strengthening and softening effects can be predicted for different combinations of E and E_s.

1.3.6 Surface elasticity theory and generalized Young-Laplace equation

It is clear that all of these theories alone are insufficient to explain the size dependence of Young's modulus of materials at nanoscale, and an extended version base on these theory is needed to model the nanoscale behavior of the Young's modulus.

For nonlocal theory of elasticity, the main challenge lies in the determination of the nonlocal modulus. Theoretically speaking, nonlocal theory includes surface physics and covers classical continuum as a subset. However, the nonlocal modulus and the small-scale parameter is mainly obtained by data fitting from experiments, the physical meaning and the validity of this modulus is hard to determine. The influence of boundary condition, chirality, and the size dependence of these parameters is unclear.

It can be seen from equations (1.8) and (1.9), for micropolar and grain boundary theory, their ability are limited to only predict a strengthening tendency with decreasing size. The grain boundary theory needs strict premise on the size and amount of grains to reach it's conclusion, and it is invalid for crystals. Though the residual stress is capable of predict both strengthening and softening effects with positive and negative residual stress, the predictions are highly rely on the boundary condition. For situations other than clamped ends the residual stress is set free, and the effects of the residual stress vanishes.

Observations of different behaviors on same material with same crystallographic structures indicate that fabrication processes might create surface residues or defects which diversify the behavior of materials (Sun et al., 2008). This implies that surface-related theory is indispensable to explain size dependent elastic properties. More importantly, it is a common understanding that surface effects are thought to be dominant at nanoscale as the surface area to volume ratio increase exponentially. For surface stiffness theory, neither residual stress or surface stress are included in the theory, which makes it incomplete.

This leads to the methodology used in this work, the combination of surface elasticity theory and generalized Young-Laplace equation.

Surface elasticity theory

Developed by Gurtin and Murdoch (Gurtin and Ian Murdoch, 1975) under the classical theory of membranes, surface elasticity theory take the surface elasticity and surface stress into consideration. It is an extension of the surface stiffness theory. A surface stress tensor is introduced in addition to the stress tensor in classical continuum mechanics. Starting form surface energy, the surface elasticity theory introduce the surface stress tensor $\tau^s_{\alpha\beta}$, a symmetric 2×2 tensor in tangent plane, as:

$$\tau^s_{\alpha\beta} = \frac{\partial G(\varepsilon^s_{\alpha\beta})}{\partial \varepsilon^s_{\alpha\beta}} + \tau^s_{0\_\alpha\beta}\delta_{\alpha\beta} \ , \quad (\alpha, \beta = 1, 2, 3) \tag{1.18}$$

where $\delta_{\alpha\beta}$ is the Kronecker delta, $G(\varepsilon^s_{\alpha\beta})$ represents the surface energy in the global coordinate system. The surface strain tensor $\varepsilon^s_{\alpha\beta}$ is assumed to be the tangential strain tensor. $\tau^s_{0\_\alpha\beta}$ represents the initial surface tension, it is the residual surface stress at the strain-free state.

Under the assumption that the surface is homogeneous, isotropic, and linearly elastic (Miller and Shenoy, 2000), the overall surface stress tensor $\tau^s_{\alpha\beta}$ can be simplified to:

$$\tau^s_{\alpha\beta} = \tau^s_{0\_\alpha\beta} + E_s\varepsilon^s_{\alpha\beta} \tag{1.19}$$

where E_s is the surface stiffness with the unit of N/m. In accordance with equation (1.19), the stress tensor $\tau^s_{\alpha\beta}$ in the tangent plane of a surface can be determined as long as the strain is given.

Generalized Young-Laplace equation

The celebrated Young-Laplace equation deals with the surface tension in fluids. It relates the difference between the hydrostatic pressure of a spherical surface with the surface tension and the mean curvature. It established a proportional relation of the pressure with surface tension and curvature (Laplace, 1805; Young, 1805). Gibbs (Gibbs et al., 1928) extended the concept of surface tension to solids, and it is defined by the change in excess free energy when the interface undergo deformation at a constant referential area. Surface stress is particularly important at the nanoscale with large surface to volume ratio. The extension of Young-Laplace equation to the solid case is the generalized Young-Laplace equation. It gives mathematical expression of the

stress discontinuity across the material interface caused by surface stress. With the existence

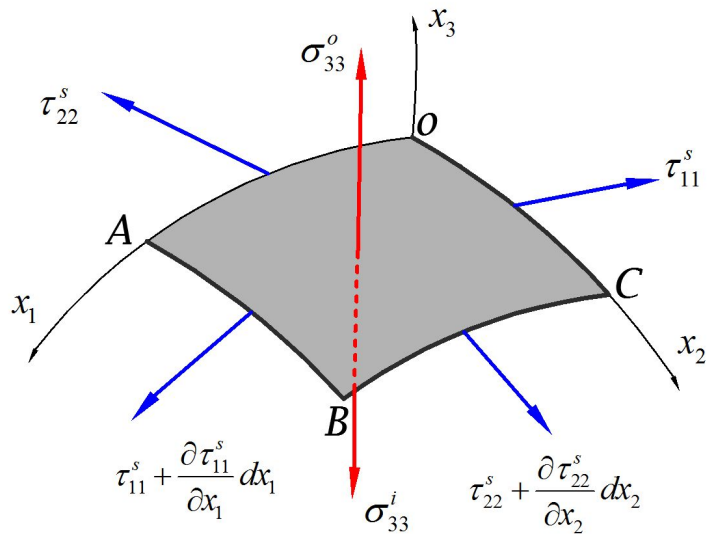

Figure 1.1: A schematic demonstration of an infinitesimal surface element on the curved interface with components of stress vectors σ^o_{33} and σ^i_{33} acting on top and bottom faces and τ^s_{11} and τ^s_{22} along four edges.

of surface stress in Equation (1.19), there exist a stress discontinuity across the surface in the normal direction n. It is mathematically expressed as:

$$[\sigma^o - \sigma^i] \cdot n = -\nabla_s \tau^s \tag{1.20}$$

where σ^o and σ^i represent the conventional stress tensor in the inner side and outer side of an interface, respectively. The principal stresses along the edges (OA and OC) and that with an increment of $\partial\tau^s_{11}/\partial x_1 dx_1$ and $\partial\tau^s_{22}/\partial x_2 dx_2$ along the edges (BC and AB) of the tangent plane are illustrated in Figure 1.1. Note that the shear stress components are neglected in Equation (1.19) for simplification. The surface divergence of a surface stress tensor is denoted as $\nabla_s \tau^s$. Equation (1.20) is the well-known generalized Young-Laplace equation. When employed to explain size effects, it gives the fundamental description of the discontinuity of stress tensor across the curved interface. For a representative infinitesimal surface element $OABC$ on a solid (Figure 1.1) defined on a curvilinear coordinate system $Ox_1x_2x_3$ (O is the origin while x_1, x_2, and x_3 are the coordinate axes, and h_1, h_2 and h_3 represent curvilinear orthonormal basis vectors), it's scale form can be expanded as:

$$\sigma_{31}^{(o)} - \sigma_{31}^{(i)} = \frac{-1}{h_1 h_2}\left[\frac{\partial(h_2\sigma_{11}^s)}{\partial v_1} + \frac{\partial(h_1\sigma_{21}^s)}{\partial v_2} + \sigma_{12}^s\frac{\partial h_1}{\partial v_2} - \sigma_{22}^s\frac{\partial h_2}{\partial v_1}\right] \tag{1.21}$$

$$\sigma_{32}^{(o)} - \sigma_{32}^{(i)} = \frac{-1}{h_1 h_2}\left[\frac{\partial(h_2\sigma_{12}^s)}{\partial v_1} + \frac{\partial(h_1\sigma_{22}^s)}{\partial v_2} - \sigma_{11}^s\frac{\partial h_1}{\partial v_2} + \sigma_{21}^s\frac{\partial h_2}{\partial v_1}\right] \tag{1.22}$$

$$\sigma_{33}^{(o)} - \sigma_{33}^{(i)} = \left(\sigma_{11}^s\frac{1}{h_1}\frac{\partial h_1}{\partial v3} + \sigma_{22}^s\frac{1}{h_2}\frac{\partial h_2}{\partial v_3}\right) \tag{1.23}$$

For simplification (Chen et al., 2006b), the shear stress components are neglected, and only the third one in Equation (1.21) is considered in this thesis .

$$\sigma_{33}^o - \sigma_{33}^i = (\tau_{11}^s\kappa_1 + \tau_{22}^s\kappa_2) \tag{1.24}$$

where κ_1 and κ_2 are the principal curvatures of the surface, and their geometrical definition are illustrated in Figure 1.2.

$$\kappa_1 = \frac{1}{h_1}\frac{\partial h_1}{\partial x_3}, \quad \kappa_2 = \frac{1}{h_2}\frac{\partial h_2}{\partial x_3} \tag{1.25}$$

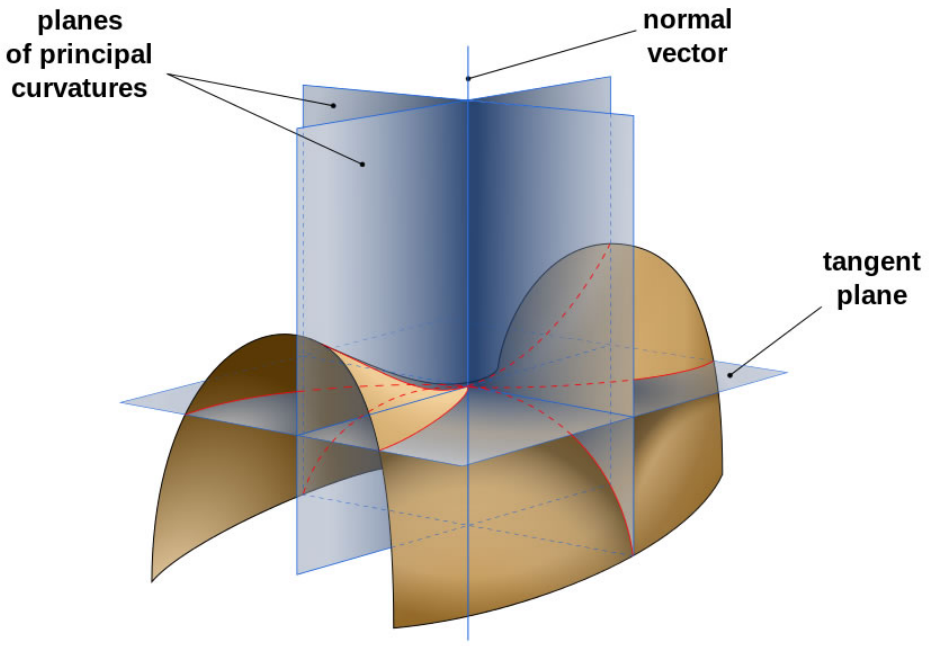

Figure 1.2: The detailed geometry of a surface: the definition of normal vector tangent plane and planes of principal curvatures (Wikipedia, 2016).

It can be seen from Equation (1.24) that the stress discontinuity is a function of the principal

surface stress and curvature in the local curvilinear coordinate system. This stress discontinuity between the inner and outer surfaces are equivalent to an additional pressure acting in the normal direction.

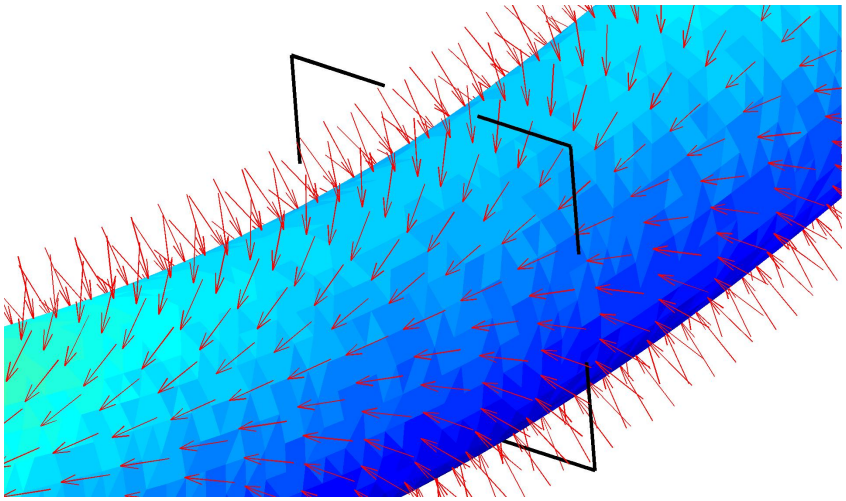

Figure 1.3: A schematic demonstration of additional pressure derived from surface stress by generalized Young-Laplace equation acting alone the inward normal direction of a circular beam surface

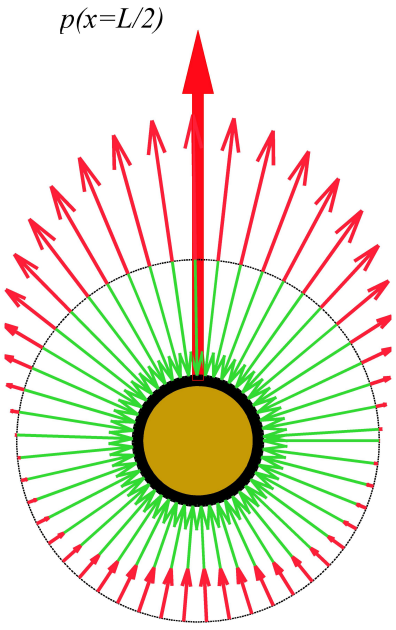

Figure 1.4: The surface load profile for the cross-section (marked black in Figure 1.3) at beam centre

The stress disparities between the inner and outer surfaces are equivalent to an additional pressure acting in the normal direction as shown in Figure 1.3 with red arrows. Figure 1.4

is a close-up of a load profile for a representative cross-section (cut by the black plane in Figure 1.3) at the middle of the beam. If these loads are integrated along the edge of such a cross-section, they are transferred into the non-uniformly distributed pressure against the external surface. For a circular beam without deflection, in the circumferential direction, the line integral equals zero as the principal curvatures at any pair of symmetrical points have the same magnitude but opposite signs (green arrows in Figure 1.4). In other words, the size effects induced loads could be cancelled out if the cross-section of a beam is rotational symmetry. However, in the longitudinal direction one side of the beam would become convex (concave) if small perturbations are introduced. As a result, the load balance of opposite points on the surface will break, and centripetal or centrifugal loads would occur as shown by the red arrows in Figure 1.4. The imbalance of additional loads, together with the initial stress τ_0 and the effective surface stiffness E_s, could make the beam stiffer or softer. Such hardening and softening phenomena are the main reasons of size effects and will be numerically investigated for the Young's modulus hereafter.

1.4 Scope and outline

This thesis is dedicated to studying the mechanisms of the size-dependent material mechanical properties in nanoporous materials. The framework of surface elasticity theory and generalized Young-Laplace equation is used. Rather than focus on solid materials, this thesis studies the nanoporous materials due the their inherent advantages in large surface area which are considered as the dominant source for, as well as, the main approach to address the size effects. To be more specific, the generalized Young-Laplace equation requires the principal curvatures as input to determine the additional size effects loads, which means the curvature need to be included in the formulation of the basic model of the problem if high accuracy and efficiency were to be achieved. It is well-known to us that beam theories and plate/shell theories has the curvature as a variables in the equilibrium formulation, which make beam and shell element as the perfect candidate for apply the adapted framework; As the size of material approaching to nano meters, the microstructure become the dominant factor that influences the mechanical performance. More often than not, porous microstructures are the prevailing states of materials at low dimension; This thesis accounts for the size effects by surface elasticity, and it is straightforward to focus on porous materials that has exceptional large surface area. In this thesis, both analytical and numerical studies are conducted on various materials with different microstructure.

Firstly, the interesting size effects is investigated theoretically through simplified geometrical models. A nanoporous material with a diamond-like microstructure subjected to axis compression is studied. The explicit solution of the effective Young's modulus of this material is obtained. The influence of the surface parameters, namely the initial surface tension and the surface stiffness, are investigated as well. The effectiveness of the theoretical framework of surface elasticity theory and the generalized Young-Laplace equation is validated.

Secondly, the theoretical framework is implemented into an iterative algorithm which extended its scope to 3D solid, by conducting the deformation and shape analysis of the surface of the deformed solid. The limitations imposed by the constraint on geometry and boundary conditions of the analytical method vanished. The size effects is included into the finite element analysis of 3D continuum on the commercial code Abaqus by user subroutine. Simulation of the identical experiment setup is conducted, and the size dependent effective Young's modulus

is obtain and compared with the experiment data.

Then a set of weak form for bending based element, namely beam and plate, are derived mathematically by using the virtual displacement principle. The size effects is explicitly integrated into the element stiffness. And the size effects of single nanowires and nanoporous gold which could be discretized as a spatial frame are studied. Predictions of these structures are compared with the reported experiment data. The efficiency and effectiveness of the new element are validated by case studies.

Finally, the proposed element is incorporated with the structural topology optimisation algorithm BESO, and topology optimisation is conducted to design the microstructure of a nanoporous material and try to utilize the size effects into the design of new material with novel properties.

The thesis is ended by a brief summary and discussion on the potential direction of future work.

CHAPTER 2

SIZE EFFECTS OF NANOPOROUS GOLD

2.1 Size effects of nanoporous materials

Many remarkable features of nanoporous materials are largely attributed to the high surface area to volume ratio of their microstructure at the nanometer scale. Due to strong interactions of molecules and their clusters on such a large surface (Dou et al., 2010; Hodge et al., 2007; Weissmuller et al., 2009), the dependence of Young's modulus and yield stress on the relative density of nanoporous materials cannot be described by conventional scaling laws (Gibson and Ashby, 1999), which are typically applicable to porous materials whose cell sizes are larger than 100 μm. Unfortunately, the structure-property relationships for nanoporous materials remain open questions (Armstrong and Peukert, 2012; Biener et al., 2005; Feng et al., 2009; Zhan and Gu, 2012). Recent advances in the continuum theory of surface elasticity (Gurtin et al., 1998) have opened a new window to studying the size-dependent phenomena at nanoscale (He and Lilley, 2008; Li et al., 2014; Wang et al., 2008; Xiu-Peng et al., 2010; Zhang et al., 2008). A framework of surface elasticity theory was established to evaluate the elastic behaviour of static bending nanowires, indicating that they become softer or stiffer under different boundary conditions (He and Lilley, 2008). The combination of Gurtin's method (Gurtin et al., 1998) with Euler-Bernoulli and Timoshenko beam theories provides an adequate technique to determine the surfaces effects on the elastic properties of nanoporous materials (Feng et al., 2009; Re et al., 2011). Up to date, the fundamental models that have been considered are mainly restricted to an orthogonal structure consisting of only horizontal and vertical beams as shown in Figure 2.1. This structure was conceived for the convenience of deformation analysis rather than efficient material utilization which is of considerable significance to the effective properties of low-

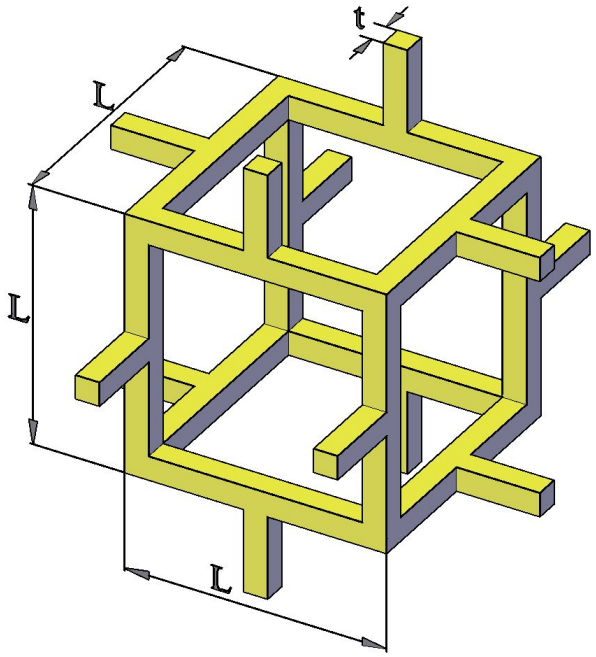

Figure 2.1: The classical Gibson and Ashby' orthogonal cell model (Gibson and Ashby, 1999).

density porous materials (Bendsoe and Sigmund, 2013; Sturm et al., 2010). Therefore, we would like to investigate a micro-cellular architecture (Figure 2.2) which was designed to increase the effective Young's modulus E^* (Schaedler et al., 2011). Such an elegant architecture constitutes an ultra lightweight porous material with $E^* \sim (\rho/\rho_0)^2$ (ρ and ρ_0 denote density of porous and bulk/base materials), distinguished from traditional $E^* \sim (\rho/\rho_0)^3$ for its stochastic counterparts.

The investigation into the effective Young's modulus based on the model proposed in Figure 2.2 will benefit the understanding of the exceptional performance of nanoporous materials which are more commonly composed of inclined beams. In this work we combine the classical solution to Euler-Bernoulli beam theory with the surface elasticity theory to quantify E^* at the nanoscale. The Young-Laplace equation (Chen et al., 2006a) and the surface elasticity model (Gurtin et al., 1998) are used to evaluate the effects of surface tension and surface elasticity. In addition, the Euler-Bernoulli beam theory (Gere and Timoshenko, 1990), which neglects the longitudinal extension of the nanostrut, is utilized to analyze the deflection of struts imposed by distributed transverse load due to the surface effects.

2.2 Size effects of nanoporous with orthogonal unit cell

The representative element (unit cell) of the porous material is a diamond-like cell consisting of eight identical struts as shown in Figure 2.2, where L and $\theta = \pi/3$ denote the strut length and the angle with respect to the horizontal direction, respectively. The strut has a solid circular cross-section with diameter D and the unit cell is subjected to stress σ vertically. The

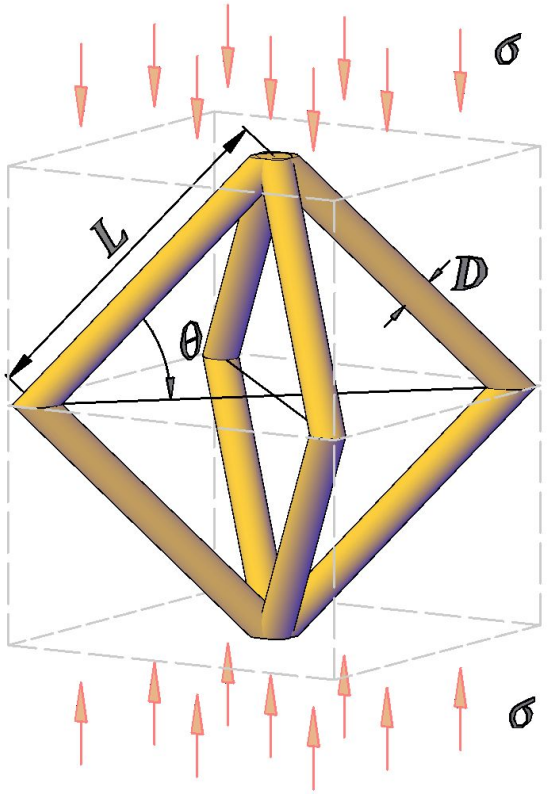

Figure 2.2: A schematic of the octahedral representative unit cell composed of inclined struts.

interactions of superficial resident constraints with the interior atoms lead to surface tension and a stress jump across the interface, which is termed as surface effects generally existing in nanostructures (Cammarata and Sieradzki, 1994). Such effects can be simplified by surface stress caused by transverse load on the edge of nanostruts along normal direction in terms of the generalized Young-Laplace equation and Gurtin's theory of surface elasticity (Cammarata and Sieradzki, 1994; Goudarzi et al., 2010; Miri et al., 2011), given as Equation (1.18). According to Equation (1.18) and under the assumption that the surface of the nanostrut is homogeneous, isotropic, and linearly elastic (Miller and Shenoy, 2000), the overall surface stress τ along the longitudinal direction of the strut is:

$$\tau = \tau_0 + E_s \varepsilon_s \tag{2.1}$$

where τ_0 is the residual surface stress at the strain-free state and ε_s the longitudinal surface strain. The stiffness of the surface layer is denoted as E_s. According to Young-Laplace equation, the stress jump $\triangle\sigma_{ij}$ across the interface depends on the surface curvature $\kappa_{\alpha\beta}$ and surface stress $\tau_{\alpha\beta}$ (Chen et al., 2006a; Miller and Shenoy, 2000; Wang and Feng, 2007), given as:

$$\triangle\sigma_{ij} n_i n_j = \tau_{\alpha\beta}\kappa_{\alpha\beta} \tag{2.2}$$

where n_i and n_j denote the unit normal vectors.

Based on Equation (2.1) and (2.2), the surface effects with consideration of residual surface stress are converted into distributed load along the transverse direction of the beam as shown in Figure (2.3), given as:

$$p(x) = H\kappa \tag{2.3}$$

From Euler-Bernoulli beam theory, the mean curvature $\kappa = w''$ is the second derivative of the small deflection w and variable H is integrated along the edge of cross-section as:

$$H = 2\int_{-\pi/2}^{\pi/2} (D/2)\tau \cos\theta \, \mathrm{d}\theta = 2\tau D \tag{2.4}$$

The equilibrium equation for the bending strut under the distributed force $p(x)$ is:

$$(EI)^* w'''' = p(x) \tag{2.5}$$

When $t << D$, the flexural stiffness, according to the composite beam theory (Gere and Timoshenko, 1990), is:

$$\begin{aligned} (EI)^* &= EI + E_1 \int_0^{2\pi} ((D/2)\cos\theta)^2 (D/2) t \, \mathrm{d}\theta \\ &= EI + \frac{\pi}{8} E_s D^3 \end{aligned} \tag{2.6}$$

where $I = \pi D^4/64$ is the second moment of inertia of circular cross-section. In our model, the elastic modulus $E_1 = E_s/t$ of the surface layer with a thickness of t is governed by the surface

elasticity model while the inner bulk volume obeys the conventional continuum mechanics theory (Chen et al., 2006a; Cuenot et al., 2004; Jing et al., 2006). Under small deformation the surface strain can be approximated as $\varepsilon_s \approx -(D/2)w''$. Substituting Equation (2.1) and (2.4) into Equation (2.5) leads to:

$$(EI)^* w'''' = p(x) = H\kappa \approx 2D(\tau_0 - E_s(D/2)w'')w'' \tag{2.7}$$

After neglecting the higher order term $(w'')^2$, Equation (2.7) is simplified as:

$$(EI)^* w'''' \approx 2D\tau_0 w'' = H^0 w'' \tag{2.8}$$

Figure 2.3 schematically shows the free-body diagram for a typically inclined strut and its deflection w. As discussed above, distributed load $p(x)$ is imposed on the normal direction, and its magnitude depends on the mean curvature. Force F and moment M induced by stress σ are applied at both ends. The cross-section of the beam having thickness t of the layer with surface effects is illustrated in the inset of Figure 2.3. Based on equilibrium equations, these forces can be simply obtained as:

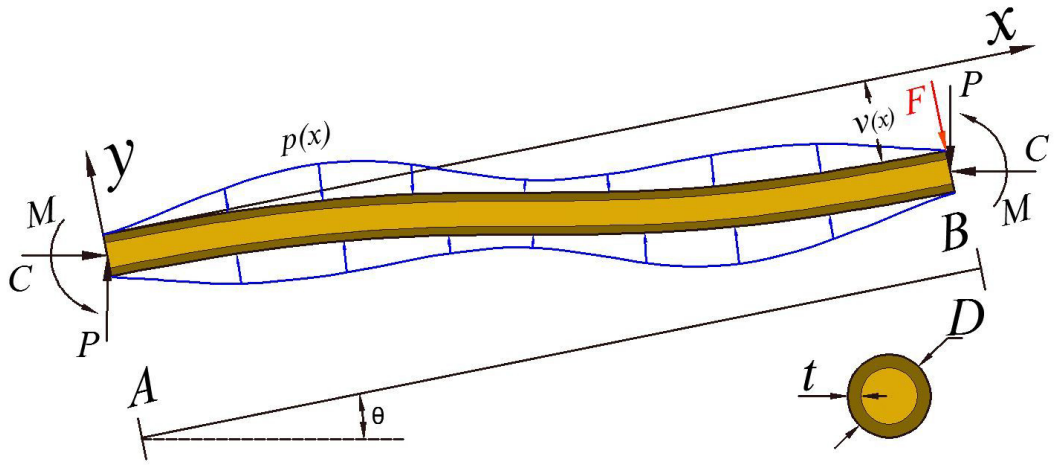

Figure 2.3: The free-body diagram and its deflection for a typically inclined strut under compression stress σ and the distributed load $p(x)$ caused by surface effects.

$$C = 0 \tag{2.9}$$

$$P = (\sqrt{2}L\cos\theta + D)^2\sigma/4 \tag{2.10}$$

$$M = L\cos\theta(\sqrt{2}L\cos\theta + D)^2\sigma/8 \tag{2.11}$$

$$F = \cos\theta(\sqrt{2}L\cos\theta + D)^2\sigma/4 \tag{2.12}$$

The deflection and slope at the fixed left end are:

$$w(0) = w'(0) = 0 \tag{2.13}$$

Due to the symmetry of the geometry and loads, the curvature at the middle of the beam with $x = L/2$ is:

$$w''(L/2) = 0 \tag{2.14}$$

By integrating the transverse load $p(x)$ in Equation (2.8) from $x = \alpha$ to $x = L$ ($\alpha \in (0, L)$), we obtain the force equilibrium as:

$$-(EI)^* w'''(\alpha) = P + \int_\alpha^L H^0 w'' \,\mathrm{d}x = F + H^0(w'(L) - w'(\alpha)) \tag{2.15}$$

With the consideration of boundary conditions Equation (2.13)-(2.15) in Equation (2.5), the deflection is determined as:

$$w(x) = \frac{F(3L - 2x)x^2}{12(EI)^*}, \tau_0 = 0 \tag{2.16}$$

$$w(x) = \frac{F\left(e^{(L-x)\eta} - e^{x\eta} + e^{L\eta}(x\eta - 1) + x\eta + 1\right)}{H^0\left(e^{L\eta} + 1\right)\eta}, \tau_0 \neq 0 \tag{2.17}$$

where $\eta = \sqrt{H^0/(EI)^*}$ is a symbol to simplify the formula. It is noted that Equation (2.16) becomes the classical Euler-Bernoulli beam theory when $E_s = 0$ and Equation (2.17) is equal to Equation (2.16) when $\tau_0 = 0$.

The component $w\cos\theta$ of deflection in the direction of σ divided by the vertical projection $L\sin\theta$ of length L gives

$$\varepsilon = w(L)\cos\theta/(L\sin\theta) \tag{2.18}$$

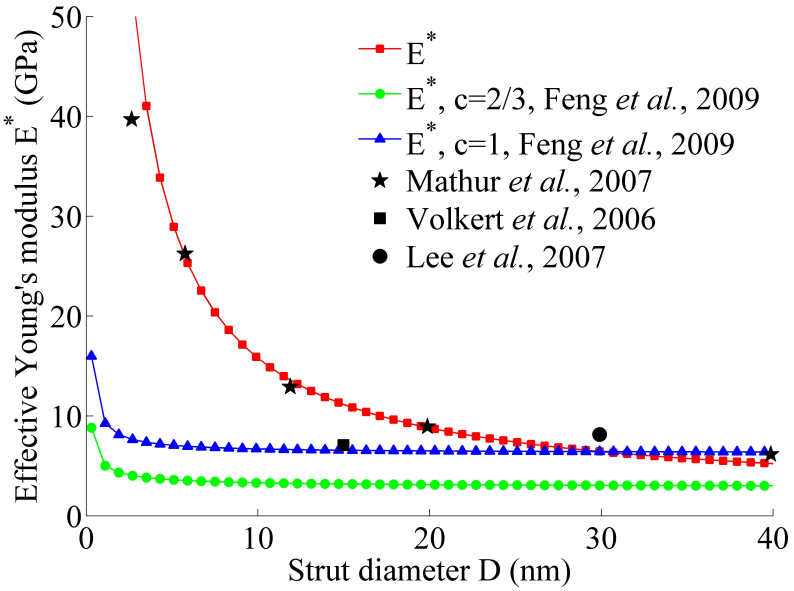

Figure 2.4: The comparison of E^* in terms of octahedral unit cell as well as Gibson and Ashby's model (Feng et al., 2009) with experimental data ($E_s = 3.63N/m$, $\tau_0 = 80N/m$, $\rho/\rho_0 = 31\%$) (Lee et al., 2007a; Mathur and Erlebacher, 2007; Volkert et al., 2006).

Thus the effective Young's modulus $E^* = \sigma/\varepsilon$ is obtained as:

$$E^* = \frac{48(EI)^* \sin\theta}{((\sqrt{2}L\cos\theta + D)L\cos\theta)^2}, \tau_0 = 0 \tag{2.19}$$

$$E^* = \frac{4H^0 L \sin\theta}{((\sqrt{2}L\cos\theta + D)\cos\theta)^2(\frac{2}{\eta}\tanh(-\frac{L\eta}{2}) + L)}, \tau_0 \neq 0 \tag{2.20}$$

The ratio of D to L can be related to the relative density as $D/L = c\sqrt{\rho/\rho_0}$, where $c \approx 1$ is a topology-dependent factor for most porous materials with open cells (Biener et al., 2006). For the cell shown in Figure 2.2, we calculate $c = \sqrt{2\cos^2\theta \sin\theta/\pi}$. Without loss of generality, the relative density is assumed to be $\rho/\rho_0 = 31\%$ in the following discussions (Hodge et al., 2007), a representative value for porous material. Nanoporous gold (np-Au) is used to embody the effective Young's modulus in Equation (2.19) and (2.20) as it has been fabricated by dealloying method (Hodge et al., 2007) with the ligament size ranging from a few nanometers to one micrometer. Moreover, the size-dependent behaviours of np-Au with relative densities from 20% to 42% has been tested (Mathur and Erlebacher, 2007), which can be used as a reliable criterion to evaluate the analysis results. This work mainly focuses on the stiffness, so other superior physical properties and unique functions of np-Au are not considered. For the single-

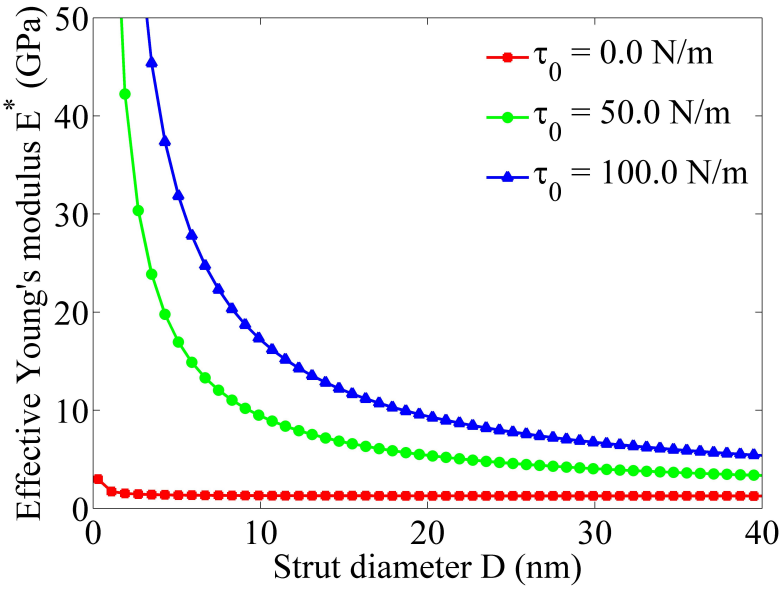

Figure 2.5: effects of residual surface stress τ_0 on the effective Young's modulus E^* with $E_s = 3.63N/m$ and $\rho/\rho_0 = 31\%$.

crystalline gold, $E_0 = 70$ GPa, $\tau_0 = 1.40$ N/m, $E_s = 3.63$ N/m on the (001) crystal surface are calculated from ideal atomic simulation (Shenoy, 2005). However, small ligament size leads to a dramatic increase in residual stress (Lee et al., 2007a). In addition, some post-fabrication processes such as annealing also result in higher residual stress. Therefore, it is plausible to let $\tau_0 = 80$ N/m in equation (2.20).

Figure 2.4 depicts the dependence of E^* on D. It clearly shows that the effective values (the red curve with square markers) well match the experimental data (five black stars in Figure 2.4) for np-Au with similar (001) crystal surface properties (Mathur and Erlebacher, 2007). The blue curve with triangle markers in Figure 2.4 is for the classical Gibson and Ashby's cell with similar parameters except for $c = 1$. It shows the effective values (Feng et al., 2009) are much lower than the experimental data for small ligament size. According to our model and experimental data, the surface effects becomes discernible when the ligament size is smaller than 20 nm while Gibson and Ashby's model does not show this effects until the ligament size is less than 3 nm. The green curve with circle markers in Figure 2.4 is for $c = 2/3$, an exact calculation for Gibson and Ashby's cell, but it deviates from the experimental results further. The black square (Volkert et al., 2006) and black circle markers (Lee et al., 2007a) stand for the experimental data for np-Au from other references, which are within an acceptable error

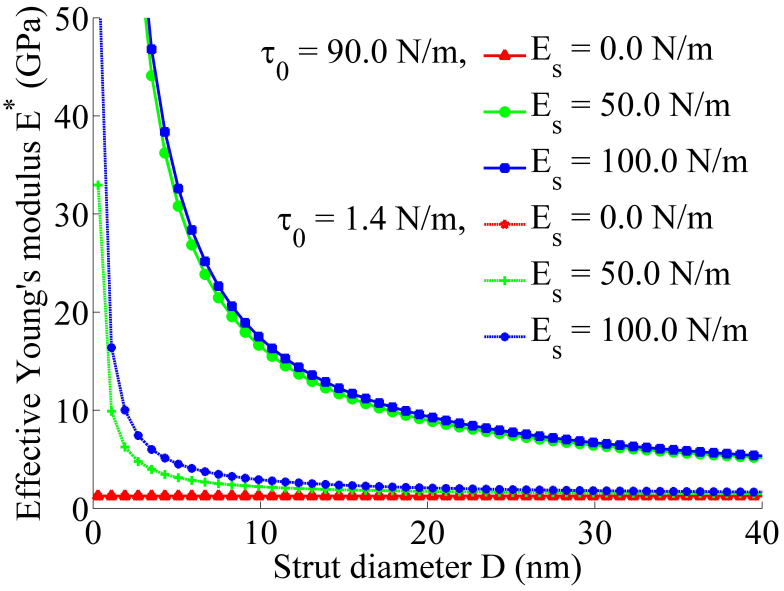

Figure 2.6: effects of surface stiffness E_s on the effective Young's modulus E^* with $\tau_0 = 1.4N/m$ and $\tau_0 = 90N/m$ for $\rho/\rho_0 = 31\%$.

margin in comparison with our analytical results.

Because the residual stress is significantly influenced by the fabrication techniques and the surface stiffness varies with different crystal surfaces, the effects of τ_0 and E_s on E^* are presented in Figs. 2.5 and 2.6, respectively. Both figures illustrate that the increase of each factor leads to higher E^*, in particular when the strut size is less than 10 nm. However, it seems that τ_0 plays a more significant role in affecting E^* than E_s when the ligament size $D > 3$ nm. It is noted in Figure 2.5 that the critical point of surface effects changes from 1 nm to 10 nm for the ligament size when τ_0 increases from 0 to 50 N/m. The role of τ_0 on intensifying the surface effects becomes weaker for larger residual stress as shown in the blue curve with triangle markers for $\tau_0 = 100$, which is only marginally higher than the green curve with circular markers for $\tau_0 = 50$ N/m in Figure 2.5. Compared with the residual stress, the surface stiffness is less important because the doubling of E_s from 50 N/m to 100 N/m slightly changes E^* in Figure 2.6. If $\tau_0 = 1.4$ N/m, the role of E_s is negligible unless $D < 1$ nm. Thus it is more reasonable to attribute the rise of E_s in Figure 2.6 to the higher value of $\tau_0 = 90$ N/m than to $E_s = 50$ N/m or $E_s = 100$ N/m.

2.3 Summary

The significant rise in the strength and stiffness of porous materials at the nanoscale cannot be described by conventional scaling laws. This chapter investigates the effective Young's modulus of such materials by taking into account surface effects in a micro-cellular architecture designed for an ultralight material whose stiffness is an order of magnitude higher than most porous materials. By considering the surface effects, the predicted stiffness using Euler-Bernoulli beam theory compares well to experimental data for spongelike nanoporous gold with random microstructures. Analytical results show that, of the two factors influencing the effective Young's modulus, the residual stress is more important than the surface stiffness.

In conclusion, this work has studied the surface effects on the effective Young's modulus for a model with inclined struts, which is more akin to the microstructure of nanoporous materials. Gurtin's theory and Young-Laplace equation are used in combination with Euler-Bernoulli beam theory to obtain an explicit definition to the effective Young's modulus of nanoporous gold. The analytical solution clearly demonstrates the experimentally observed surge of Young's modulus at nanoscale for nanoporous gold (Mathur and Erlebacher, 2007). It also reveals that the residual surface tension plays a more important role than the stiffness of surface layer. This study affirms that the architecture of microstructure could significantly impact on the overall behaviour of nanoporous materials, and it is possible to optimize the base cell by using structural topology optimisation techniques in order to improve the effective Young's modulus.

CHAPTER 3

ITERATIVE FINITE ELEMENT ANALYSIS OF SIZE EFFECTS OF COMPLEX NANOSTRUCTURES

3.1 Motivation for the iterative finite element analysis

When the size of a structure approaches the nanoscale, its mechanical properties such as Young's modulus and strength could significantly increase (Cammarata, 1994; Cao and Chen, 2007; Chen et al., 2007a; Diao et al., 2004; Farsad et al., 2010; Sharma et al., 2003). For instance, both theoretical analysis and experimental measurements have verified that carbon nanotubes possess amazing specific strength amounting to 48,000 kPa/(kg/m3), a 200-fold increase in comparison with carbon steel in macro size (Peng et al., 2008; Yu et al., 2000) Such size-dependent effects have received increasing attention as they might have promising applications in lightweight structure, high strength material, catalysis, sensing, and actuating (Jung et al., 2007; Lu et al., 2014; Meza et al., 2014).

The enhancement in mechanical properties is mainly attributed to the strong interactions of molecules and their clusters on the material surface when the ratio of surface area to volume becomes extremely large in reduced dimensionality (Cammarata, 1994; Hodge et al., 2007; Zhan and Gu, 2012). With the assumption that surface layers can be superposed and inner substances possess the same elastic properties as bulk material, several analytical methods have been established to quantitatively explain size effects for nanostructures in terms of Gurtin's surface elasticity theory (Gurtin and Ian Murdoch, 1975). The first of such methods is based on a core-shell structure to account for hardened external surface and has been successfully utilized to explain the dramatic rise of Young's modulus for ZnO nanowire in experiments (Chen and Zhu, 2007; Chen et al., 2006a). By employing surface stress and surface elasticity, the silver nanowire is considered as a composite composed of an inner bulk kernel and a bounding skin

under the framework of classical continuum theory, which reasonably explains the remarkable increase of Young modulus with respect to the decrease of the diameter of a nanowire (Gurtin and Ian Murdoch, 1975). Later, a model integrated both generalized Young-Laplace equation and surface elasticity theories was proposed to essentially predict the softened or stiffened effects on the mechanical properties of nanostructures (He and Lilley, 2008). Integrated with simple beam theories, this method offers an adequate platform to determine the effective Young's modulus for nano beams (Feng et al., 2009; Lu et al., 2014; Xia et al., 2011). Though these analytical methods enable the size-dependent properties to be calculated from some explicit formula, they are only applicable to fairly simple structures such as simply-supported beams with regular cross-section and orthogonal frames. Moreover, the strict restrictions on the boundary conditions and external loadings preclude the application of these analytical methods to complex nanostructures, which are ubiquitous in real scenarios.

An alternative approach to compensating for the insufficiencies of analytical methods is classical molecular dynamics simulation (Mi et al., 2008; Miller and Shenoy, 2000; Shenoy, 2005). This method offers insights into the exceptional performance of nanomaterials at the atomic scope and therefore has been widely used to study surface effects. As it necessitates knowing the motions of each individual particle and their interactions, molecular dynamics simulations are only applicable to ultra-small and highly simplified geometrical models. For a common structure at tens of nanometers in size, molecular dynamics simulation is infeasible as the computational cost would be astronomical due to the enormous constituting particles (e.g. 60 million for a 100 nm gold cubic) (Park and Klein, 2008). To avoid such a prohibitive computational cost, finite element method based approaches are often used (Lee et al., 2007a). In this method, a two-node surface element is developed to illustrate the strong size dependence of Young's modulus for a 2D structure subjected to pressure in its cavity (Gao et al., 2006). To simulate nanowire beam under large deformation, a finite element absolute nodal coordinate formulation algorithm (Shabana, 1996) is used to account for the strength and softening effects (He and Lilley, 2008, 2009). To tackle the discontinuities across the interface of two solids for the general deformation in 3D, the level set method (Osher and Sethian, 1988) and the extended finite element method(Moes et al., 1999) are integrated (Farsad et al., 2010; Yvonnet et al., 2008).

This chapter will transfer one of the represent surface effects into a non-uniformly pressure

on the external surface of a complex structure based on the generalized Young-Laplace equation. It will be applicable to the evaluation of the size effects for the nanostructures in any arbitrary shape, which has not been unresolved to our best knowledge. Considering the fact that these advanced structures can be prototyped by modern nanofabrication technology precisely and efficiently (Sun et al., 2005) the work in this field is highly valuable.

The rest of this chapter is structured as follows. Firstly the generalized Young-Laplace equation and surface elasticity theory used to describe the size effects at the nanoscale will be introduced. Then the shape-dependent pressure will be applied to the surface to transfer the size effects into the finite element model. Numerical implementation for a benchmark beam fixed at both ends is elaborated thereafter. Then the influence of surface stiffness and initial surface tension on the effective Young's modulus is discussed. To further demonstrate the capacity of the proposed method, the size effects of two complex structures at the nanometer scale is investigated. One is featured with ultra-light and ultra-stiff properties (Zheng et al., 2014) while the other is produced from structural topology optimisation (Huang and Xie, 2010) for the sake of obtaining maximal stiffness.

3.2 The theoretical foundation

Aiming to fill the gap that conventional finite element method did not include the size effects, the iterative finite element analysis proposed in this chapter adapt the logic used in Chapter 2, the combination of surface elasticity theory and generalized Young-Laplace equation is implemented numerically to extend this method to 3D solid structure with arbitrary topology, loading and boundary conditions. They will be briefly reviewed hereafter.

Surface elasticity theory was developed the classical theory of membranes by Gurtin and Murdoch (Gurtin and Ian Murdoch, 1975). It established a constitutive relation between the surface stress with surface strain and surface stiffness. Apart from the stress tensor in classical continuum mechanics. The surface stress tensor $\tau^s_{\alpha\beta}$, a symmetric 2×2 tensor in tangent plane along the material surface, is introduced. And it can be determined from surface energy as Equation (1.18).

For a homogeneous, isotropic, and linearly elastic surface (Miller and Shenoy, 2000), surface elasticity theory gives a constitutive relation of the overall surface stress tensor $\tau^s_{\alpha\beta}$ as

Equation (1.19). The stress tensor $\tau^s_{\alpha\beta}$ at a point on the material surface can be calculated as long as the strain is given.

The generalized Young-Laplace equation is used to investigate the stress discontinuity across the material interface caused by surface stress. It relates the stress discontinuity across the surface with the surface divergence of the surface stress tensor $\nabla_s \tau^s$ in Equation (1.20). It can be seen from the scaler form Equation (1.24) that the stress discontinuity is a function of the principal surface stress and curvature in the local curvilinear coordinate system. This stress discontinuity between the inner and outer surfaces are equivalent to an additional pressure acting in the normal direction as shown in Figure 3.1.

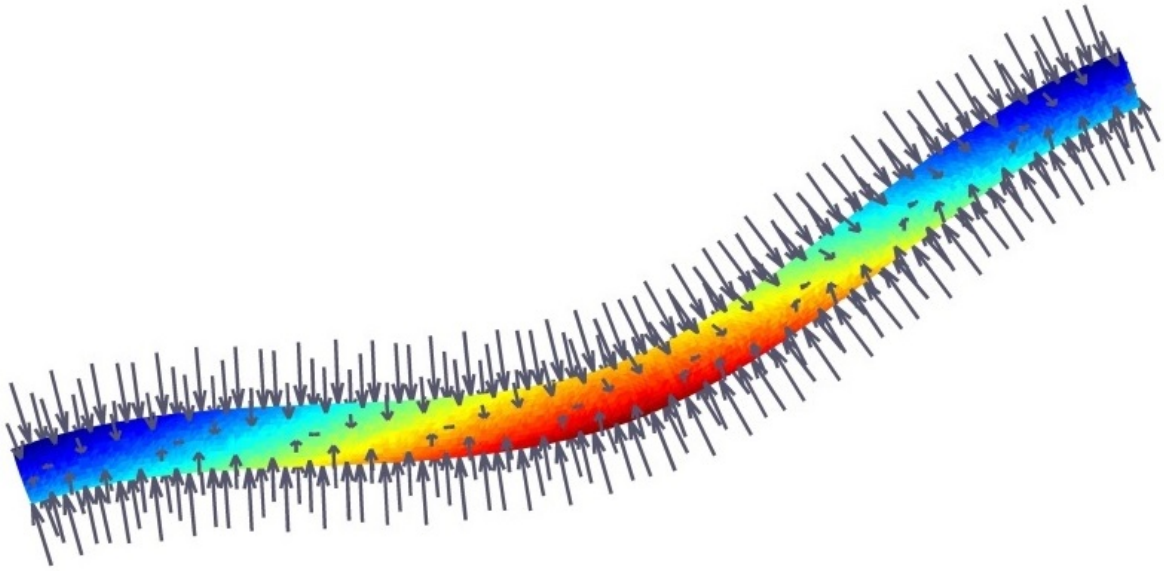

Figure 3.1: The additional pressure, shown as gray arrows, derived from the stress discontinuity across the material interface of a deformed beam.

As a result, this additional pressure could act as resistance or additional loading and could make the structure stiffer or softer. Such weaken, or reinforcement effects is the main reasons of size effects and will be numerically implemented into finite element always in this chapter.

3.3 Implementation of FEM with size effects

The generalized Young-Laplace equation is well understood and has become the cornerstone for a series of analytical models, but the complex structures are widely existing in nano world, where randomly-shaped architectures with irregular cross-sections are subjected to distributed

loads and unusual boundary conditions, still require an effective method to determine their size effects. We can, however, use finite element analysis to obtain the effective Young's modulus for such complex structures. A benchmark of a beam which is fixed at both ends and subjected to a point load at its center is studied firstly to validate the proposed scheme. The diameter and length of the beam are represented as D and L, respectively (Figure 3.2 initially there is no surface pressure as the principal curvatures are totally canceled out.

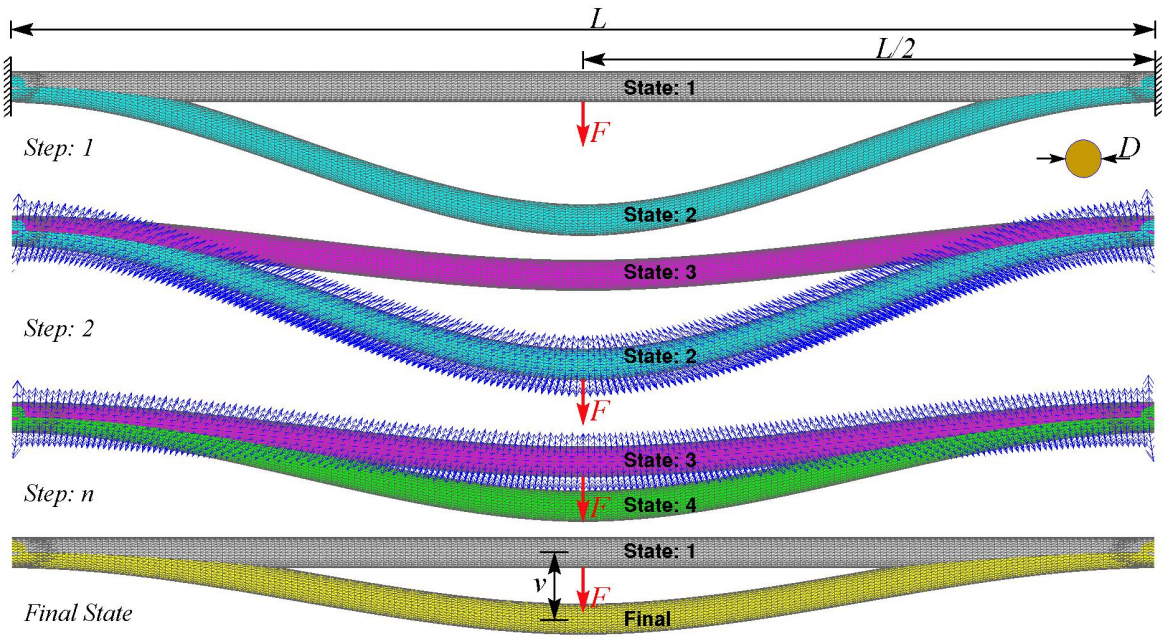

Figure 3.2: The iterative simulation process to capture the size-effects-induced pressure for a beam fixed at both ends under concentrated load F at the beam centre.

To trigger surface pressure, a concentrated force F is applied at the beam center to actuate small but significant initial deflection. This deformation breaks the force balance and leads to distributed pressure as seen in Figure 1.3 (red arrows), which pushes the beam away from initial equilibrium state. In the new configuration, the changes of principal curvatures update the pressure and therefore the just achieved balance is broken. It normally weakens the current bending, sometimes even pushing the beams to the opposite direction. The beam vibrates in such a manner with decreasing amplitude and eventually achieves the final equilibrium state. To be more specific, the iterative process is illustrated in Figure 3.2. Firstly, finite element analysis is conducted to simulate the beam deforming from State 1 (gray) to State 2 (cyan) due to the concentrated load F. Then the principal curvatures of the beam surface at State 2 are calculated

to determine the curvature-dependent distributed surface load (blue arrows). Together with load F, the curvature-dependent pressure continuously deforms the beam into State 3 (magenta). As a result of further deformation, the surface load changes both in magnitude and direction and therefore breaks the balance obtained in the previous step, making the beam be transferred to State 4 (green). Because the deformation in the current stage will always be corrected in next step due to the newly achieved equilibrium state by the end of the current step, the deflection fluctuation attenuates and eventually reaches a balanced state (yellow) with a deflection v at its middle point.

The above algorithm is implemented as a user subroutine in Fortran on the commercial finite element code Abaqus (Systemes, 2013), the detailed code can found in Appendix A.

3.4 FEM simulations of nano structures with size effects

Three cases of nanostructures with different topology and boundary conditions are simulated hereafter to demonstrate the efficiency and effectiveness of the proposed method. To verify the method with experiment results, a clamped beam with concentrated force applied at the beam center is studied first. This case corresponding to the bending test in many literature.

3.4.1 Case study one: clamped beam

A typical convergence process for beams with different diameters are shown in Figure 3.4, in which y-axis denotes the ratio of deflection at middle point to the beam length while x-axis gives the iteration step. This figure clearly illustrates that the thinner the beam, the slower it converges. For instance, it takes around 25 steps for D = 20 nm to converge while only five steps for D = 50 nm. Moreover, the initial amplitudes of the thinner beam are remarkably larger than the thicker ones, consistent with common sense that size effects is more significant at smaller scale. Specifically, we find that the fluctuation fails to converge for a beam with $D < 3$ nm even though hundreds of iteration steps were attempted. The reason for this failure is attributed to the fact that the surface pressure is extremely large for thin beams, resulting in a non-feasible solution or nonlinear deformation or fracture.

The effective Young's modulus for this simply-supported beam undergoing deflection v can

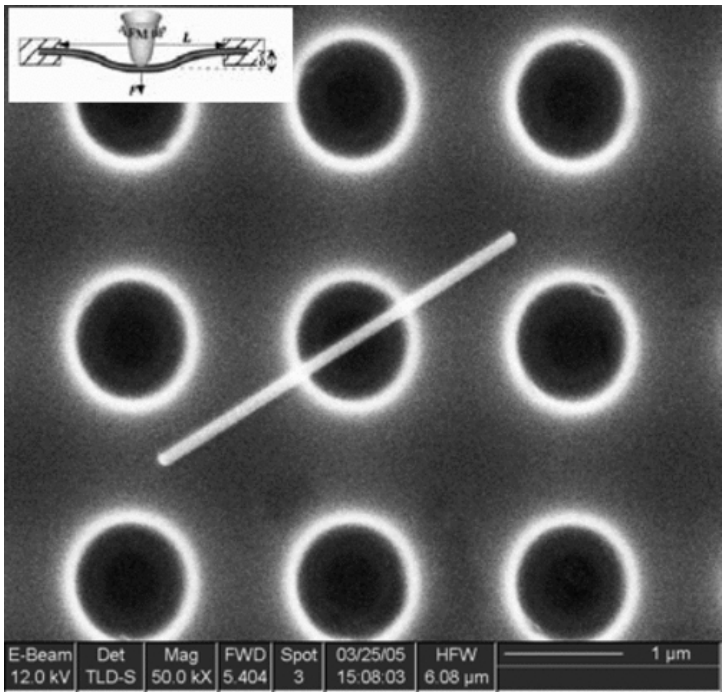

Figure 3.3: SEM image of a typically suspended nanowire ($D = 79nm$), the inset is a schematic showing this nanowire is bent by an atomic force microscopy tip at its middle point (Chen et al., 2006c).

be obtained in accordance with classic Euler-Bernoulli beam theory (Gere and Timoshenko, 1990), given as:

$$v_{max} = \frac{FL^3}{192E^*I} \tag{3.1}$$

where v_{max} is the maximal deflection for the same beam subjected to identical loads and supports and $I = D^4/64$ represents the second moment of inertia of circular cross-section. Because the biggest deflection is around $0.1094D$ or $0.0055L$ in the simulation, it is reasonable to use the assumption of small deformation and neglect the axial stress along the longitudinal direction (Gere and Timoshenko, 1990). Therefore, the effective Young's modulus E^* of the simulated beam can be determined as:

$$E^* = \frac{FL^3}{192v_{max}I} \tag{3.2}$$

The blue curve in Figure 3.5 is the interpolated effective Young's modulus E^* (denoted by the magenta square markers) for a beam with fixed $D : L = 1 : 20$. It clearly demonstrates the surge of E^* as the characteristic size approaches 50 nm. Similar trajectories have been

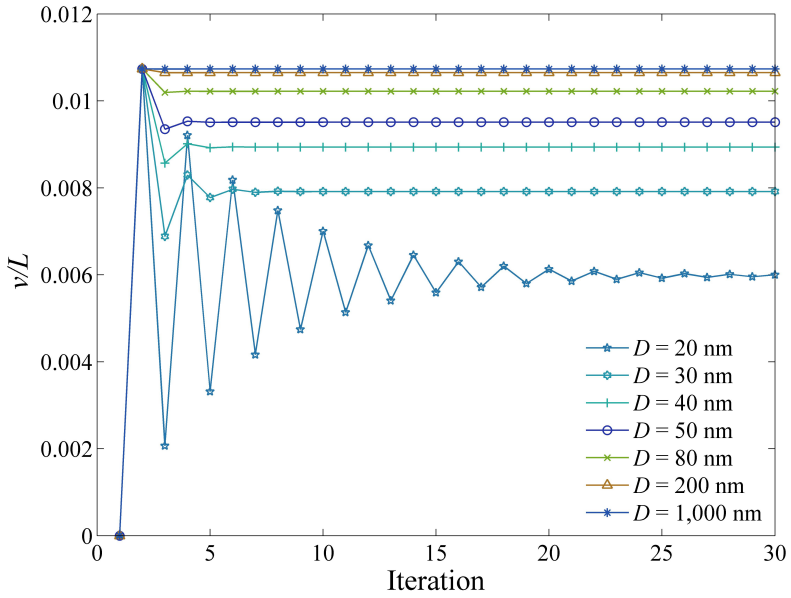

Figure 3.4: The magnitude of normalized deflection at the middle point of a beam fixed at both ends versus its diameter.

reported in tests, in which a silver nanowire is suspended over a dent, and its two ends are tightly clamped onto the substrate. The experimental data (Chen et al., 2006c; Jing et al., 2006) are represented as red stars and red circular markers (the error bars stand for the acceptable error margins), respectively, in Figure 3.5. It is interesting to note, for the similar simply-supported beams under the same boundary conditions, the blue curve matches with the experimental data (brown stars) reasonably well, especially for a thinner beam with $D < 50$ nm. Moreover, the numerical results are within the error margins for two tests with $D = 60$ nm and $D = 79$ nm. Though having the same surface parameters, theoretical prediction (He and Lilley, 2008) represented by the cyan curve with circular marks is, however, notably larger than both the computational results and experimental data. When the beam becomes thicker, the results from computational simulation still perform better than analytical model though both of them deviate from experimental data.

3.4.2 Case study two: complex cubic frame structure

To demonstrate the superiority of this computational method over theoretic analysis, a complex architecture (Figure 3.6) claimed to have an ultra large stiffness (Zheng et al., 2014) was simulated herein. This structure is inscribed in a cube with a width of W, and all struts have the

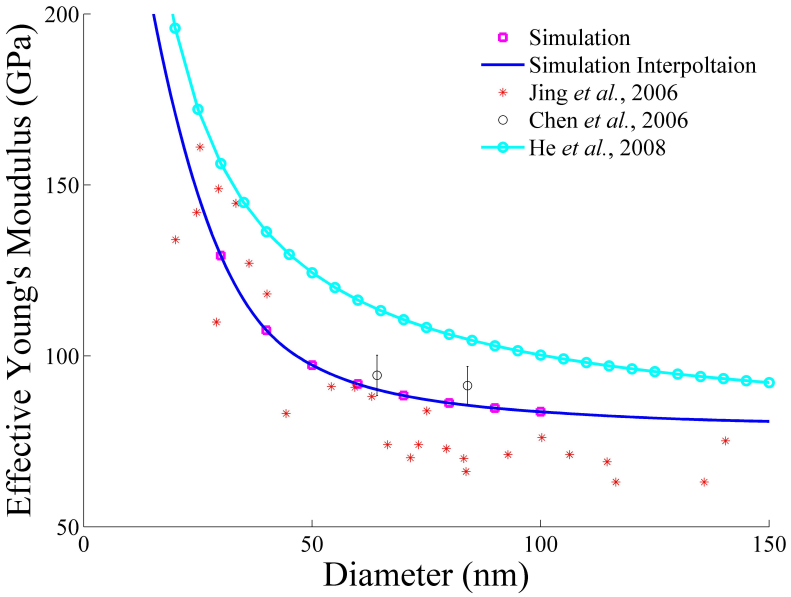

Figure 3.5: The effective Young's modulus E^* from an analytical model (He and Lilley, 2008), experimental data (Chen et al., 2006c; Jing et al., 2006), and computational results.

same circular cross-section with diameter D. Though the length of some struts are different, the ratio of its diameter to the length of cube is fixed to $D : L = 1 : 25$. Because the complexity of this structure, an explicit solution based on the theoretical analysis (Feng et al., 2009; He and Lilley, 2008; Xia et al., 2011) might not be exist. Therefore we have to resort to a computational method for such irregular structures. Due to structural symmetry, a simple uniaxial pressure test is capable of determining the effective Young's modulus by imposing downward deflection which is equivalent to a strain $\varepsilon = 0.1$. With the rational assumption that all bilateral faces are undergone in-plane deformation when the structure are periodically-repeated itself in space, the effective Young's modulus can be determined as:

$$E^* = \sigma/\varepsilon \tag{3.3}$$

where the stress $\sigma = F/A$ is equal to the reaction force F divided by the area A of the inscribed cube. For several representative values of surface stiffness E_s and initial surface tension τ_0, the effective Young's modulus E^* of this complex structure is plotted in Figure 3.7. It is evident that the proposed scheme captures the experimentally observed rising Young's modulus as the diameter is smaller than 10 nm (which is equivalent to a cell with the width of 250 nm). This figure also reveals that the role of surface stiffness is insignificant as a large variation of E_s from

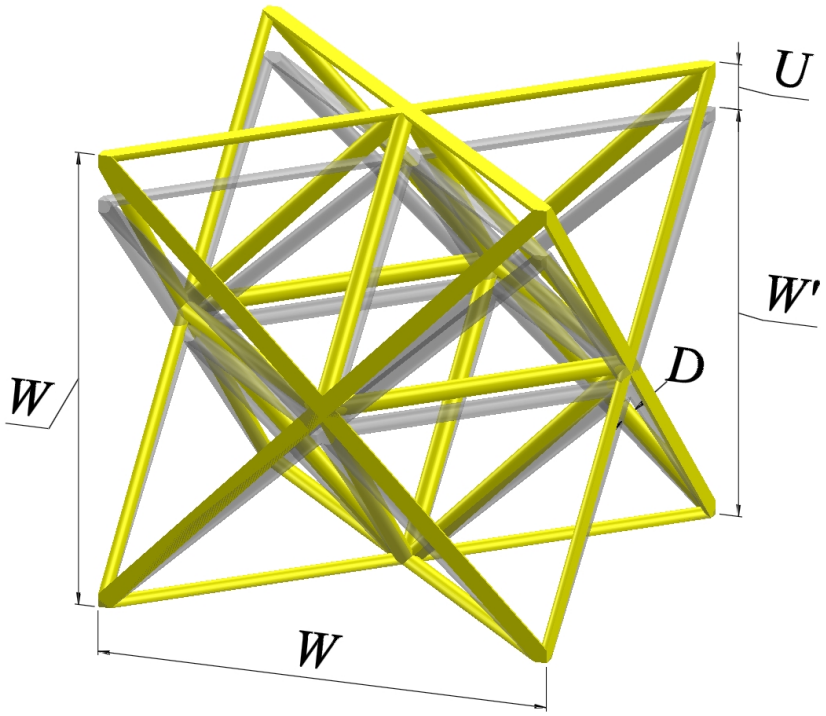

Figure 3.6: A complex cubic frame of width W subjected to vertical compression

8.7 N/m to 50 N/m merely leads to a marginal difference (seen the nearly overlapped green and blue lines in the inset). However, the effective Young's modulus is quite sensitive to the change of initial surface tension as shown by the red, pink and blue curves in Figure 3.7. Similar finding that E^* is proportional to τ_0 has been reported previously via analytical model (Lu et al., 2014). Because this lattice structure is stretch dominant, its stiffness is much larger than the bending dominant beams in Figure 3.5. Therefore it can resist the size effects induced pressure more effectively. As a result, the increase of effective Young's modulus for this lattice is comparably smaller than those of the beams. Moreover, the lattice structure is likely to alleviate size effects as the critical dimension needed to raise E_s considerably is as small as 10 nm.

3.4.3 Case study three: cantilever beam with complex topology

To further test this computational method, it is used to retrieve the effective Young's modulus for a cantilever beam, as shown in Figure 3.8, which is designed to have the maximal stiffness using structural topology optimisation (Huang and Xie, 2010). Figure 3.9 is the cross-section of this beam along the longitudinal direction, from which we can see that this beam has complex topology with cavities and irregular connections. The ration of height(H), length(L) and

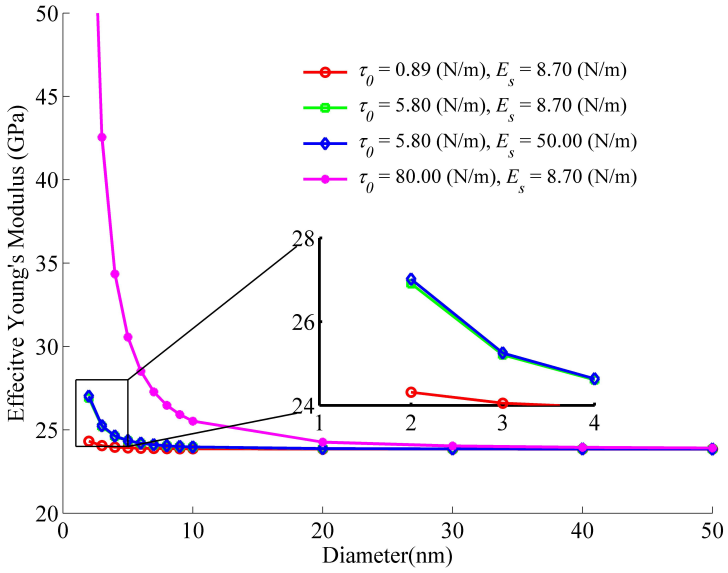

Figure 3.7: The plot of effective Young's modulus E^* versus strut diameter D for the cubic structure.

width(W) of this beam is $L : H : W = 6 : 3 : 1$ and the real dimension are multiplied by 20β (β is a scale factor). A unit load F is applied at the bottom-left end while the right surface is fixed. Within the linear elastic assumption, the maximal deflection is inversely proportional to the effective Young's modulus (Gere and Timoshenko, 1990). Therefore the effective Young's modulus E^* could be obtained as,

$$E^* = \frac{v_{max}}{v_{0max}} E_0 \tag{3.4}$$

where v_{max} and v_{0max} denote the maximal deflection with and without the consideration of size effects, and E_0 is the Young's modulus of the bulk material.

Several computational tests are conducted with different combinations of surface stiffness E_s and initial surface tension τ_0, all showing a remarkably softened effects as the scale factor $\beta < 10$ nm in Figure 3.10. The similar softened effects for a cantilever beam with circular cross-section has been found by He Jin *et at.* (He and Lilley, 2008).

The weakened Young's modulus is mainly attributed to the convex shape of the deformed cantilever, which results in an overall downward pressure. This additional pressure bends the beam with the same direction as the external force F. Thus the deflections are superimposed other than partially offset in previous examples. For this complex cantilever, it is found both

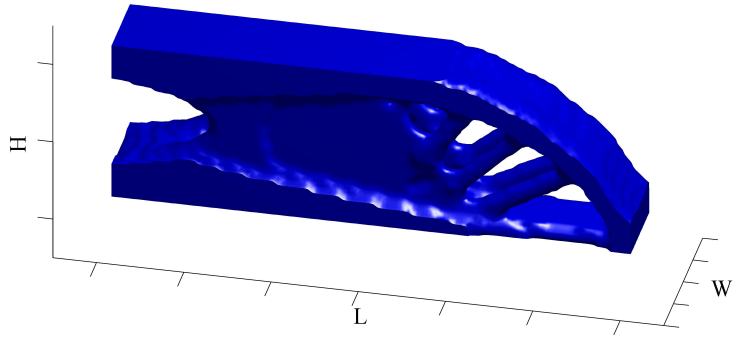

Figure 3.8: A complex cantilever obtained from structural topology optimisation with maximal stiffness.

initial surface tension τ_0 and surface stiffness E_s are appropriate to the softened Young's modulus. However, τ_0 plays a more important role than E_s as a moderate increase of τ_0 (from $\tau_0 = 0.89$ N/m to $\tau_0 = 5.8$ N/m) distinctly changes E^* from the red curve to green curve. While a considerable rise of E_s (from $E_s = 8.7$ N/m to $E_s = 50$ N/m) only slightly changes E^* as shown in the green curve and blue curve in Figure 3.10.

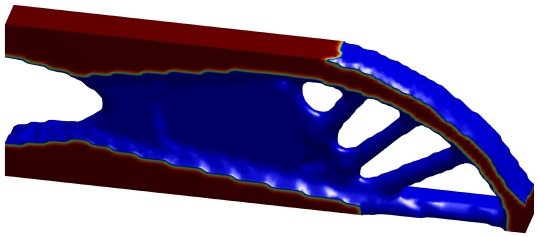

Figure 3.9: The longitudinal cross-section of the complex cantilever obtained from structural topology optimisation with maximal stiffness.

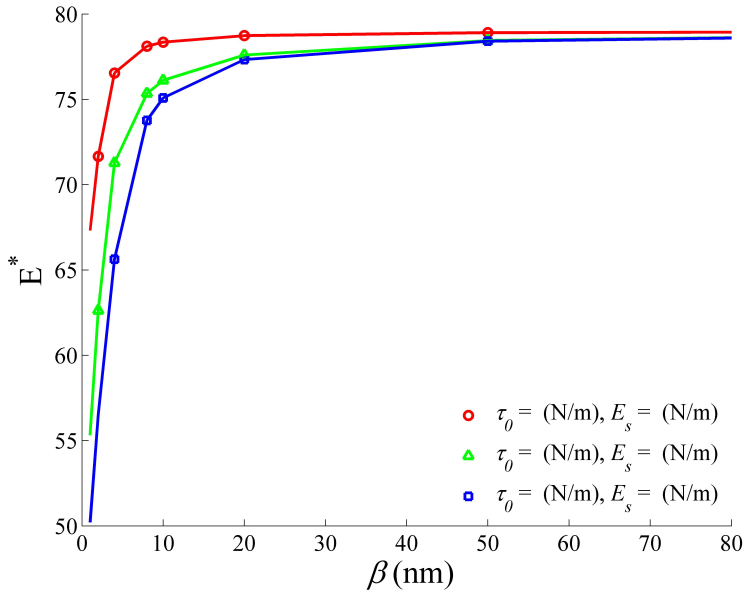

Figure 3.10: The plot of predicted effective Young's modulus E^* as a function of the scale factor.

3.5 Summary

Analytical studies on the size effects of a beam fixed at both ends have successfully explained the sudden changes of effective Young's modulus as its diameter decreases below 100 nm. Yet they are invalid for complex nanostructures ubiquitously existing in nature. In accordance with a generalized Young-Laplace equation, one of the representative size effects is transferred to a non-uniformly distributed pressure against the external surface due to the imbalance of inward and outward loads along the interface. Because the magnitude of the load depends on the principal curvatures, iterative steps have to be adopted to stabilize the structure in finite element analysis gradually. Computational results from the simulation are in good agreement with both experiment data and theoretical prediction. Furthermore, the investigation on the strengthened and softened Young's modulus for two complex nanostructures demonstrates that the proposed computational method provides a general and effective approach to analyze the size effects of nanostructures of arbitrary shapes.

In this study, we have proposed a recursive computational method to determine the size effects for nanostructures by integrating finite element analysis with a generalized Young-Laplace equation. One of the representative surface effects is transferred into a non-uniformly distributed pressure on the external surface of nanostructures according to Gurtin's surface elasticity theory. Computational results illustrate that this method can well capture the experimentally observed strengthened and softened effects when the characteristic size approaches tens of nanometers. More importantly, the computational method enables the investigation of size effects for complex structures, which are beyond the capability of conventional analytical methods. The first example of complex structure also reveals the critical size below which the size effects becomes notable is 20 nm, much smaller than 50 nm of beams with both ends fixed. Parametric studies on the initial surface tension and surface stiffness show that the former is a predominant factor. The weakened Young's modulus is found in a complex cantilever which is produced from structural topology optimisation. This computational method also indicates the potential of introducing structural topology optimisation into nanostructures design as two illustrating examples clearly show that the size effects is highly dependent on the structural shape and topology at the nanoscale level.

CHAPTER 4

NUMERICAL APPLICATION OF SIZE EFFECTS ON BENDING BASED ELEMENTS

The framework of surface elasticity theory and generalized Young-Laplace equation has been proved to be effective and efficient to account for the experimentally observed size effects in the last two chapters. Due to the inherent natural of theoretical analysis, it can only be applied to models with very simple geometries and loading conditions. Though the theoretical analysis is correct, it is tractable analytically only for simple elementary cells, even for the unit cell in Chapter 2 it needs rather long calculations. So the best way to used this framework is to solve problems numerically. It is noticed in the generalized Young-Laplace equation that the key issue of determining the size effects lays in the determination of the curvature of the deformed material surface. In the iterative finite element method proposed in chapter 2, compromise is made in order to use the conventional solid element. The iterative process has to be adapt to calculate the curvature of the deformed shape since in the formulation of solid element no information on the curvature of the material surface can be explicitly obtained. And the curvature can only be solved from the inter-element information, to be more spacific, from the displacement of a series of nodes from different element alone the material surface. This is the motivation for the works in this chapter. It is well known that the general strain of bending base elements, such as beam and shell, is curvature (Bathe, 2006). This makes it possible to formulate a series of bending based element with size effects include.

4.1 Introduction

The size effects refer to the abnormal changes of mechanical properties when the characteristic sizes of nanomaterials or nanostructures are less than 100 nm (Chen et al., 2006a; Cuenot et al., 2004; Lee et al., 2007b; Lukic et al., 2005). Since the rapid increase of Young's modulus and

flexural rigidity at the level of nanoscale were experimentally detected by using three-point bending tests (Salvetat et al., 1999; Tombler et al., 2000), nano-indentation (Volkert et al., 2006), atomic force microscopy (Lucas et al., 2008), and Raman spectroscopy (Lourie and Wagner, 1998), size effects have attracted intense attention as they could be used in many fields like lightweight materials, sensors, and actuators (Hodge et al., 2007; Lu et al., 2014; Meza et al., 2014).

One of the most challenging problems in size effects is the establishment of an appropriate approach to evaluating the dependence of effective properties on the characteristic size. The first estimation was made by the well-known Gibson-Ashby model (Gibson and Ashby, 1999). which estimates the effective Young's modulus E^* of an open-cell foam material with a density of ρ by $E^*/E_0 = C(\rho/\rho_0)^2$, in which the density and Young's modulus of the bulk material are represented by ρ_0 and E_0, respectively. The constant C is to be determined experimentally. An alternative is to use the molecular dynamics simulation to predict the mechanical properties at the atomic level (Biener et al., 2006). Considering the huge amount of particles to be included in the numerical model, this approach is computationally inefficient even for ordinary scale nanostructures (Park and Klein, 2008).

Recent studies show that the strengthened or weakened mechanical properties are attributed to the strong interactions of atoms and their clusters on the material surface when the surface-to-volume ratio is extremely large at nanoscale (Dou et al., 2010; Hodge et al., 2007; Weissmuller et al., 2009). Based on this fundamental conjecture, scientists have learned how to theoretically explain such abnormal changes using a core-shell model in continuum mechanics (Dou et al., 2010; Hodge et al., 2007; Wang and Feng, 2007; Weissmuller et al., 2009). And they found the main reasons for the size effects are ascribed to the surface residual tension and surface stiffness induced by the material disparity between the superficial layer and inner core (Chen et al., 2006c; Gurtin et al., 1998).

Later, a framework of surface elasticity (Gurtin et al., 1998). and generalized Young-Laplace equation (Chen et al., 2006c). was integrated with the beam theory to study the size effects for a ZnO nanowire and a nanostructure. The dependence of Young's modulus on the characteristic size obtained by this approach shows the similar trend to the experimental results (He and Lilley, 2008; Lu et al., 2014). The aforementioned theoretical studies are based on the models of simple beams and regular beam systems, which are theoretically viable but geometrically dissimilar

to nanostructures. Later, an iterative finite element method was proposed to directly simulate the deformation of complex nanostructures under the curvature-dependent pressure resulting from the size effects (Lu et al., 2015). Though this computational approach can be used to validate the experimental data for randomly-shaped nanoporous structures, it is inapplicable to the nanostructures less than 10 nm due to the low efficiency and misconvergence at such a small scale. It is necessary to develop a finite element scheme that includes the size effects for bending base element. The combination of generalized Young-Laplace equation and surface elasticity is adapted to introduce the size effects into this new method.

4.2 Formulation of the finite element method with size effects

The surface elasticity theory and generalized Young-Laplace equation are combined to study the size effects for the beam with circular cross-section. For completeness, they are briefly reviewed before incorporating them into the Euler-Bernoulli and Timoshenko beam theories.

According to the surface elasticity theory (Gurtin and Ian Murdoch, 1975), the surface stress $\tau^s_{\alpha\beta}$, a symmetric 2×2 tensor on the tangent plane to the surface, is given in Equation (1.18). By assuming that the surface is homogeneous, isotropic, and linearly elastic, the overall surface stress τ along the longitudinal direction of a beam can be simplified to Equation (1.19).

According to generalized Young-Laplace equation, a stress jump $\Delta\sigma_{ij}$ across the interface depends on the surface curvature $\kappa_{\alpha\beta}$ and the surface stress $\tau_{\alpha\beta}$ exists and could be express as Equation (2.2).

The surface effects considering the initial surface stress are converted into curvature-dependent pressure $q(x)$ along the normal direction of beam surface, as shown in Figure 4.1.

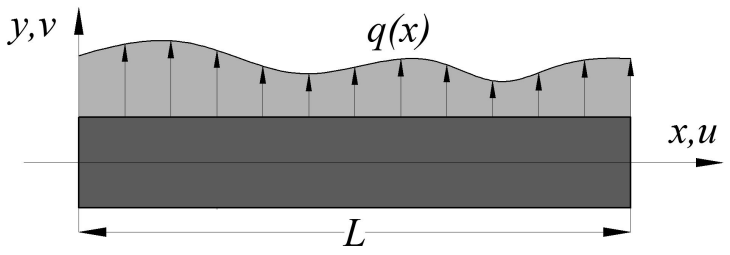

Figure 4.1: The schematic of pressure $q(x)$ resulted from the size effects

In continuum mechanics, the deformation of a beam is composed of axial displacement u

and bending deflection w. Noted that the introduction of size effects in traditional beam theories only influences the deflection w while the axial displacement remains the same. Following this assumption, the following finite element analysis brings out a new element stiffness matrix for a 2D circular cross-section beam. Its extension to 3D is straightforward if the deformations in axial and radial directions are considered.

According to the principle of virtual displacements, the virtual external work of real external forces moving through collocated virtual displacements equals the internal virtual work of real stresses in equilibrium with real forces with the virtual strains compatible with the virtual displacements integrated over the volume of the solid(Lanczos, 1970) and can be mathematically expressed as:

$$\delta W_I = \delta W_E \tag{4.1}$$

$$\int_w \sigma \cdot \delta\varepsilon dV = \int_w \delta U^T f^B dV + \int_S \delta U^{ST} f^s dV + \sum_i \delta U^{iT} F^i \tag{4.2}$$

where δW_I is the total internal virtual work, and δW_E is the total external virtual work. σ is the actual stress, $\delta\varepsilon$ is the virtual strains. f^b, f^s and F^i are the actual external body force, surface traction and concentrated force and δU^T, δU^{ST} and δU^{iF} are the corresponding virtual displacement. In the following sections apart from the conventional virtual work, the exact expression of the contributions from surface elasticity and generalized Young-Laplace equation to the virtual internal and external work will be derived for three bending based element, namely the Euler-Bernoulli beam, the Timoshenko beam and thin plate. New weak form for the elements will be obtained.

4.2.1 Weak form for Euler-Bernoulli beam theory with size effects

Regarding Euler-Bernoulli beam theory, the z-axial displacement is neglected and the x-component displacement u is given as:

$$u(x, y) = -y\frac{\partial w(x)}{\partial x} = -yw' = -y\theta \tag{4.3}$$

with y the distance of a material point to the neutral plane, and the deflection $w(x, y) = w(x)$ only relies on x, and the rotation angle is $\theta = \partial w/\partial x = dw/dx$. The longitudinal strain can be

determined by differentiating the axial displacement $u(x, y)$ of Equation (4.3) as:

$$\varepsilon = \frac{\partial u}{\partial x} = -y\frac{\partial^2 w}{\partial x^2} = -y\frac{d^2 w}{dx^2} = -yx'' \approx -y\kappa \tag{4.4}$$

where $\kappa \approx w''$ denotes the curvature of the neutral axis, and it can be approximated as the second derivative of deflection. Based on the Hooke's law, the stress σ is related to ε as

$$\sigma = E\varepsilon = -Ey\frac{d^2 w}{dx^2} = -Ey\kappa \tag{4.5}$$

where E is the elastic modulus. The bending moment M is calculated from the area integration over the cross-section, given as:

$$M = \int_A -y\sigma dA = E\kappa \int_A y^2 dA = EI\kappa \tag{4.6}$$

where I denotes the moment of inertia of the cross-section. EI is the bending rigidity.

The total internal virtual work δW_I of an Euler-Bernoulli beam with consideration of surface effects is given as:

$$\delta W_I = \delta W_{IC} + \delta W_{IS} \tag{4.7}$$

where the subscript $_{IC}$ and $_{IS}$ denote the conventional part and surface effects part of internal virtual work, respectively. In terms of Euler-Bernoulli beam theory, item δW_{IC} is given by:

$$\delta W_{IC} = \int_0^L M_c \kappa dx = \int_0^L w'' EI w'' dx \tag{4.8}$$

where M_c is the bending moment which is the same as the traditional definition in Equation (4.6). The second term δW_{IS} on the right side of Equation (4.7) relates to the surface effects, and its elaborated derivation is given below.

For a representative infinitesimal edge element on the perimeter of the cross-section with diameter D, as shown in Figure 4.1, the axial strain is (Gere and Timoshenko, 1990):

$$\varepsilon_s = -\frac{D}{2}\sin\theta\kappa \tag{4.9}$$

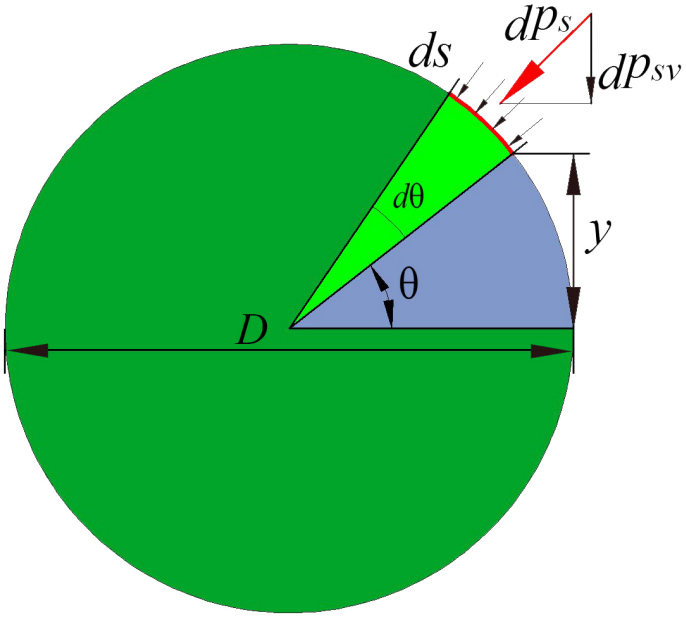

Figure 4.2: The cross-sectional profile of the pressure $q(x)$ from the size effects along the section edge

Then the surface stress along the axial direction in Equation (1.19), as shown in Figure 4.3, becomes:

$$\tau_{axial} = \tau_0 - E_s \frac{D}{2} \sin\theta\kappa \tag{4.10}$$

In an infinitesimal arc (red curve in Figure 4.2), this surface stress results in an extra moment about the neutral plane as:

$$dM_s = -\tau_{axial} y ds = (E_s \frac{D}{2} \sin\theta\kappa - \tau_0) \frac{D^2}{4} \sin\theta d\theta \tag{4.11}$$

Therefore, the contribution of the surface effects to the internal work δW_I is determined as:

$$\delta W_{IS} = \int_0^L M_s \kappa dx = \int_0^L M_s w'' dx = \int_0^L w'' \frac{\pi D^3}{8} E_s w'' dx \tag{4.12}$$

Then, the overall internal virtual work can be obtained as:

$$\delta W_I = \delta W_{IC} + \delta W_{IS} = \int_0^L w'' EI w'' dx + \int_0^L w'' \frac{\pi D^3}{8} E_s dx \tag{4.13}$$

This equation indicates the beam element has an effective bending modulus of $EI+EsD3/8$. Noted that similar expression was reported by He *et at.* (He and Lilley, 2008).

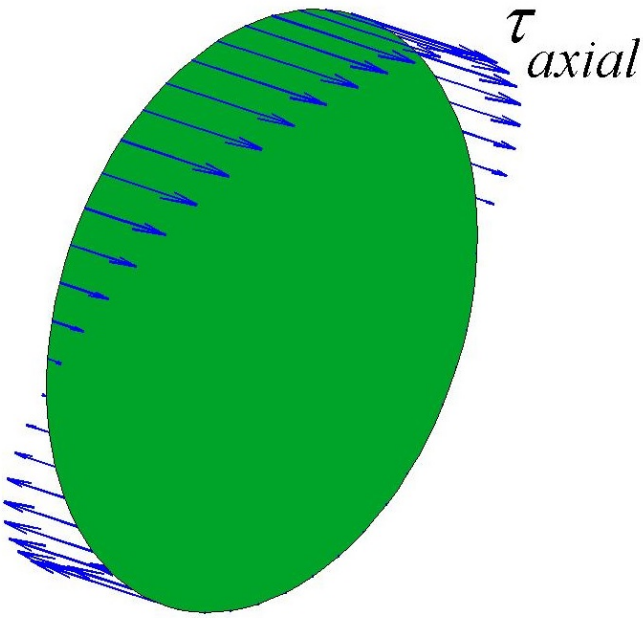

Figure 4.3: The surface tension, derived from the surface elasticity theory, in the longitudinal direction along the edge of the cross-sectional of the beam

The conventional part of the external virtual work δW_E is straightforward given as:

$$\delta W_{EC} = \int_0^L q_c w dx \tag{4.14}$$

where q_c is the transverse force per unit length acting alone the beam, here the subscript $_{EC}$ denotes the conventional part of external virtual work. With consideration of the surface effects, δW_{ES} can be derived similarly, where the subscript $_{ES}$ denotes the surface effects part of external virtual work. According to generalized Young-Laplace equation, the axial surface stress will lead to a loading dp_s which is normal to the infinitesimal edge element (as shown in Figure 4.2). It is expressed as:

$$dp_s = \tau_{axial}\kappa\frac{D}{2}d\theta \tag{4.15}$$

Owing to the symmetry condition, only the component of dp_sin the flexure plane contributes to the external virtual work and it can be obtained by decomposition:

$$dp_{sv} = dp_s \sin\theta = \tau_{axial}\kappa\frac{D}{2}\sin\theta d\theta \tag{4.16}$$

The overall surface induced transverse load can be found by integrating dp_{sv} along the perimeter as:

$$q_s = \int dp_{sv} ds = 2\tau_0 D\kappa \tag{4.17}$$

Again, the expression in Equation (4.17) is consistent with the distributed transverse force reported in (He and Lilley, 2008; Wang and Feng, 2007).

Then the surface effects part of the external work δW_{ES} is determined as:

$$\delta W_{ES} = \int_0^L q_s w dx = \int_0^L 2\tau_0 D\kappa w dx = \int_0^L w(2\tau_0 D)w'' dx \tag{4.18}$$

Therefore the total external virtual work can be computed by:

$$\delta W_E = \delta W_{EC} + \delta W_{ES} = \int_0^L q_c w dx + \int_0^L w(2\tau_0 D)w'' dx \tag{4.19}$$

In accordance with principle of virtual displacement, the external virtual work δW_E equals to the internal virtual work δW_I, eventually, by substituting Equations (4.13) and 4.19 into Equation (4.1), we can obtain:

$$\int_0^L w'' EI w'' dx + \int_0^L w'' \frac{\pi D^3}{8} E_s w'' dx = \int_0^L q_c w dx + \int_0^L w(2\tau_0 D)w'' dx \tag{4.20}$$

By rearranging the last term to the left side, this equation becomes:

$$\int_0^L w'' EI w'' dx + \int_0^L w'' \frac{\pi D^3}{8} E_s w'' dx - \int_0^L w(2\tau_0 D)w'' dx = \int_0^L q_c w dx \tag{4.21}$$

The expression in Equation (4.21) is similar to the weak form of the equilibrium equation in finite element analysis. But it has two additional terms: the second term on the left side changes the effective bending rigidity while the third one comes from the extra transverse load. It is interesting to note that the terms $EI + \pi D^3 E_s/8$ and $2\tau_0 D$ in Equation (4.21) have been reported in their pioneering studies (He and Lilley, 2008) in the form of effective flexural rigidity and the coefficient resulted from the distributed transverse force.

4.2.2 Weak form for Timoshenko beam theory with size effects

Following the similar routine, the formulation of the element stiffness matrix for Timoshenko beam element with size effects is derived in this section. The stiffness matrix for extended Timoshenko beam element comprises contributions from axial compression, torsional and bending. Axial and torsional effects are considered in the conventional manner (Gere and Timoshenko, 1990).

The bending contribution is formulated under Timoshenko beam theory. Element stiffness is derived from a 2D circular cross-section beam model with only bending considered for simplicity, extending to 3D is straightforward. The axial $u(x, y)$ and transverse $w(x, y)$ displacements in the x-y plane is used to describe the motion of an arbitrary material point on the beam. Here motion in z direction is not considered. The kinematic assumption of Timoshenko beam theory can be represented as:

$$\begin{aligned} u(x,y) &= -y(\tfrac{\partial w(x)}{\partial x} + \gamma) \\ w(x,y) &= w(x) \\ \theta_z &= \tfrac{\partial w}{\partial x} + \gamma = w' + \gamma \\ \gamma &= \tfrac{w}{GA_s} \end{aligned} \tag{4.22}$$

here θ_z is the rotation angle and γ is angle of shearing. y is the distance of a material point to the neutral plane.

The strain can be determined by differentiating the displacement in Equation (4.22) as:

$$\varepsilon_{11} = -y\frac{\partial \theta_z}{\partial x} \tag{4.23}$$

$$\varepsilon_{13} = \frac{1}{2}(\theta_z - \frac{\partial w}{\partial x}) = \frac{1}{2}\gamma \tag{4.24}$$

Based on the Hooke's law (Zienkiewicz et al., 1977), the stress component can be obtained as,

$$\sigma_{11} = E\varepsilon_{11} \tag{4.25}$$

$$\sigma_{13} = G\gamma \tag{4.26}$$

where E is the elastic modulus, G is the shear modulus.

The axial stress σ_{11} will cast a bending moment to the neutral axis. And this bending

moment M over the cross-section is calculated from the integral,

$$M = \int_A -y\sigma_{11} dA \tag{4.27}$$

The overall internal virtual work of Timoshenko beam including surface effects can be express as:

$$\delta W_I = \delta W_{IC} + \delta W_{IS} \tag{4.28}$$

where δW_I denote the overall internal virtual, work and it is consist of the contribution from the conventional bending and shearing effects and the contribution of surface effects from initial surface tension and surface stiffness, denoted as δW_{IC} and δW_{IS} correspondingly. The Timoshenko beam theory assumes that the internal energy of beam member is due to bending and shearing which can be expressed as:

$$\delta W_{IC} = \int_0^L EI(\frac{\partial \theta_z}{\partial x})^2 dx + \int_0^L \kappa AG(\theta_z + \frac{\partial w}{\partial x})^2 dx \tag{4.29}$$

here I denotes the moment of inertia of the cross-section, EI is the flexure rigidity, κ denotes the shear area coefficient and $\kappa = 10/9$ for solid circular sections, A is the cross-section area of the beam considered (Cowper, 1966).

For a representative infinitesimal surface element on the surface of the cross-section display as red arc in Figure 4.2, according to Equation (4.25) the longitudinal strain, which is perpendicular to the cross-sectional plane, is,

$$\varepsilon_s = -\frac{D}{2} \sin\alpha \frac{\partial \theta_z}{\partial x} \tag{4.30}$$

Base on Equation (1.19), the surface stress along beam axis can be expressed, as shown in Figure 4.3, as:

$$\begin{aligned} \tau_{axial} &= \tau_0 + E_s \varepsilon_s \\ &= \tau_0 + E_s(-\frac{D}{2} \sin\alpha \frac{\partial \theta_z}{\partial x}) \end{aligned} \tag{4.31}$$

This surface stress along beam axis introduces an extra moment on the infinitesimal surface

element to the neutral axis of this cross-scetion which can be express as:

$$\begin{aligned} dM_s &= -\tau_{axial} y ds \\ &= -(\tau_0 + E_s(-\frac{D}{2}\sin\alpha\frac{\partial\theta_z}{\partial x}))\frac{D}{2}\sin\alpha\frac{D}{2}d\alpha \end{aligned} \tag{4.32}$$

By integrate the listed bending moment dM_s along the perimeter of the cross-section of the beam, the overall additional moment derived from the surface effects at this cross-section x can be obtained as,

$$\begin{aligned} M_s &= \int dM_s \\ &= \int_0^{2\pi} -(\tau_0 + E_s(-\frac{D}{2}\sin\alpha\frac{\partial\theta_z}{\partial x}))\frac{D}{2}\sin\alpha\frac{D}{2}d\alpha \\ &= \frac{\pi D^3}{8}E_s\frac{\partial\theta_z}{\partial x} \end{aligned} \tag{4.33}$$

The contribution from the surface effects to the virtual internal work δW_{IS} of this beam under Timoshenko beam theory is then determined as:

$$\begin{aligned} \delta W_{IS} &= \int_0^L M_s\frac{\partial\theta_z}{\partial x}dx \\ &= \int_0^L \frac{\pi E_s D^3}{8}(\frac{\partial\theta_z}{\partial x})^2 dx \end{aligned} \tag{4.34}$$

The overall internal virtual work is then obtained as:

$$\begin{aligned} \delta W_I &= \delta W_{IC} + \delta W_{IS} \\ &= \int_0^L EI(\frac{\partial\theta_z}{\partial x})^2 dx + \int_0^L \kappa AG(\theta_z + \frac{\partial w}{\partial x})^2 dx \\ &\quad + \int_0^L \frac{\pi E_s D^3}{8}(\frac{\partial\theta_z}{\partial x})^2 dx \end{aligned} \tag{4.35}$$

The external virtual work δW_E also consists of the conventional part δW_{EC} and the surface

effects part δW_{ES}. The conventional part is the work done by the external distributed load as:

$$\delta W_{EC} = \int_0^L q_c w dx \tag{4.36}$$

where q_c is the transverse force per unit length that acts along the beam axis.

According to generalized Young-Laplace equation the surface tension alone the beam longitudinal direction, as shown in Figure 4.3, will cause an additional distributed pressure in the normal direction of the surface, as shown in Figure 4.2 as red arrow, which can be expressed as:

$$p_s = \tau_{axial} \frac{\partial \theta_z}{\partial x} \frac{D}{2} \sin \alpha d\alpha \tag{4.37}$$

Due to the symmetric nature of the beam, only the force component acting along the deflection direction in the flexure plane can do work and contributes to the external virtual work, and this part of the force can be obtained by decomposition p_s to the deflection direction as,

$$\begin{aligned} p_{s\_flexure} &= p_s \sin \alpha \\ &= \tau_{axial} \frac{\partial \theta_z}{\partial x} \frac{D}{2} \sin \alpha d\alpha \sin \alpha \end{aligned} \tag{4.38}$$

By integrating the $p_{s\_flexure}$ component around the perimeter of the cross-section of the beam, the total surface effects induced transverse load q_s at this cross-section can be obtained as:

$$\begin{aligned} q_s &= \int \tau_{axial} \frac{\partial \theta_z}{\partial x} \sin \alpha ds \\ &= \int_0^{\pi} \frac{D}{2} \frac{\partial \theta_z}{\partial x} (\tau_0 - E_s \sin \alpha \frac{D}{2} \frac{\partial \theta_z}{\partial x}) \sin \alpha d\alpha \\ &\quad - \int_{\pi}^{2\pi} \frac{D}{2} \frac{\partial \theta_z}{\partial x} (\tau_0 - E_s \sin \alpha \frac{D}{2} \frac{\partial \theta_z}{\partial x}) \sin \alpha d\alpha \\ &= 2\tau_0 D \frac{\partial \theta_z}{\partial x} \end{aligned} \tag{4.39}$$

Therefore the contribution from surface effects to the overall external work δW_{ES} can then

be expressed as,

$$\begin{aligned} \delta W_{ES} &= \int_0^L q_s w dx \\ &= \int_0^L 2\tau_0 D \frac{\partial \theta_z}{\partial x} w dx \end{aligned} \tag{4.40}$$

The total external virtual work δW_E of this Timoshenko beam with surface effects considered is then determined as:

$$\begin{aligned} \delta W_E &= \delta W_{EC} + \delta W_{ES} \\ &= \int_0^L q_c w dx + \int_0^L 2\tau_0 D \frac{\partial \theta_z}{\partial x} w dx \end{aligned} \tag{4.41}$$

Then the virtual displacement principle of Timoshenko beam with surface effects included can be obtained, according to Equation (4.1), as:

$$\begin{aligned} \int_0^L EI(\frac{\partial \theta_z}{\partial x})^2 dx + \int_0^L \kappa AG(\theta_z + \frac{\partial w}{\partial x})^2 dx + \int_0^L \frac{\pi E_s D^3}{8}(\frac{\partial \theta_z}{\partial x})^2 dx \\ = \int_0^L q_c w dx + \int_0^L 2\tau_0 D \frac{\partial \theta_z}{\partial x} w dx \end{aligned} \tag{4.42}$$

Compared Equation (4.42) with that of ordinary beam element(Zienkiewicz et al., 1977), after some rearrangement of Equation (4.42), the new weak form that is corresponding to the Timoshenko beam element with surface effects considered becomes,

$$\begin{aligned} \int_0^L EI(\frac{\partial \theta_z}{\partial x})^2 dx + \int_0^L \kappa AG(\theta_z + \frac{\partial w}{\partial x})^2 dx \\ + \int_0^L \frac{\pi E_s D^3}{8}(\frac{\partial \theta_z}{\partial x})^2 dx - \int_0^L 2\tau_0 D \frac{\partial \theta_z}{\partial x} w dx = \int_0^L q_c v dx \end{aligned} \tag{4.43}$$

Following the standard finite element discretization scheme, by introducing the displacement interpolation matrix and strain-displacement matrix, the stiffness matrix of the extended Timoshenko beam element with surface effects can be obtained. The detailed finite element implementation is out of the scope of this section.

4.2.3 Weak form for the thin plate with size effects

Similar to the previous sections, the principle of virtual displacement is used in the process of deriving the weak form of the thin plate. The formulation of the thin plate element including deriving internal and external energy, δW_I and δW_E, which are composed of conventional part and surface effects related part δW_{IC}, δW_{EC} and δW_{IS}, δW_{ES} as well.

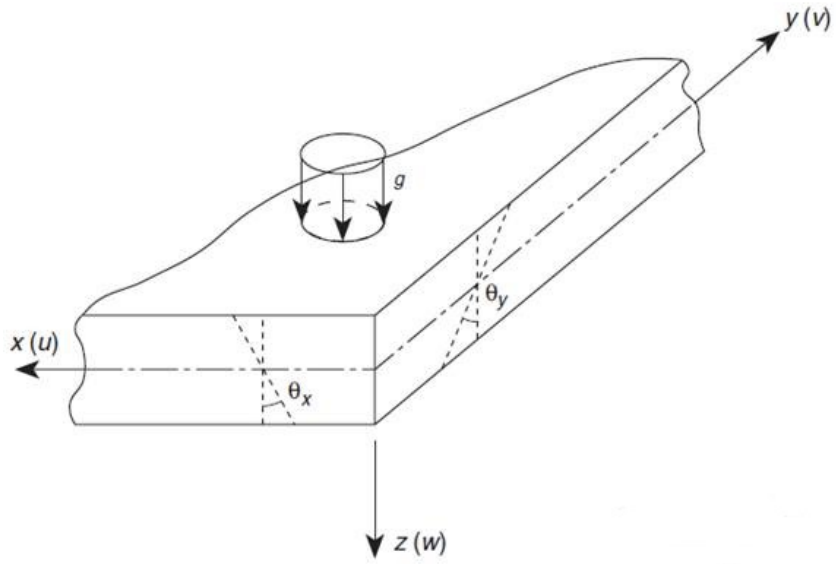

Figure 4.4: The kinematics of a thin plate: the definition of displacement and rotation for the plate (Zienkiewicz et al., 1977)

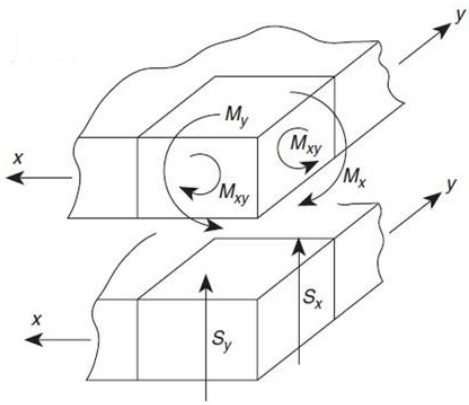

Figure 4.5: The kinematics of a thin plate: the definition of moment and forces for a plate (Zienkiewicz et al., 1977)

According to the kinematics of thin plate, as shown in Figure 4.4 and 4.5. The displacement

of a material point in the plate can be expressed as:

$$\begin{aligned} u &= -z\theta_x(x,y) \\ v &= -z\theta_y(x,y) \\ w &= w_0(x,y) \end{aligned} \tag{4.44}$$

where θ_x and θ_y are the rotations of the neutral plane of the plate with respect to x and y axis, w_0 is the deflection in the normal direction of the plate, with y the distance of a material point to the neutral plane.

The strain can be determined by differentiating the displacements of Equations 4.44 as:

$$\begin{aligned} \varepsilon &= \begin{bmatrix} \varepsilon_x \\ \varepsilon_y \\ \gamma_{xy} \end{bmatrix} = -z \begin{bmatrix} \frac{\partial}{\partial x} & 0 \\ 0 & \frac{\partial}{\partial y} \\ \frac{\partial}{\partial y} & \frac{\partial}{\partial x} \end{bmatrix} \begin{bmatrix} \theta_x \\ \theta_y \end{bmatrix} = -z\mathbf{L}\theta, \mathbf{L} = \begin{bmatrix} \frac{\partial}{\partial x} & 0 \\ 0 & \frac{\partial}{\partial y} \\ \frac{\partial}{\partial y} & \frac{\partial}{\partial x} \end{bmatrix} \\ \gamma &= \begin{bmatrix} \gamma_{xz} \\ \gamma_{yz} \end{bmatrix} = \begin{bmatrix} \frac{\partial w}{\partial x} \\ \frac{\partial w}{\partial y} \end{bmatrix} - \begin{bmatrix} \theta_x \\ \theta_y \end{bmatrix} = \nabla \mathbf{w} - \theta, \nabla = \begin{bmatrix} \frac{\partial}{\partial x} \\ \frac{\partial}{\partial y} \end{bmatrix} \end{aligned} \tag{4.45}$$

where ε and γ are the normal strain and shear strain respectively, $\mathbf{L}$ and ∇ are differential operators as listed. Under the assumption of thin plate theory (Bathe, 2006), the shear deformations out of plane are disregarded, which lead to:

$$\gamma = \mathbf{0} = \nabla \mathbf{w} - \theta \tag{4.46}$$

According to Hooke's law (Zienkiewicz et al., 1977) the stress for thin plate has three component and can be determined as:

$$\begin{bmatrix} \sigma_x \\ \sigma_y \\ \tau_{xy} \end{bmatrix} = \frac{E}{1-\nu^2} \begin{bmatrix} 1 & \nu & 0 \\ \nu & 1 & 0 \\ 0 & 0 & (1-\nu)/2 \end{bmatrix} \begin{bmatrix} \varepsilon_x \\ \varepsilon_y \\ \gamma_{xy} \end{bmatrix} = \mathbf{E}\varepsilon \tag{4.47}$$

where E and ν are the Young's modulus and Poison's ratio of the constitutive material of the plane respectively.

The surface strain of the deformed thin plate can be expressed as:

$$\varepsilon_s = \varepsilon \Big|_{z=\pm t/2} = \begin{bmatrix} \frac{t}{2}\mathbf{L}\nabla\mathbf{w} \\ \\ -\frac{t}{2}\mathbf{L}\nabla\mathbf{w} \end{bmatrix} \tag{4.48}$$

By using the surface elasticity theory (Gurtin and Ian Murdoch, 1975), the surface stress derived from this surface strain can be expressed as:

$$\tau_{\mathbf{s}} = \tau_0 + E_s\varepsilon \Big|_{z=\pm t/2} = \begin{bmatrix} \tau_0 + E_s\frac{t}{2}\mathbf{L}\nabla\mathbf{w} \\ \\ \tau_0 - E_s\frac{t}{2}\mathbf{L}\nabla\mathbf{w} \end{bmatrix} \tag{4.49}$$

noted here only the effects of the normal surface strain is considered for simplicity.

The contribution of surface effects to the virtual internal work of thin plate can be obtained as:

$$\begin{aligned} \delta W_{IS} &= \int_{\Omega} (\delta\varepsilon_s)^T \tau_s d\Omega = \int_{\Omega} \begin{bmatrix} \frac{t}{2}\mathbf{L}\nabla\mathbf{w} \\ \\ -\frac{t}{2}\mathbf{L}\nabla\mathbf{w} \end{bmatrix}^T \begin{bmatrix} \tau_0 + \mathbf{E_s}\frac{t}{2}\mathbf{L}\nabla\mathbf{w} \\ \\ \tau_0 - \mathbf{E_s}\frac{t}{2}\mathbf{L}\nabla\mathbf{w} \end{bmatrix} d\Omega \\ &= \frac{t^2}{4}\mathbf{E_s}\int_{\Omega} \delta w(\mathbf{L}\nabla)^T(\mathbf{L}\nabla) w d\Omega \end{aligned} \tag{4.50}$$

where Ω is the integration domain, here is the area of the neutral plane of the thin plate.

And the overall virtual internal work of the thin plate is:

$$\begin{aligned} \delta W_I &= \delta W_{IC} + \delta W_{IS} \\ &= \int_{\Omega} \delta w(\mathbf{L}\nabla)^T(\mathbf{D} + \frac{t^2}{4}\mathbf{E_s})(\mathbf{L}\nabla) w d\Omega \end{aligned} \tag{4.51}$$

Follow the same procedure, the additional surface load derived from the surface stress of surface elasticity in Equation (4.49) will cast an additional distributed pressure in the normal direction of the thin plate due to generalized Young-Laplace equation as:

$$p_s = {\tau_{\mathbf{s}}}^T\kappa = \begin{bmatrix} \tau_0 + E_s\frac{t}{2}\mathbf{L}\nabla\mathbf{w} \\ \\ \tau_0 - E_s\frac{t}{2}\mathbf{L}\nabla\mathbf{w} \end{bmatrix}^T \mathbf{L}\nabla\mathbf{w} = 2\tau_0\mathbf{L}\nabla\mathbf{w} \tag{4.52}$$

where κ is the curvature tensor of the deformed thin plate expressed as:

$$\kappa = \begin{bmatrix} \kappa_{xx} \\ \kappa_{xx} \\ \kappa_{xy} \end{bmatrix} = \begin{bmatrix} \frac{\partial^2 w}{\partial x^2} \\ \frac{\partial^2 w}{\partial y^2} \\ \frac{\partial^2 w}{\partial x \partial y} \end{bmatrix} = \mathbf{L}\nabla\mathbf{w} \tag{4.53}$$

This additional distributed pressure from generalized Young-Laplace equation is acting along the deflection direction and consequently will cause additional external work δW_{ES}, due to the deflection in normal direction of neutral plane w, as:

$$\begin{aligned} \delta W_{ES} &= \int_{\Omega} \delta w p_s d\Omega \\ &= \int_{\Omega} \delta w 2\tau_0 (\mathbf{L}\nabla) w d\Omega \end{aligned} \tag{4.54}$$

And the overall external work of the thin plate is then obtained as:

$$dW_E = dW_{EC} + dW_{ES} = \int_{d\Omega} \delta w q_c d\Omega + \int_{\Omega} \delta w 2\tau_0 (\mathbf{L}\nabla) w d\Omega \tag{4.55}$$

According to the principle of virtual displacements Equation (4.1), the virtual external work should equals to the internal virtual work(Lanczos, 1970), and this leads to:

$$\int_{\Omega} \delta w (\mathbf{L}\nabla)^T (\mathbf{D} + \frac{t^2}{4}\mathbf{E_s})(\mathbf{L}\nabla) w d\Omega = \int_{d\Omega} \delta w q_c d\Omega + \int_{\Omega} \delta w 2\tau_0 (\mathbf{L}\nabla) w d\Omega \tag{4.56}$$

After some rearrangement, the weak form of thin plate with size effects included is obtained as:

$$\int_{\Omega} \delta w (\mathbf{L}\nabla)^T (\mathbf{D} + \frac{t^2}{4}\mathbf{E_s})(\mathbf{L}\nabla) w d\Omega - \int_{\Omega} \delta w 2\tau_0 (\mathbf{L}\nabla) w d\Omega = \int_{d\Omega} \delta w q_c d\Omega \tag{4.57}$$

Following the standard finite element discretization scheme, by introducing the displacement interpolation matrix and strain-displacement matrix, the stiffness matrix of the extended Timoshenko beam element with surface effects can be obtained. The detailed finite element

implementation is out of the scope of this section.

4.3 Finite element implementation of Euler-Bernoulli beam with size effects

To complement previous work, this section aims to develop a finite element method capable of evaluating the size effects for complex structures at any level of scale. With the assumption that the complex nanoporous structures are composed of a system of inter-connected beams (Sears and Batra, 2004), we explicitly incorporate the size effects derived from the surface elasticity and generalized Young-Laplace equation into the element stiffness matrix. Numerical tests indicate that this method provides the exactly same size effects for a cantilever beam as the theoretical study in (He and Lilley, 2008), and very similar data to the one for a cubic unit cell containing 24 horizontal/vertical ligaments (Feng et al., 2009). The computational results for a simply-supported beam and the nanoporous gold match the experimental data (Jing et al., 2006; Lee et al., 2007a) within an acceptable margin of error. According to the standard finite element discretization scheme, the detailed implementation of the Euler-Bernoulli beam theory with size effects in 2D with only bending considered is list hereafter, the extending of this model to 3D with axial tension and torsion is straight forward.

4.3.1 Element stiffness matrix of Euler-Bernoulli beam with size effects

In finite element analysis, the elemental deflection is $w = \mathbf{N}\mathbf{u}^e$, in which the interpolation function $\mathbf{N}$ is a 1×4 vector and the nodal displacement vector u^e is a 4×1

The element nodal displacement vector $\mathbf{u}^e$ contains nodal deflection and rotation as,

$$\mathbf{u}^e = \begin{bmatrix} w_1 \\ \theta_1 \\ w_2 \\ \theta_2 \end{bmatrix} \tag{4.58}$$

where the subscript 1 and 2 indicate the two end nodes, node one and node two in a beam.

The displacement interpolation matrix $\mathbf{N}$, which relates the nodal displacements with the

deflection in the beam, can be express as,

$$\mathbf{N} = \begin{bmatrix} \frac{1}{4}(1-\xi)^2(2+\xi) \\ \frac{1}{8}l(1-\xi)^2(1+\xi) \\ \frac{1}{4}(1+\xi)^2(2-\xi) \\ -\frac{1}{8}l(1+\xi)^2(1-\xi) \end{bmatrix} \tag{4.59}$$

with $\xi = 2x/l - 1$ as the dimensionless natural coordinate. Note that there exist different forms of the dimensionless natural coordinate depending on the choice of origin.

For beam, the generalized strain is curvature κ, and corresponding generalized stress is moment M (Bathe, 2006). The generalized strain κ could be obtained by differentiating the deflection twice with respect to x:

$$\kappa = w'' = \frac{d^2w}{dx^2} = \mathbf{B}\mathbf{u}^e = \mathbf{N}''\mathbf{u}^e \tag{4.60}$$

where $\mathbf{B}$ is the strain-displacement matrix, which relates the nodal displacements with the generalized strain. The strain-displacement matrix $\mathbf{B}$ has the same dimension as $\mathbf{N}$ and can be obtained as the second derivative of $\mathbf{N}$ with respect to the natural coordinate ξ as,

$$\mathbf{B} = \frac{1}{l}\begin{bmatrix} 6\frac{\xi}{l} \\ 3\xi - 1 \\ -6\frac{\xi}{l} \\ 3\xi + 1 \end{bmatrix} \tag{4.61}$$

Substituting the matrix form of w and w'' into the virtual displacement principle equation, Equation (4.21), of this element could get finite element notion of the element equilibrium equation as,

$$\int_0^L \mathbf{u}^{eT}\mathbf{B}^T(EI + \frac{\pi D^3}{8}E_s)\mathbf{B}\mathbf{u}^e dx = \int_0^L q_c\mathbf{N}\mathbf{u}^e dx + \int_0^L \mathbf{u}^{eT}\mathbf{N}^T(2\tau_0 D)\mathbf{B}\mathbf{u}^e dx \tag{4.62}$$

With some rearrangement of the equilibrium equation, the equilibrium equations that

correspond to the nodal point displacements of the element in finite element notation becomes

$$\mathbf{u}^{eT}[\int_0^L \mathbf{B}^T(EI + \frac{\pi D^3}{8}E_s)\mathbf{B}dx - \int_0^L \mathbf{N}^T(2\tau_0 D)\mathbf{B}dx]\mathbf{u}^e = \mathbf{u}^{eT}[\int_0^L \mathbf{N}^T q_c dx] \tag{4.63}$$

this is, in fact, the discretized finite element notion of the weak form of the beam element with size effects included.

The element stiffness matrix $\mathbf{K^e}$ of Euler-Bernoulli beam theory with size effects is then obtained as,

$$\mathbf{K}^e = \int_0^L \mathbf{B}^T(EI + \frac{\pi D^3}{8}E_s)\mathbf{B}dx - \int_0^L \mathbf{N}^T(2\tau_0 D)\mathbf{B}dx \tag{4.64}$$

and the consistent element node force vector is,

$$f^e = \int_0^L \mathbf{N}^T q_c dx \tag{4.65}$$

All the information has been obtained for the Euler-Bernoulli beam finite element with surface effects considered. The exact formulation of the stiffness matrix can be obtained by integrating Equation (4.64) as,

$$\begin{aligned} K^e = EI & \begin{bmatrix} \frac{12}{l^3} & \frac{6}{l^2} & -\frac{12}{l^3} & \frac{6}{l^2} \\ \frac{6}{l^2} & \frac{4}{l} & -\frac{6}{l^2} & \frac{2}{l} \\ -\frac{12}{l^3} & -\frac{6}{l^2} & \frac{12}{l^3} & -\frac{6}{l^2} \\ \frac{6}{l^2} & \frac{2}{l} & -\frac{6}{l^2} & \frac{4}{l} \end{bmatrix} \\ +\frac{\pi}{8}D^3E_s & \begin{bmatrix} \frac{12}{l^3} & \frac{6}{l^2} & -\frac{12}{l^3} & \frac{6}{l^2} \\ \frac{6}{l^2} & \frac{4}{l} & -\frac{6}{l^2} & \frac{2}{l} \\ -\frac{12}{l^3} & -\frac{6}{l^2} & \frac{12}{l^3} & -\frac{6}{l^2} \\ \frac{6}{l^2} & \frac{2}{l} & -\frac{6}{l^2} & \frac{4}{l} \end{bmatrix} \\ -2\tau_0 D & \begin{bmatrix} \frac{6}{5l} & -\frac{11}{10} & \frac{6}{5l} & -\frac{1}{10} \\ -\frac{1}{10} & -\frac{2l}{15} & \frac{1}{10} & \frac{l}{30} \\ \frac{6}{5l} & \frac{1}{10} & -\frac{6}{5l} & \frac{11}{10} \\ -\frac{1}{10} & \frac{l}{30} & \frac{1}{10} & -\frac{2l}{15} \end{bmatrix} \end{aligned} \tag{4.66}$$

Form Equation (4.66) we can see that the element stiffness matrix of the Euler-Bernoulli beam with surface effects considered consist of three parts, the conventional beam element stiffness matrix, the effects of surface stiffness, these two parts are symmetric and a nonsymmetric part which comes from the effects of initial surface tension.

4.3.2 Validation of the finite element stiffness matrix

In this section, the correctness of the obtained element stiffness matrix is tested by numerically simulate beams with three boundary conditions subjected to concentrated force acting at beam center or free end. The deflection obtain from proposed element is compared with the analytical prediction reported by (He and Lilley, 2008). They reported the analytical solution for the deflection of beam with cantilever, simple supported and clamped boundary conditions for surface tension $\tau_0 = 0$ as,

$$v = \begin{cases} \dfrac{F(3L-x)x^2}{6(EI+\frac{\pi}{8}E_sD^3)}, x \in [0,L](\text{cantilever}) \\ \\ \dfrac{F(3L^2-4x^2)x}{48(EI+\frac{\pi}{8}E_sD^3)}, x \in [0,L/2](\text{simple}) \ , \tau_0 = 0 \\ \\ \dfrac{F(3L-4x)x^2}{48(EI+\frac{\pi}{8}E_sD^3)}, x \in [0,L/2](\text{clamped}) \end{cases} \tag{4.67}$$

and for surface tension $\tau_0 \neq 0$ as,

$$v = \begin{cases} \dfrac{F\cosh\sqrt{\eta}}{2\tau_0 D}\left[x - \dfrac{L}{\sqrt{\eta}}\tanh\sqrt{\eta} - \dfrac{L}{\sqrt{\eta}}\dfrac{\sinh(\sqrt{\eta}x/L - \sqrt{\eta})}{\cosh\sqrt{\eta}}\right], \\ \qquad\qquad x \in [0, L](\text{cantilever}) \\ \dfrac{F}{4\tau_0 D}\left[x - \dfrac{L}{\sqrt{\eta}}\dfrac{\sinh\sqrt{\eta}x/L}{\sqrt{\eta}\cosh(\sqrt{\eta}/2)}\right], \\ \qquad\qquad x \in [0, L/2](\text{simple}) \\ \dfrac{F}{4\tau_0 D}\left[x - \dfrac{L}{\sqrt{\eta}}\tanh(\sqrt{\eta}/4) - \dfrac{L}{\sqrt{\eta}}\dfrac{\sinh(\sqrt{\eta}x/L - \sqrt{\eta}/4)}{\cosh(\sqrt{\eta}/4)}\right], \\ \qquad\qquad x \in [0, L/2](\text{clamped}) \end{cases} , \tau_0 \neq 0 \quad (4.68)$$

where $\eta = 2\tau_0 DL^2/(EI + \pi E_s D^3/8)$ is a dimensionless surface effects factor which reflects the influences of the surface effects on the overall elastic behaviour of the beam. It's worthwhile to mention that η could be either positive or negative, due to both positive and negative surface tension τ_0 is reported from atomistic simulations (Shenoy, 2005).

Similar cantilever beam: fixed at the left end and loaded at the right free end with a concentrated force P = 0.05 nN; simple supported beam: simple supported at both end with a concentrated force P = 0.05 nN acting at beam center, and clamped beam: fixed at both end with a concentrated force P = 0.05 nN acting at beam center (He and Lilley, 2008) is employed to verify this finite element method. The beam has a length of L = 1,000 nm, a diameter of D = 50 nm and a Young's modulus of E = 76 GPa. To investigate the roles of surface stiffness E_s and initial surface tension τ_0, three cases (1) τ_0 = 0, E_s = 0; (2) τ_0 = 1.22 N/m and E_s = 5.8 N/m and (3) τ_0 = -1.22 N/m and E_s = 5.8 N/m are simulated and their deflection is represented by the red circular, green triangle and blue square markers, respectively, in Figures 4.6-4.8 Encouragingly, all of them are exactly located on the solid curves which are obtained from the theoretical predictions from Equations (4.67) and (4.68) (He and Lilley, 2008). There is no size effects in Case 1 because of τ_0 = 0 and E_s = 0. Therefore, it can be used as the referent example

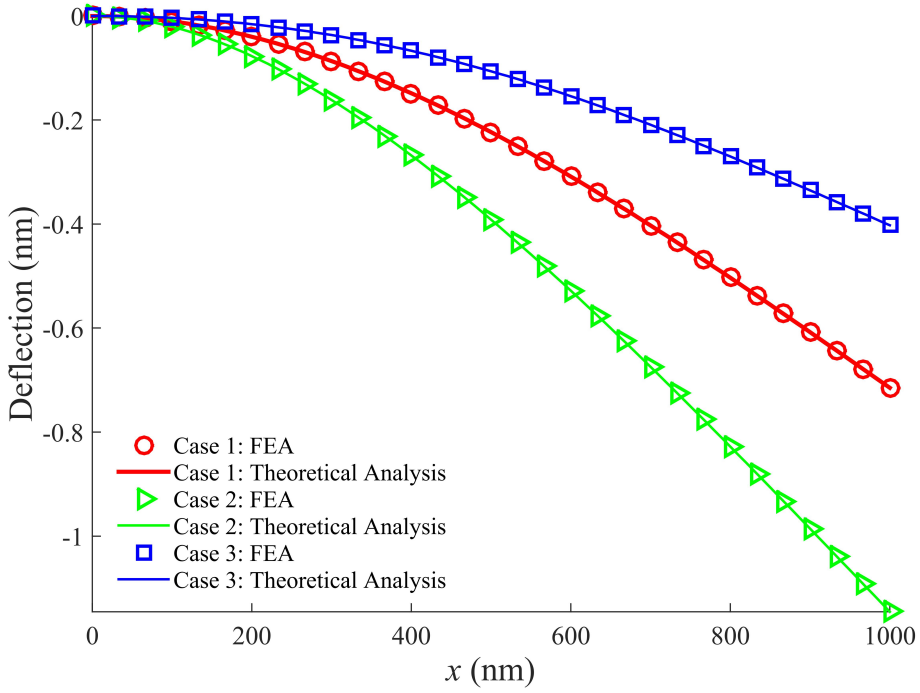

Figure 4.6: The comparison of the deflection for a cantilever beam subjected to concentrated force at free end obtained from the proposed element with theoretical prediction from (He and Lilley, 2008)

to illustrate the significance of size effects. For example, in Figure 4.6 the deflection in Case 2 (green markers) is larger than Case 1 (red markers). Thus the beam is softened by the size effects. While the beam is strengthened in Case 3 due to the smaller deflection (blue markers). For the simple supported and clamped boundary conditions, however with the same combination of surface stiffness and surface tension, an opposite trend of softening and strengthening trend occur. Specifically speaking, in contrast to the softening (strengthening) effects for a positive (negative) value of surface tension in Case 2 (Case 3), as shown in Figure 4.6, a strengthening (softening) effects occurred for both simple supported and clamped boundary condition as shown in Figures 4.7 and 4.8, the deflection in Case 2 (green markers) is smaller than Case 1 (red markers). Thus those beams are strengthened by the size effects. And those beams are softened in Case 3 due to the larger deflection (blue markers).

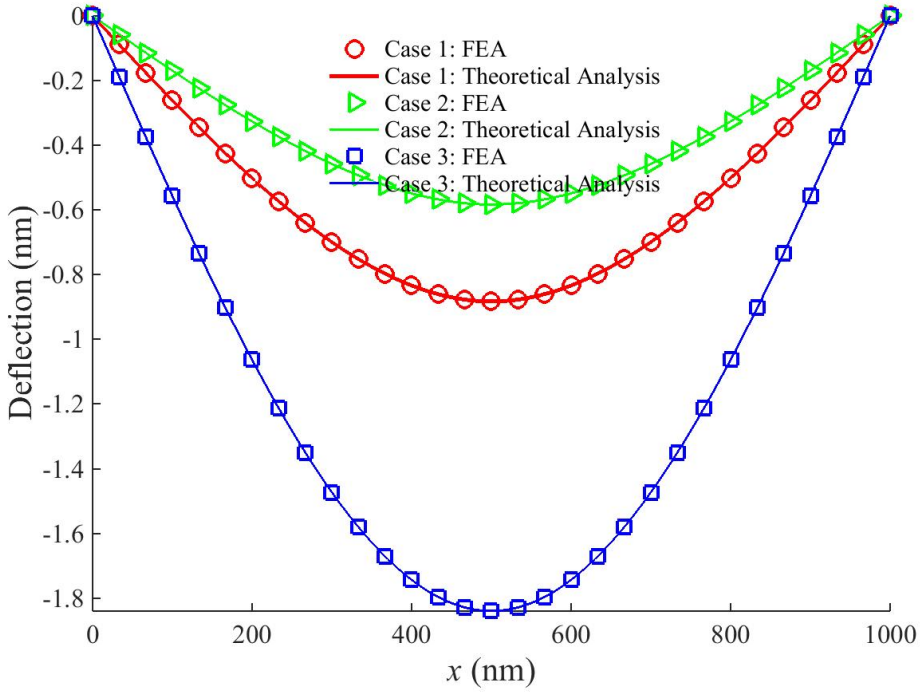

Figure 4.7: The comparison of the deflection for a simple supported beam subjected to concentrated force at beam center obtained from the proposed element with theoretical prediction from (He and Lilley, 2008)

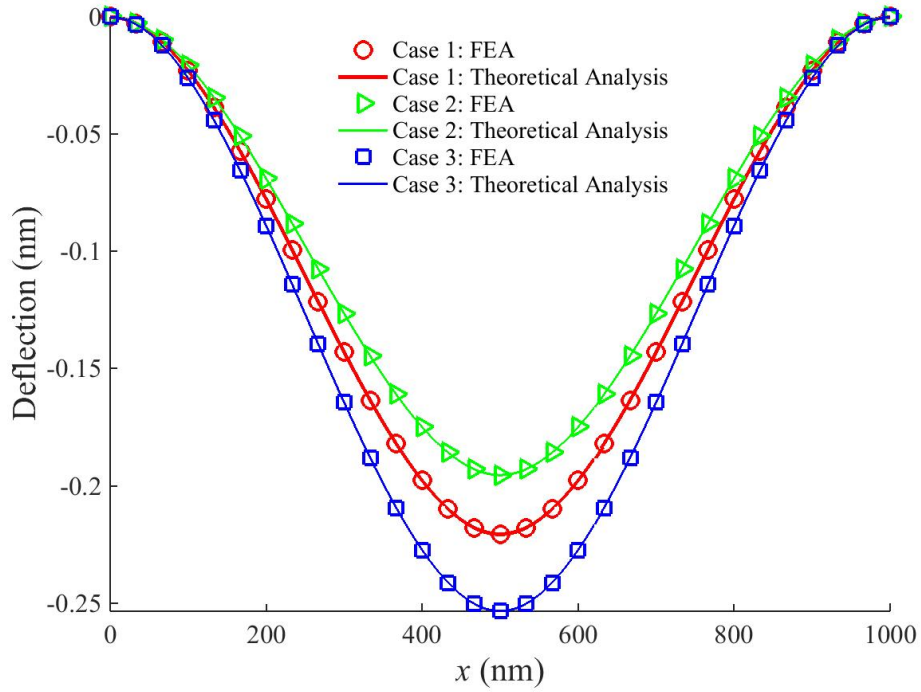

Figure 4.8: The comparison of the deflection for a fixed-fixed beam subjected to concentrated force at beam center obtained from the proposed element with theoretical prediction from (He and Lilley, 2008)

4.4 Application of the new elements with size effects

A single beam with boundary conditions in the last section subjected to simple load is easy to simulate and even can be solved analytically. The goal of proposing the new element with size effects integrated into the element stiffness matrix is to extend the scope of the theoretical framework to a complex scenario. In this section, the capability of the proposed element will be tested to compare with the existing experimental data, theoretical predictions and nano porous gold with complex topology.

4.4.1 Simulation of the bending test on nanowires

The first example is to simulate the bending experiment (Jing et al., 2006) on nano wires for a clamped beam on which a concentrated load is applied at its middle point, as shown in Figure 3.3. According to Euler-Bernoulli beam theory, the deflection at beam center is expressed as,

$$w_c = \frac{FL^3}{192EI} \tag{4.69}$$

where F is the concentrated force acting at beam center, L is the length of the beam, E is the Young's modulus of the constitutive material of the beam, and I is the second moment of inertia of the cross-section of the beam.

The effective Young's modulus E^* can be obtained by substituting the deflection value at beam center obtained from the finite element analysis back to Equation (4.69) and solve the Young's modulus (He and Lilley, 2008; Lu et al., 2014), which is given as,

$$E* = \frac{FL^3}{192w_cI} \tag{4.70}$$

here w_c is the deflection at beam center obtained from the finite element analysis.

Figure 4.9 demonstrates the effective Young's modulus obtained from the proposed new elements. According to the experiment reported in (Jing et al., 2006), the nanowires are suspended over the etched holes in the silicon wafer to form a beam with both ends fixed. In the three-point bending test (Jing et al., 2006), the length of the beam is fixed to L = 1,000 nm, but the diameter D varies from 20 nm to 140 nm. According to (Gere and Timoshenko, 1990), defining the specific ratio r of a beam as the ratio of diameter D over length L, it is required

that $r < 1/16$ for Euler-Bernoulli beam theory to be valid and $r > 1/16$ for Timoshenko beam theory to be applied. Therefore, the threshold diameter can be determined from $L/16 \approx 60$ nm and the valid diameter regions of Euler-Bernoulli beam theory, and Timoshenko beam theory are $D = 0 \sim 60$ nm and $D = 60 \sim 150$ nm, respectively (Gere and Timoshenko, 1990). The material of this beam is silver with $E = 76$ GPa (Jing et al., 2006), its initial surface stress $E_s = 1.22$ N/m and the surface stress $\tau_0 = 0.89$ N/m are obtained from the literature (Shenoy, 2005). As shown in Figure 4.9, there is a sudden increase of effective Young's modulus (solid blue line with circular marker) when the beam diameter is smaller than $D < 40$ nm. The numerical results match the experimental data (red triangles) within a small margin of error. Because the shear deformation is considered in Timoshenko beam theory which results in an additional energy term (the third term on the left side of Equation (4.43)) in the internal energy and unchanged external energy, the effective Young's modulus becomes smaller than the one obtained from Euler-Bernoulli beam theory. Such a drop is clearly observed in Figure 4.9 at $D = 60$ nm. The predictions beyond the validation ranges for both beam theories are plotted as black dash line as well, which illustrate that both theories become invalid in these ranges.

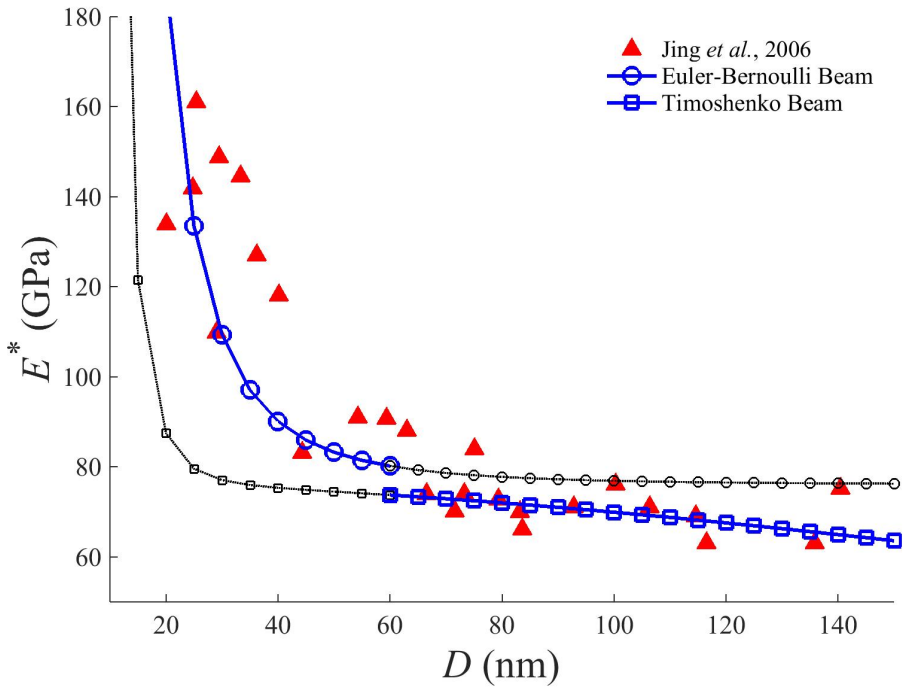

Figure 4.9: The comparison of experimental data (Jing et al., 2006) with the computational results for the effective Young's modulus of a silver nanowire.

4.4.2 Simulation of the orthogonal unit cell model

A cubic unit cell with orthogonal strut is proposed by (Feng et al., 2009) as an approximate representation of nanoporous gold as shown in the inset in Figure 4.10.

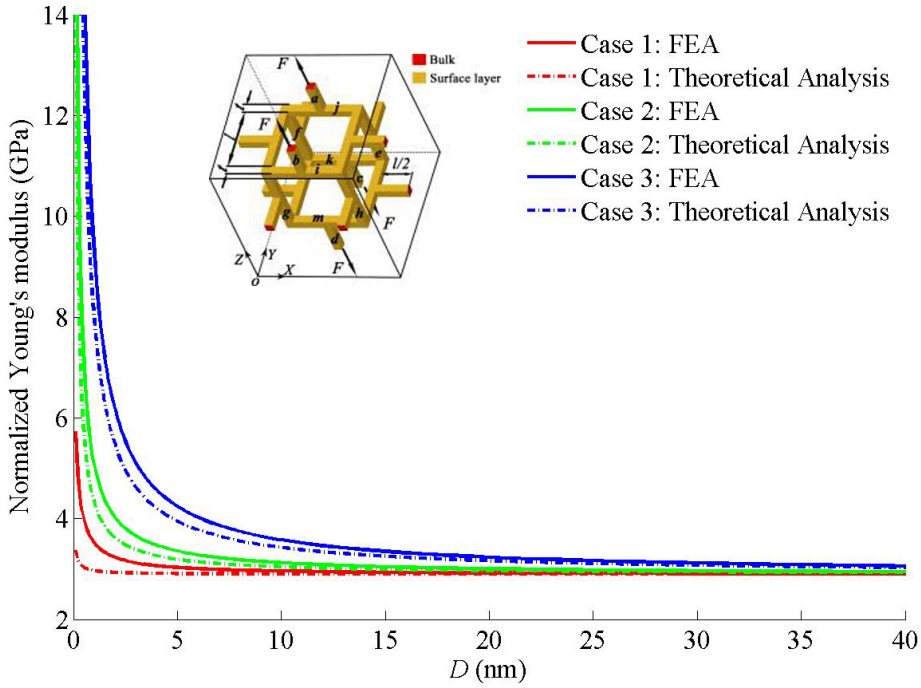

Figure 4.10: FIG. 5. The comparison of the effective Young's modulus with the prediction in (Feng et al., 2009).

For the simplicity in theoretical analysis, the constituting ligaments are assumed to be perpendicular to each other and for those ligaments that are parallel to the loading direction will only have axis compression and for those ligaments that are perpendicular to the loading direction will only have bending deformation.

Feng *et al.* (Feng et al., 2009) indicated that the effective Young's modulus tends to abruptly increase when the beam diameter reaches to 5 nm (shown as the red, green and blue dot curves for Case 1 $E_s = 0.00$ N/m and $\tau_0 = 1.64$ N/m; Case 2 $E_s = 6.60$ N/m and $\tau_0 = 1.64$ N/m and Case 3 $E_s = 25.00$ N/m and $\tau_0 = 1.64$ N/m). For this 3D beam system, the effective properties (corresponded solid curves in Figure 4.10) calculated from finite element analysis exhibit similar trends to the dotted curves. Since only the flexure deformation and the axial deformation are considered for horizontal struts and vertical struts respectively in (Feng et al., 2009), the system is artificially weakened, and thus it is likely to reduce the stiffness. The

finite element analysis considers the system in a whole and therefore it could reveal the real deformation. And this is exactly the reason for the disparity between the results obtained from the new element and the result Feng *et al.* reported.

4.4.3 Simulation of an open-cell nanoporous gold

The most important advance of this numerical approach based on finite element analysis is its wide applicability to models with complex topology and boundary conditions that can not be solved analytically. It can be used for arbitrary structures in a complex shape, subjected to complicated boundary conditions, and undergoing diverse loadings as well as their combinations. Previous theoretical analyses are mainly based on simplified structures. To investigate the size effects for a real nanoporous gold as showed in Figure 4.11, we devise a cubic open cell foam composed of a number of randomly-connected beams (Figure 4.12) using the technique of Voronoi tessellations and Q-hull (Barber et al., 1996; Okabe et al., 2009). In this model the diameter D of the constituting beams ranges from 3 nm to 40 nm and its ratio to the length of the longest beam is fixed as $D = 0.25L_{max}$, where L_{max} denotes the length of the longest beam in the model. The size of this open-cell form is $20D \times 20D \times 20D$, and it has the similar volume fraction (around 0.3 in (Rösner et al., 2007)) to the common nanoporous gold. Unlike previous examples based on the Euler-Bernoulli beam theory, this example is based on Timoshenko beam theory because of the relatively small ratio of the beam length to its diameter. Thereby, the element stiffness matrix for this kind of beam structure is determined from Equation (4.43).

For the ideal single-crystalline gold on the (001) crystal surface, the surface stress is $\tau_0 = 1.40$ N/m in accordance with the atomic simulation conducted by Shenoy *et al.* (Shenoy, 2005). Given the small ligament size and post-fabrication processes may lead to a dramatic increase in residual stress, it is thereafter changed to $\tau_0 = 80.0$ N/m (Lee et al., 2007a). The Young's modulus and surface stiffness for the constituting material are $E = 79$ GPa and $E_s = 3.63$ N/m, respectively. The effective Young's modulus for this nanoporous material is plotted in Figure 4.13 (the solid blue line), which shows it has the same trend as experiment data (green circular marker with error bar) (Lee et al., 2007a; Mathur and Erlebacher, 2007; Volkert et al., 2006). When D is in the range of $15 \sim 40$ nm, the effective Young's modulus is located in the $6 \sim 12$ GPa range, which agrees very well with data obtained by nanoindendation

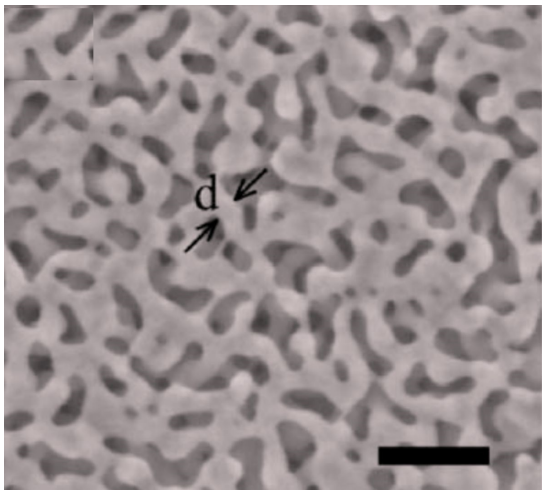

Figure 4.11: The SEM image of a representative nanoporous gold with the ligament size $D = 20$ nm(Mathur and Erlebacher, 2007).

and compression tests (Lee et al., 2007a; Volkert et al., 2006). When $D < 15$ nm, the modulus increases rapidly and surges to 40 GPa at $D = 3$ nm. Since the model generated by random spatial tessellations and Q-hull cannot fully represent the real nanoporous gold, there are disparities between the computational results and experimental data. Such errors are acceptable as they are within a small range. Inaccurate surface parameters might result in the errors as well, but further investigations are needed in this field.

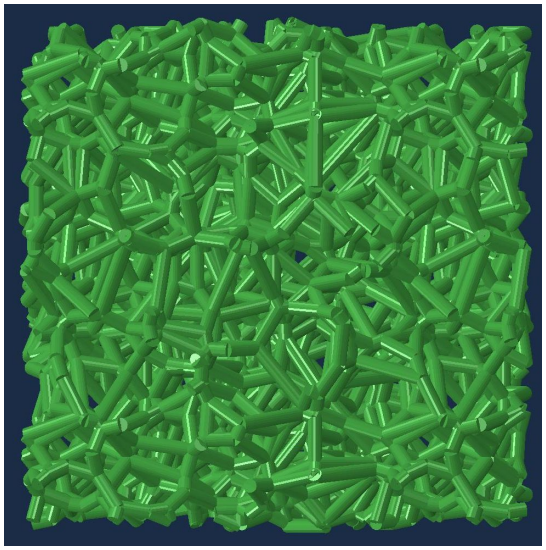

Figure 4.12: A perspective view of a random open-cell foam generated by Voronoi tessellations.

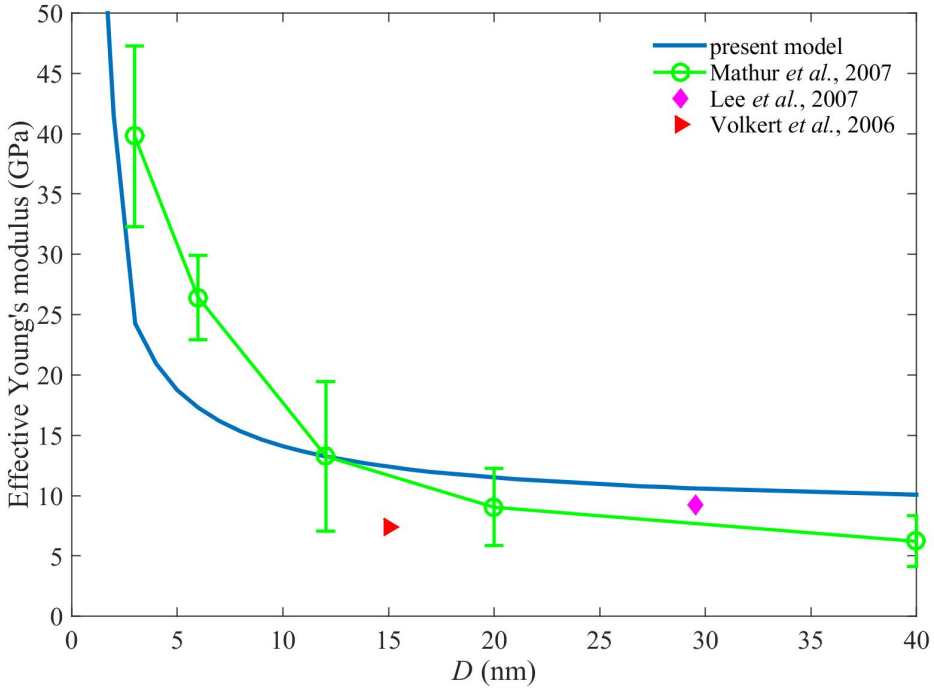

Figure 4.13: The comparison of the effective Young's modulus between computational results with experiment data (Lee et al., 2007a; Mathur and Erlebacher, 2007; Volkert et al., 2006).

4.5 Summary

The size effects that reveal the dramatic changes of mechanical behaviour at nanoscales have traditionally been analyzed for regular beam systems. Here, the method of using finite element analysis is explored with the intention of evaluating the size effects for complex nanostructures. Different from the iterative finite element method with a solid element, which may suffer from convergence issue, a finite element method based on beam theories is proposed in this chapter. The surface elasticity theory and generalized Young-Laplace equation are integrated into beam elements to account for the size effects in classical Euler-Bernoulli and Timoshenko beam theories. Computational results match well with the theoretical predictions on the size effects for a cantilever beam and for a cubic unit cell containing 24 horizontal/vertical ligaments. For a simply-supported nanowire, it is found the results are very close to the experimental data. With the assumption that the nanoporous gold is composed of many randomly-connected beams, for the first time, the size effects of such a complex structure is numerically determined.

In summary, we develop a finite element approach for bending based element. And implemented the finite element method within the framework of Euler-Bernoulli and Timoshenko beam theories to retrieve the effective Young's modulus for arbitrary nanostructures. Surface effects are taken into consideration by integrating the surface elasticity theory and generalized Young-Laplace equation into the element stiffness matrix. Numerical simulation results are in good agreement with not only the analytical solution but also the experimental data. More importantly, the new elements enable the investigation of size effects for complex nanomaterials such as nanoporous gold with open-cell foams. The present approach paves the way to exploiting and optimizing the exceptional performance of material at nano scale by using techniques such as structural topology optimisation.

CHAPTER 5

TOPOLOGY optimisation WITH SIZE EFFECTS AT NANOSCALE

5.1 Introduction

Vast attention has been drawn to the mechanical response of nanoporous materials such as nanoporous Au (Mathur and Erlebacher, 2007; Volkert et al., 2006), because of their high potential in applications which benefit from their characteristic large specific surface area. Another important property associated with nano porous is the emergence of the so-called size effects (Dou et al., 2010; Hodge et al., 2007; Weissmuller et al., 2009). In this case, the mechanical properties such as stiffness and strength exhibits a strong dependence on the characteristic sizes of the microstructure (Chen et al., 2006a; Cuenot et al., 2004; Lee et al., 2007b; Lukic et al., 2005), in particular, for length scale less than 100 nm, which let nanoporous holds great promise for applications involving lightweight and ultra-strong materials.

In classical porous theory, however, the mechanical properties are assumed to be scale independent (Gibson and Ashby, 1982, 1999) and it becomes inaccurate in dealing with the same problems for nanoporous materials. Recently, much effort has been dedicated to understanding the size-dependence properties of materials at nano scale. In particular, a framework of surface elasticity and generalized Young-Laplace equation has been successfully adapted to the unusual mechanical behaviour and provided a reasonable explanation for some relevant experimental results (Feng et al., 2009; He and Lilley, 2008; Lu et al., 2014, 2015).

Within the mechanical context, the effective properties, such as bulk modulus and shear modulus, of nano porous material is crucial in many applications (Schaedler et al., 2011). They are determined both by their micro structure, namely the spatial configuration of bulk materials and voids, and the properties of the constituent solid such as stiffness, strength, etc. (Gibson

and Ashby, 1999).

5.1.1 Homogenization theory

Homogenization theory is adapted to estimate the effective properties of a heterogeneous composite by assuming that the composite could be treated as an equivalent material model with certain types of periodicity.

It developed from the studies on partial differential equations with rapid varying coefficients in the 70's (Bensoussan et al., 1978; Hassani and Hinton, 1998a,b,c). In homogenization theory, the heterogeneous composites are taken as a cluster of the repetition of 'microscopic' cells known as the periodic base cell (PBC).

It assumes the physical properties vary on multi-scales because of the existence of periodic base cells. And can be defined by periodic functions like,

$$\mathbf{\Gamma}(x_1 + n_1 Y_1, x_2 + n_2 Y_2, x_2 + n_l Y_2) = \mathbf{\Gamma}(x_1, x_2, x_3) \tag{5.1}$$

where $\mathbf{x} = (x_1, x_2, x_3)$ is the position vector, $\mathbf{Y} = (Y_1, Y_2, Y_3)$ is a constant vector which determine the periodicity of function $\mathbf{\Gamma}$. And n_1, n_2, n_3 are arbitrary integer numbers.

The period $\mathbf{Y}$ is assumed to be in 'microscopic' compared with the dimension of the problem studied, which means $\mathbf{Y}$ is much smaller than the overall characteristic dimensions of the research domain. Therefore two scales of dependencies for all quantities exist: one on the *macroscopic* or *global* level $\mathbf{x}$ with slow variations, and the other on the *microscopic* or *local* level $\mathbf{Y}$ with rapid oscillations.

By using the asymptotic expansion, the functions of the physical properties of the composite material can be expanded as:

$$\phi^{\varepsilon}(\mathbf{x}) = \phi^0(\mathbf{x}) + \varepsilon\phi^1(\mathbf{x}, \mathbf{y}) + \varepsilon^2\phi^2(\mathbf{x}, \mathbf{y}) + \dots \tag{5.2}$$

where ε is a small parameter representing the ratio of the real length of a unit cell in the microscopic coordinates to the real length of a unit vector in the macroscopic coordinates, and $\varepsilon = \mathbf{x}/\mathbf{Y}$. ϕ^0 is taken as the average value of the function, and ϕ^1 and ϕ^2 are the local oscillations which take equal values on the opposite sides of the periodic base cells. In elasticity

problems, the first term on the expansion ϕ^0 only depends on the macroscopic scale $\mathbf{x}$ (Hassani and Hinton, 1998c).

The effective or homogenized elastic tensor of a composite material can be obtained by using the double scale asymptotic expansion and imposing the periodicity on the microstructure boundary conditions. The effective or homogenized elasticity tensor of composite materials can be calculated as (Bendsøe and Kikuchi, 1988):

$$E^H_{ijkl}(\mathbf{x}) = \frac{1}{|Y|}\int_Y (E_{ijkl} - E_{ijpq}\frac{\partial \chi^{kl}_p}{\partial y_p})dy \tag{5.3}$$

with χ is the solution of:

$$\int_Y E_{ijpq}\frac{\partial \chi^{kl}_p}{\partial y_q}\frac{\partial v_i}{\partial y_j}dy = \int_\Omega E_{ijkl}\frac{\partial v_i}{\partial y_j}dy, \forall \mathbf{v} \in \mathbf{U}_Y \tag{5.4}$$

where Y denotes the periodic unit cell in $\mathbf{R}^3$, where E^H_{ijkl} is homogenized elasticity tensor, E_{ijkl} is the constitutive matrix at a given point in the domain, v is an arbitrary admissible displacement that can be expanded as

$$v^\varepsilon(x) = v_0(x) + \varepsilon v_1(x, y), \quad y = x/\varepsilon \tag{5.5}$$

$\mathbf{U}_Y$ is the admissible space defined in the cell Y:

$$\mathbf{U}_Y = \left\{\mathbf{v} = v_i e_{Yi} : v_i \in H^1(Y)/R, v_i \quad \text{takes equal values on opposite faces of } Y\right\}$$

5.1.2 Material property bounds

In conventional continuum mechanics, the effective properties of porous materials are bounded in a theoretical range.

Those bounds define the function over each of the individual properties of the constituent material in terms of their volume fractions, which provides a theoretical estimation over the admissible range of the composite effective properties (Zhou and Li, 2008a,b). And have been using as an important theoretical tool for the research and design of new composites over the last decades. They are often adapted to verify the optimality of composite materials (Challis

et al., 2008).

The most well-known bound is the Hashin-Shtrikman bounds (Hashin and Shtrikman, 1963), which is derived by Hashin and Strickman from a variational approach. Based on classical continuum theory, this bound provides the exact range of properties of an isotropic two-phase material could achieve with given material composition and only the volume fractions available (Hashin and Shtrikman, 1963). For quasi-homogeneous quasi-isotropic multi-phase material, if with well-ordered constituent phases $(K_{(1)} - K_{(1)})(G_{(1)} - G_{(1)}) \geq 0$, where K and G stands for the bulk and shear modulus respectively, and subscripts indicate the materials number, this bound is applicable as well.

For a composite material with a volume fraction V_f of solid material in the solid domain, the maximum value of bulk or shear modulus satisfy the Hashin-Shtrikman bounds for two-phase materials (Hashin and Shtrikman, 1963). The corresponding dimensionless upper bounds of stiffness are given as below.

$$\begin{aligned} \kappa_{upper} &= \frac{V_f G_0}{\big(1-V_f\big)\kappa_0+G_0} \\ G_{upper} &= \frac{V_f \kappa_0}{\big(1-V_f\big)(\kappa_0+2G_0)+\kappa_0} \end{aligned} \tag{5.6}$$

where κ_{upper} and G_{upper} are the upper bound for bulk and shear modulus respectively, κ_0 and G_0 are the bulk and shear modulus of the constituent material of the composite. Apart from the constituent material properties and volume fraction, the effective properties of the composites is strongly microstructural geometries dependent (Gibiansky, 1993).

With size effects included it is rational to expect nanomaterials with the new design of microstructure which possess optimum effective properties that could reach even beyond the conventional material bound like, Hashin-Shtrikman Bound. Creating a new microstructure of a nano porous material which produces properties beyond those of the conventional prediction is of great significance (Schaedler et al., 2011). This objective could be accomplished by casting a topology optimisation problem for the nanoporous microstructure.

5.1.3 The Bidirectional Evolutionary Structural optimisation method

Topology optimisation is a powerful method to obtain the optimal configuration of structures from the design objectives and constraints mathematically, and is usually used to search the

optimum or most economical distribution of material in a given design domain. Well-known topology optimisation methods include Solid Isotropic Material with Penalization (SIMP) method (Bendsøe, 1989; Sigmund, 2001), level-set method (Allaire et al., 2002), Evolutionary Structural optimisation (ESO) (Xie and Steven, 1993, 1997) and its later version Bidirectional Evolutionary Structural optimisation (BESO) (Huang and Xie, 2007, 2009, 2010; Querin et al., 1998).

Xie and Steven (Xie and Steven, 1993, 1997) introduced the topology optimisation algorithm called Evolutionary Structural optimisation (ESO) in 1993. It is based on the intuitive idea of gradually removing low-efficient materials from the structure so that the topology of the structure evolve gradually toward the optimum.

The Bi-directional Evolutionary Structural optimisation (BESO) proposed by Huang and Xie (Huang and Xie, 2011) is the improved version of (ESO). It aims to simultaneously add or remove elements from the structure. In (ESO), the low-efficient elements are completely removed from the structure, as a consequence, information about the effects of these elements vanish in later stages of optimisation. The essence of BESO is to eliminate inefficiency materials meanwhile add materials to the most efficient regions. Thus, the topology of a structure will evolve to an optimum. Though the basic idea is simple, BESO has been proven to be efficient and robust for various topology optimisation problems (Huang and Xie, 2011; Huang et al., 2014; Zuo et al., 2013).

Recently, BESO has been further extended to design the microstructures of materials with extreme mechanical properties(Huang et al., 2013, 2015), thermal properties and electromagnetic properties (Huang et al., 2012).

These methods have been successfully extended to the design of cellular materials and composites, optical devices (Aage et al., 2010; Jensen and Sigmund, 2011; Wang et al., 2011), and band gap structures (Li et al., 2016; Meng et al., 2015; Sigmund and Hougaard, 2008). Existing researches has demonstrated the great potential of topology optimisation to find novel results with optimum even exotic properties which could be anti-intuitive in conventional sensitivities.

In order to create a novel nanoporous material with extreme properties, the BESO method is adopted.

5.2 Spatial frame element with surface effects

A spatial frame element build on the aforementioned surface elasticity and generalized Young-Laplace equation is used to account for the size effects of porous material at the nanoscale. By including this size-dependent part of pressure into the equilibrium equation of the system, a new weak form of the equilibrium equation of beam in finite element analysis could be built. In fact, this takes into account the curvature-dependent pressure existing on the surface of materials which is neglected at the macro scale. With one additional term that changes the effective bending rigidity and another which comes from the additional pressure, a new finite element is built with size effects include,

$$\int_0^L v'' EI v'' dx + \int_0^L v'' \frac{\pi D^3}{8} E_s v'' dx - \int_0^L v(2\tau_0 D) v'' dx = \int_0^L q_c v dx \tag{5.7}$$

This element has been tested to be valid and effective in last chapter and will be used to simulate nanoporous material to conduct topology optimisation in this chapter.

5.3 optimisation formulations

This chapter will focus on the design of a nanoporous material with extreme bulk or shear modulus under a given volume constraint using BESO. To explore the potential of exceptional mechanical property of nano porous material, this work is the first attempt to design a nanoporous material with extreme bulk or shear modulus under a given volume constraint using topology optimisation. The topology of the microstructure and the effective properties of a nanoporous material are totally represented by a periodic base cell (PBC) which is discretized as spatial frame elements with size effects on a grand structure, as shown in Figure 5.1, (Hagishita and Ohsaki, 2009). The ground structure derived from the ground structure method (Dorn, 1964), is a truss network generated for a set of nodes. Theoretically, all the nodes are interconnected by a member in the network and could be used approximates an optimal Michell structure (Hemp, 1973; Ohsaki, 2016) composed of an infinite number of members with a finite number of truss members.

The stiffness of an elastic material can be described by the bulk modulus K or shear modulus G. They are the most essential properties of cellular materials, and highly depend on

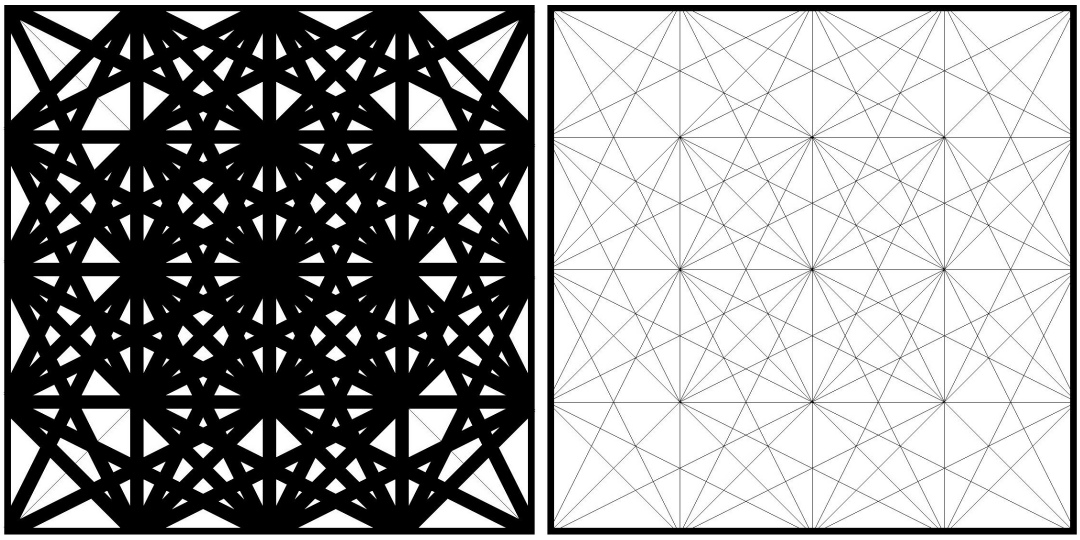

Figure 5.1: The schematic of a 4×4 grid ground structure with different initial volume fraction.

the microstructure of their base cells (Gibson and Ashby, 1999). To obtain the stiffest material, the effective bulk modulus or shear modulus of cellular materials can be chosen as the objective function. The topology optimisation problem is to find the appropriate distribution of the solid phase within the PBC, here the diameter of the members in the ground structure, subject to a prescribed volume fraction and can be defined as:

Maximize: $f(\mathbf{x}) = K$ or G

Subject to:

$$\begin{aligned} & V^* - \sum_{e=1}^{N} V_e = 0 \\ & x_e \in [x_{e\_\min}, 1] \end{aligned} \tag{5.8}$$

where V_e and V^* are the volumes of an individual member and the prescribed target volume fraction. The total number of the members in the ground structure of the PBC is denoted as N. And the design variable x_e is the normalized diameter, from which the diameter of a member D_e is expressed as:

$$D_e = D_0 x_e \tag{5.9}$$

where D_0 is a upper limit on the diameter of the members. The volume of the individual

member is calculated from:

$$\begin{aligned} V_e &= A_e l_e \\ &= \frac{\pi}{4} D_e^2 l_e \\ &= \frac{\pi}{4} (D_0 x_e)^2 l_e \end{aligned} \tag{5.10}$$

where A_e and le are the cross-section area and length of the member e respectively.

The bulk modulus K^H and shear modulus G^H of the materials can be expressed in terms of the components of the effective elasticity tensor E^H_{ijkl} in 2D cases as:

$$\begin{aligned} \kappa^H &= \tfrac{1}{4} \left(E^H_{1111} + E^H_{1122} + E^H_{2211} + E^H_{2222} \right) \\ G^H &= E^H_{1212} \end{aligned} \tag{5.11}$$

and in 3D cases as:

$$\begin{aligned} \kappa^H &= \tfrac{1}{9} \left(E^H_{1111} + E^H_{1122} + E^H_{1133} + E^H_{2211} + E^H_{2222} + E^H_{2233} + E^H_{3311} + E^H_{3322} + E^H_{3333} \right) \\ G^H &= \tfrac{1}{3} (E^H_{2323} + E^H_{3131} + E^H_{1212}) \end{aligned} \tag{5.12}$$

with the index map for 2D and 3D listed below,

$$\begin{array}{cccccccc} j = & 11 & 22 & 12, 21 & & & & \\ & \Downarrow & \Downarrow & \Downarrow & \Downarrow & & & \\ \alpha = & 1 & 2 & 3 & & & & \\ j = & 11 & 22 & 33 & 23, 32 & 13, 31 & 12, 21 & \\ & \Downarrow & \Downarrow & \Downarrow & \Downarrow & \Downarrow & \Downarrow & \Downarrow \\ \alpha = & 1 & 2 & 3 & 4 & 5 & 6 & \end{array}$$

The fourth-order elasticity tensor C_{ijkl} can be simplified as a matrix $C_{\alpha\beta}$. And the homogenized bulk and shear modulus can be expressed in 2D cases as:

$$\begin{aligned} \kappa^H &= \tfrac{1}{4} \left(E^H_{11} + E^H_{12} + E^H_{21} + E^H_{22} \right) \\ G^H &= E^H_{33} \end{aligned} \tag{5.13}$$

and in 3D cases as:

$$\begin{aligned} \kappa^H &= \tfrac{1}{9}\left(E^H_{11}+E^H_{12}+E^H_{13}+E^H_{21}+E^H_{22}+E^H_{23}+E^H_{31}+E^H_{32}+E^H_{33}\right) \\ G^H &= \tfrac{1}{3}(E^H_{44}+E^H_{55}+E^H_{66}) \end{aligned} \tag{5.14}$$

In this chapter, the effective elasticity tenor is calculated from homogenization theory (Bendsøe and Kikuchi, 1988; Sigmund, 1995) in terms of the material distribution in the PBC as:

$$E^H_{ij} = \frac{1}{|Y|}\int_\Omega \left(\left\{\varepsilon^i_0\right\}-\left\{\varepsilon^i\right\}\right)^T [E]\left(\left\{\varepsilon^j_0\right\}-\left\{\varepsilon^j\right\}\right) dy \tag{5.15}$$

where E^H_{ij} denotes the homogenized elasticity tensor, E is the elasticity tensor at a material point, $|Y|$ is the area of the 2D PBC, ε^i_0 are three linear independent test strain fields as $\varepsilon^1_0 = \{1,0,0\}$, $\varepsilon^2_0 = \{0,1,0\}$,$\varepsilon^3_0 = \{0,0,1\}$, and ε^i are the resulting strain fields from test, which are the solution to the PBC with periodic boundary condition subjected to the test strain fields ε^i_0.

In the topology optimisation, it is assumed that the size of the ground structure PBC is very small compared with the overall material size. The periodic boundary condition is applied on PBC. According to the asymptotic expansion in Equation (5.2), the displacement of the node i in the PBC under the strain, $\bar{\varepsilon} = \{\bar{\varepsilon}_x, \bar{\varepsilon}_y, \bar{\gamma}_{xy}\}$ in 2D cases is the sum of the macroscopic displacement and a periodic displacement Michel et al. (1999). As shown in Figure 5.2, the displacement of node i in x-axis can be expressed as,

$$u^x_i = \bar{\varepsilon}_x x_i + \tilde{u}^x_i \tag{5.16}$$

where x_i is the x-coordinate of the node, $\tilde{u}^x_i$ is an unknown term.

Based on the definition of periodic boundary condition, the displacements along x-axis for a pair of nodes on the opposite boundaries, as shown in Figure 5.2 for 2D case, should satisfy the listed equations,

$$\begin{aligned} u^x_{i-} &= \bar{\varepsilon}_x x_{i-} + \tilde{u}^x_i \\ u^x_{i+} &= \bar{\varepsilon}_x x_{i+} + \tilde{u}^x_i \end{aligned} \tag{5.17}$$

where the subscripts $i-$ and $i+$ indicate nodes on the opposite boundaries in Figure 5.2. These equations are used to eliminate the unknown term $\tilde{u}^x_i$. And the vertical and horizontal

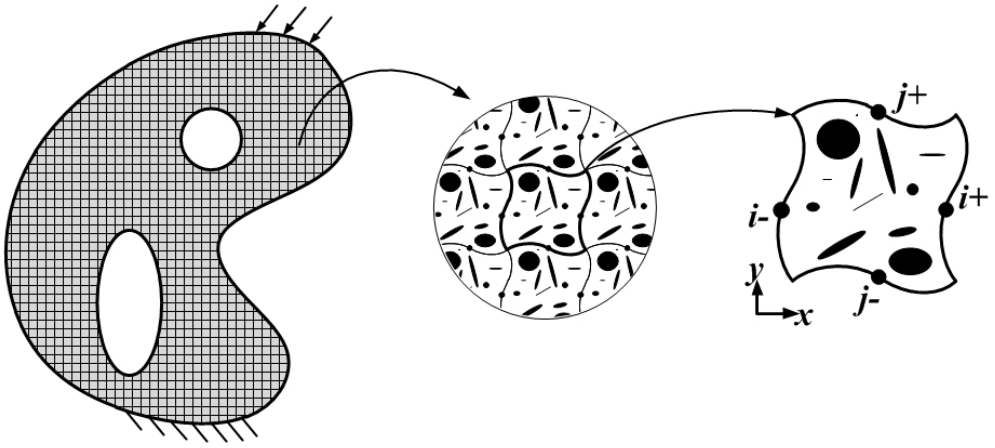

Figure 5.2: Illustration of the periodic base cell (PBC) and periodic boundary condition of the displacement of opposite nodes the on boundaries of a PBC.

displacement difference between the pair of nodes located on the horizontally opposite side of the PBC can be obtained as:

$$\begin{aligned} u^x_{i+} - u^x_{i-} &= \bar{\varepsilon}_x(x_{i+} - x_{i-}) = \bar{\varepsilon}_x L_x \\ u^y_{i+} - u^y_{i-} &= \tfrac{1}{2}\bar{\gamma}_{xy}(x_{i+} - x_{i-}) = \tfrac{1}{2}\bar{\gamma}_{xy} L_x \end{aligned} \tag{5.18}$$

where L_x is the dimension of the PBC in the x direction.

Similarly, the periodic boundary conditions for a pair of the vertical boundary nodes are

$$\begin{aligned} u^x_{j+} - u^x_{j-} &= \tfrac{1}{2}\bar{\gamma}_{xy}(y_{j+} - y_{j-}) = \tfrac{1}{2}\bar{\gamma}_{xy} L_y \\ u^y_{j+} - u^y_{j-} &= \bar{\varepsilon}_y(y_{i+} - y_{i-}) = \bar{\varepsilon}_y L_y \end{aligned} \tag{5.19}$$

where L_y is the dimension of the PBC in y direction correspondingly.

The listed periodic boundary condition for the four boundaries of the PBC is implemented in the finite element analysis by manually impose the displacement different onto the pairs of opposite boundary nodes.

Sensitivity analysis aims to estimate the impact of variations of design variables over the objective function sensitivity analysis is conducted hereafter.

The gradient of objective function with respect to the change of design variable x_i is for

bulk modulus can be calculated by:

$$\alpha = \frac{\partial f(x_e)}{\partial x_e} \tag{5.20}$$

where x_e is the design variable for each element e.

According to the relationships in Equation (5.13), the sensitivities for homogenized bulk or shear modulus can be computed as:

$$\frac{\partial \kappa^H}{\partial x_e} = \frac{1}{4}\left(\frac{\partial E^H_{11}}{\partial x_e} + \frac{\partial E^H_{12}}{\partial x_e} + \frac{\partial E^H_{21}}{\partial x_e} + \frac{\partial E^H_{22}}{\partial x_e}\right) \tag{5.21}$$

and

$$\frac{\partial G^H}{\partial x_e} = \frac{\partial E^H_{33}}{\partial x_e} \tag{5.22}$$

Using the adjoint variable method (Komkov et al., 1986), the sensitivity of the homogenized elasticity tensor with respect to design variable can be derived as:

$$\frac{\partial E^H_{ij}}{\partial x_e} = \frac{1}{|Y|}\int_\Omega \left(\left\{\varepsilon^i_0\right\} - \left\{\varepsilon^i\right\}\right)^T \frac{\partial E_{ij}}{\partial x_e}\left(\left\{\varepsilon^j_0\right\} - \left\{\varepsilon^j\right\}\right) d\Omega \tag{5.23}$$

Considering the material interpolation scheme defined in Equation (5.9), the sensitivity of the homogenized elasticity tensor can be written as:

$$\frac{\partial E^H_{ij}}{\partial x_e} = \frac{x_e}{|Y|}\int_\Omega \left(\left\{\varepsilon^i_0\right\} - \left\{\varepsilon^i\right\}\right)^T E^0_{ij}\left(\left\{\varepsilon^j_0\right\} - \left\{\varepsilon^j\right\}\right) d\Omega \tag{5.24}$$

The detailed optimisation procedure using BESO method can be illustrated by the Figure 5.3. We chose a simple or random PBC as the initial design and discretized the design domain by a ground structure. Then we define the objective volume fraction of the solid material V^*, evolutionary ratio ER. In the following step, we conduct finite element analysis over the PBC. Then we use homogenization method to get the effective bulk K or shear modulus G of the current configuration. Also, the sensitivities of homogenized parameters are calculated. The target volume for step i is defined as:

$$V_f^{i+1} = V_f^i\,(1 - ER) \quad when \quad V_f^i > V_f^* \tag{5.25}$$

Based on the relative ranking of the calculated overall sensitivity, a threshold of the sensitiv-

ity number, α_{th}^i, is determined by using the bi-section method so that the volume fraction in the next iteration is equal to V_f^{i+1}. The design variable of each element is modified by comparing its sensitivity number α_e^i with the threshold as

$$x_e^{i+1} = \begin{cases} \min(x_e^i + \Delta x, 1), \text{if} \alpha_e^i > \alpha_{th}^i \\ \max(x_e^i - \Delta x, 0), \text{if} \alpha_e^i < \alpha_{th}^i \end{cases} \tag{5.26}$$

where $\Delta x = 0.1$ throughout the paper. The above procedure is repeated until the convergence criteria are satisfied.

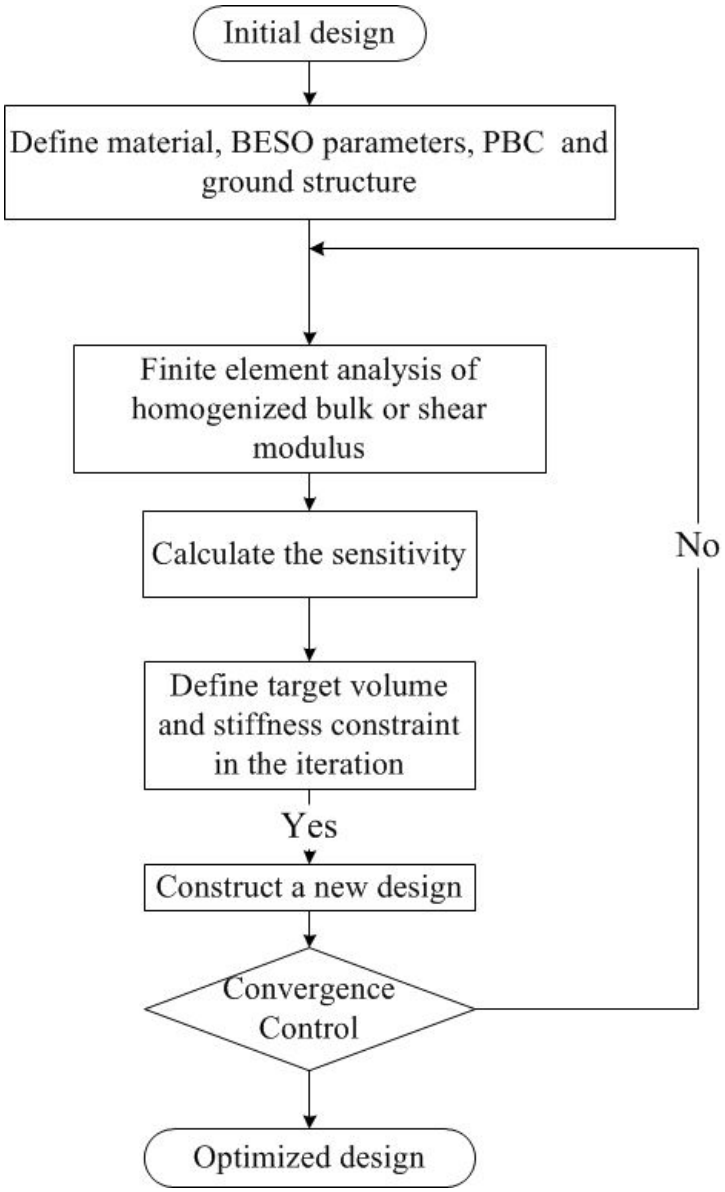

Figure 5.3: Flow chart of optimisation procedure using BESO method

5.4 Results and discussions

To illustrate the capability of the proposed algorithm, this section will present a number of optimisation results we obtained for maximizing the bulk and shear modulus, respectively. In the following examples, we consider the design of a 2D nano composite material with two phases, namely the solid material and void, the design domain is a square PBC. The objective is to maximize the stiffness of the PBC. All the numerical simulations are conducted with a volume constraint $V^* = 0.3V_0$, where V_0 is defined as the volume of the PBC with all members' diameter set to the upper limit D_0. For the PBC, as shown in Figure 5.4, if we assume the dimension of this PBC as $4L \times 4L$ then the upper limit of the diameter D_0 is set to be $L/10$.

5.4.1 2D materials with maximum bulk modulus

For designing microstructures for nanoporous material with maximum bulk modulus, the square design domain (PBC) with dimensions $4L \times 4L$ is discretized into a 4×4 ground structure with 200 2-node beam elements with size effects. As shown in Figure 5.4, the initial topology of the design domain discretized as a 4×4 ground structure, all members (marked as blue) have the upper limit diameter D_0 except for four members (marked as orange) align with the diagonal direction with the lower limit diameter $D_0 x_{e\_min}$ with $x_{e\_min} = 10^{-6}$. The constitutive materials are selected as silver (Shenoy, 2005), with the Young's modulus of E = 79e9 KPa and the Poisson's ratio of is $v = 0.3$, the surface parameters of silver is chosen as initial surface stress τ_0 = 1.21 N/m, surface elasticity E_s = 3.47 N/m. The BESO parameters are the evolution rate $ER = 0.01$.

The designed microstructures with a maximum bulk modulus of $K = 5.37$ GPa for a nano porous material with a base cell of size 40nm $\times$ 40nm are shown in Figure 5.5.

optimisations are conducted for this configuration on different scales, and the maximized bulk modulus for different length scales is plotted in Figure 5.6, from which we can see that the size effects of the material is observed. With the length scale change from macroscale (with unit size of 4m $\times$ 4m) to microscale (with unit size of 4um $\times$ 4um) to nanoscale (with unit size of 4nm $\times$ 4nm), the maximized bulk modulus of the cellular material exhibits an increasing trend, to be more specific, the bulk modulus is constant with in the um to m range which indicate that the size effects is not significant. However, this trend of constant bulk modulus changes as

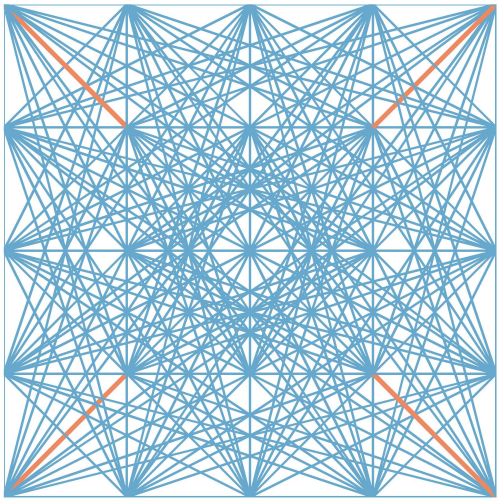

Figure 5.4: The initial topology of the 4×4 level five ground structure of the PBC for maximizing bulk modulus and the symmetrical initial distribution of the material: blue members have the initial diameter of D_0 and orange members have the initial diameter of $D_0 x_{e\_min}$

length scale go on shrinking toward nanometer. Particularly, when the scale smaller then um the surge of the bulk modulus is observed from around 4.5 GPa to more than 7.8 GPa. This size effects of the bulk modulus is consistent with the extensive experimental results and theoretical prediction in former chapters.

The optimized topology of the composite material, however, do not exhibits significant size-dependent property. As can be seen in Figure 5.6, the corresponding optimized topology for four major length scales, namely nm, um, mm, m, are listed on the top of the figure. And no significant change of the topology can be founded.

Figure 5.7 demonstrates the evolution histories of bulk modulus, volume fraction and the topology of the resulting microstructure. The total iterations of this optimisation are 300. As can be seen in Figure 5.7, the bulk modulus and the topology of the PBC converge to their final solutions with good stability, as long as the volume constraint is satisfied.

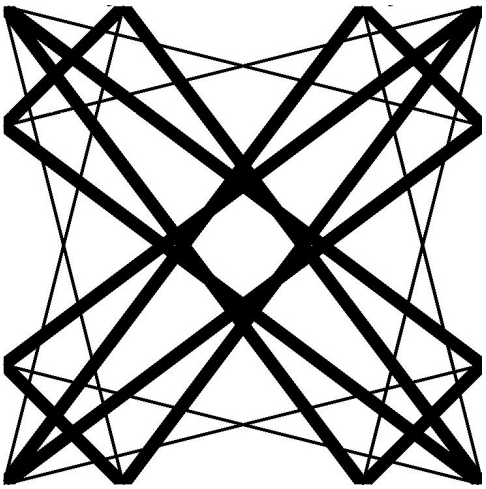

Figure 5.5: Microstructures of a single base cell obtained from the maximization of bulk modulus for a 2D composite material with PBC size 40nm $\times$ 40nm

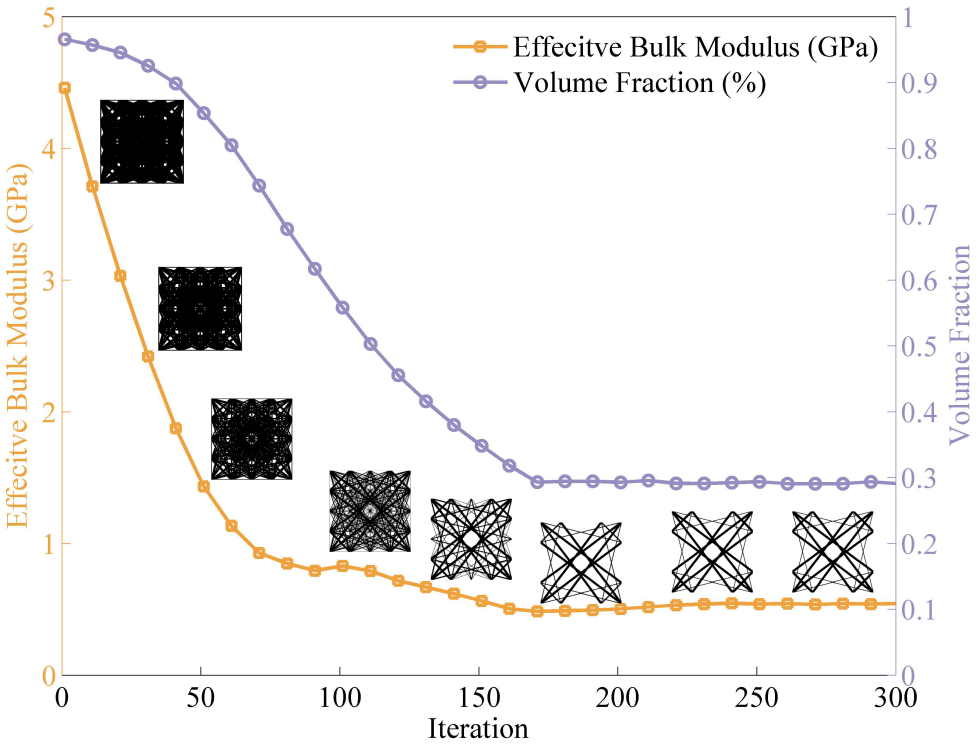

Figure 5.7: Evolution histories of the objective function, volume fraction, and topology for the maximization of bulk modulus and the PBC is shown in Figure 5.4. The size of the PBC is 40 nm.

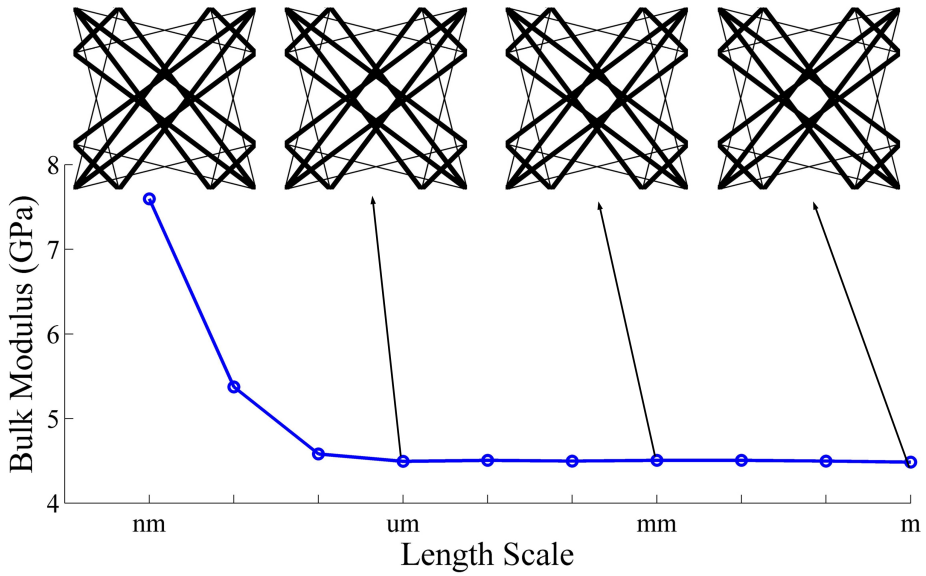

Figure 5.6: Microstructures of a single base cell obtained from the maximization of bulk modulus for a 2D composite material at different length scale and the maximized bulk modulus.

5.4.2 2D materials with maximum shear modulus

For designing microstructures for nano composite material with maximum shear modulus, similar optimisation setup is adopted with the optimisation of composite material with maximum bulk modulus. The constitutive materials are selected as silver with exactly the same mechanical properties and surface parameters with the maximization of bulk modulus, and the evolution rate $ER = 0.01$. The initial topology of this optimisation is a level two ground structure, The design domain (PBC) is discretized into a 4×4 ground structure and the initial topology is shown in Figure 5.8 with its members on the four boundaries set to be blue member with the upper limit diameter D_0 and the rest all internal members to be orange with the lower limit diameter $D_0 x_{e\_min}$ with $x_{e\_min} = 10^{-6}$.

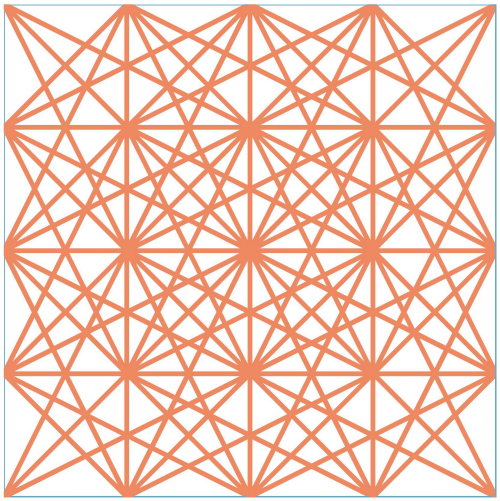

Figure 5.8: The initial topology of the 4×4 level two ground structure of the PBC for maximizing shear modulus and the symmetrical initial distribution of the material: blue members have the initial diameter of D_0 and orange members have the initial diameter of $D_0 x_{e\_min}$

The designed microstructures with a maximum shear modulus of $G = 3.82$ GPa for a nano porous material with a base cell of size 40nm $\times$ 40nm are shown in Figure 5.9.

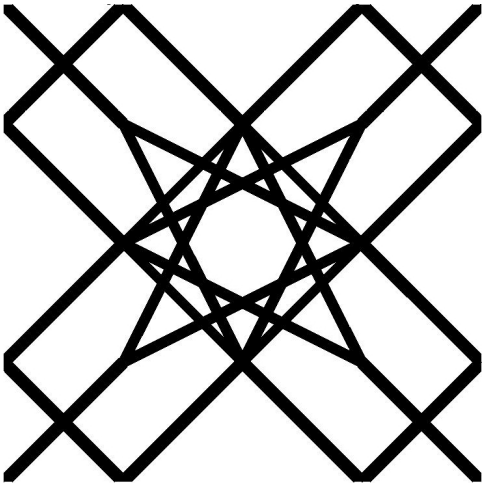

Figure 5.9: Microstructures of a single base cell obtained from the maximization of shear modulus for a 2D composite material with PBC size 40nm $\times$ 40nm

optimisations of maximization of shear modulus are conducted for this configuration on different scales, and the results for length scales span from nm to m is plotted in Figure 5.11. As can be seen that the size effects occurred. With the length scale change from the macroscale to the nanoscale, the maximized shear modulus of the cellular material exhibits an increasing trend. There is a plateau stage within the um to m range indicating that the size effects is

negligible. As length scale approaches to the nanometer, this trend of constant shear modulus changes. When the scale smaller then um a dramatic increasing of the shear modulus occurred from around 2.5 GPa to more than 6.8 GPa. This size effects of the shear modulus agrees with the experimental observation as well as the simulations mentioned in former chapters.

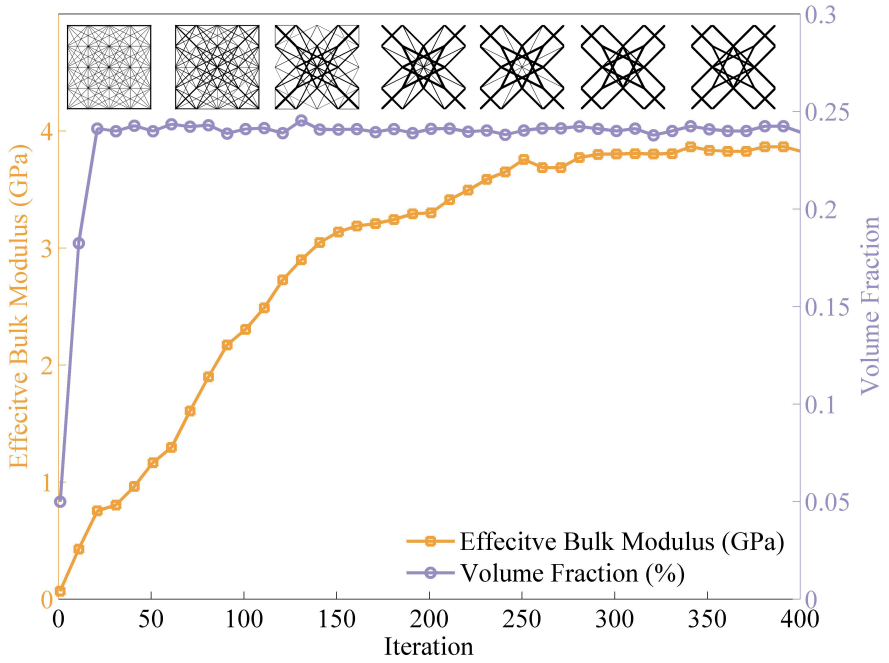

Figure 5.10: Evolution histories of the objective function, volume fraction, and topology for the maximization of shear modulus and the PBC is shown in Figure 5.8. The size of the PBC is 40 nm.

Figure 5.10 demonstrates the evolution histories of shear modulus, volume fraction and the topology of the resulting microstructure. The total iterations of this optimisation are 400. As can be seen in Figure 5.10, the shear modulus and the topology of the PBC converge to their final solutions with a slower speed compared with that for maximization of bulk modulus.

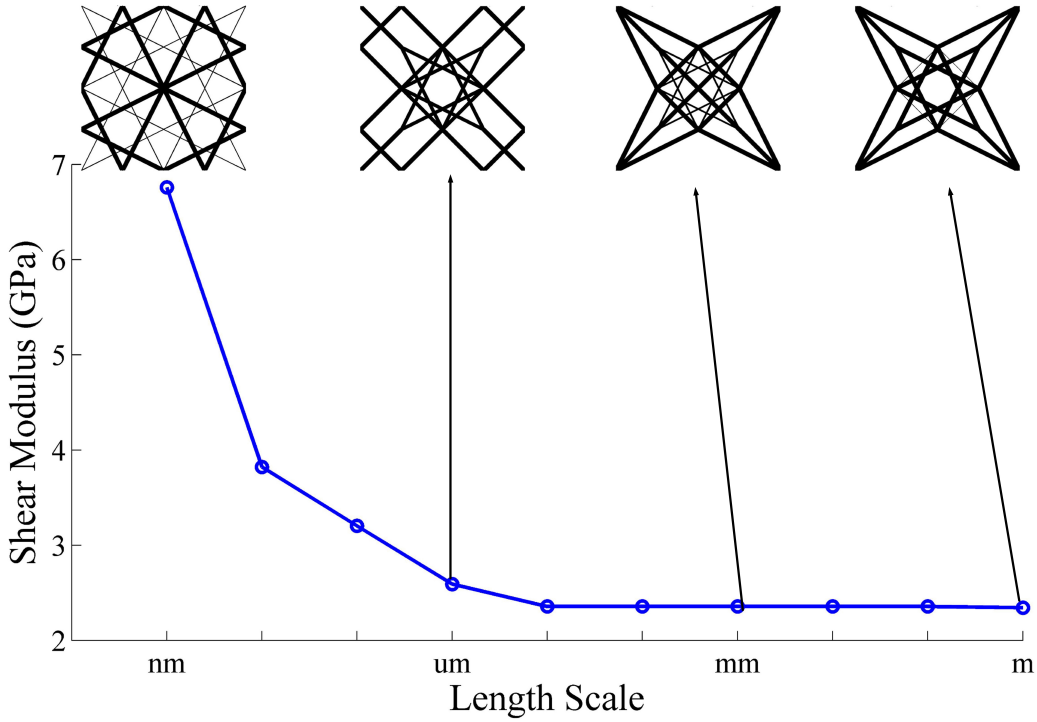

Figure 5.11: Microstructures of a single base cell obtained from the maximization of shear modulus for a 2D composite material at different length scale and the maximized shear modulus.

Unlike the result of the optimisation of bulk modulus, the optimized topology of the composite material demonstrated series of different topologies as the size changes. As can be seen in Figure 5.11, the corresponding optimized topology for four major length scales, namely nm, um, mm, m, are listed on the top of the figure. The microstructure tends to converge to the diagonal shape which is observed in the conventional optimisation of material with extreme stiffness (Huang et al., 2011).

5.5 Summary

In this chapter the nanostructures are designed by structural topology optimisation, in which the structure are represented by a great number of circular beams connecting among all nodes and the properties are extracted by homogenization theory with the consideration of size effects. The diameter of individual beams can be reduced and increased in terms of their sensitivity.

The optimized stiffness indicate an increasing trend for both shear and bulk modulus with the decreasing of the length scale from the um to nm, which is consistent with the experimental observations and the simulation works in previous chapters. It is interesting to note that the shear modulus exhibits obvious size effects while the bulk modulus is size-independent.

In summary, we develop a topology optimisation scheme that could make use of the exceptional size-dependent mechanical property. Material that has several time larger stiffness could be achieved when the dimension of the microstructure of the material is less than 100 nm.

CHAPTER 6

CONCLUSIONS

The exceptional size-dependent mechanical property of materials at nanoscale breaks the conventional scaling laws. To explore the underline mechanisms of such size effects, this thesis studies the dramatic changes of mechanical properties for porous nanomaterials theoretically and computationally.

In Chapter 2, the material is simplified by self-repeated representative unit cells in the shape of an octahedra. By taking into account surface effects with Young-Laplace equation and Euler-Bernoulli beam theory, the dependence of Young's modulus on the length scale is established, whose effectiveness has been validated by experimental data. Through parameter investigation, I have found that by considering the surface effects the predicted stiffness using Euler-Bernoulli beam theory compares well to experimental data for spongelike nanoporous gold with random microstructures. Analytical results show that, of the two factors influencing the effective Young's modulus, the residual stress is more important than the surface stiffness.

However, the analytical approach proposed in Chapter 2 becomes invalid for complex structures in real situations. Therefore, in Chapter 3 an iterative algorithm is developed by considering the size effects as distributed pressure acting on the external surface in terms of the generalized Young-Laplace equation. Because the magnitude of pressure depends on the principal curvatures, iterative steps are adopted to gradually stabilize the structure in finite element analysis. Computational results are in good agreement with both experiment data and theoretical prediction. Furthermore, the investigation on strengthened and softened Young's modulus for two complex nanostructures demonstrates that the proposed computational method provides a general and effective approach to analyze the size effects for nanostructures in arbitrary shape.

To tackle the convergence issue of the iterative algorithm, a new finite element with size

effects integrated into the stiffness matrix is proposed and validated by experiment data in Chapter 4. The surface elasticity theory and generalized Young-Laplace equation are integrated into a beam element to account for the size effects in classical Euler–Bernoulli and Timoshenko beam theories. Computational results match well with the theoretical predictions on the size effects for a cantilever beam and a cubic unit cell containing 24 horizontal/vertical ligaments. For a simply supported nanowire, it is found that the results are very close to the experimental data. With the assumption that nanoporous gold is composed of many randomly connected beams, for the first time, the size effects of such a complex structure is numerically determined.

By incorporating this new element with the structural topology optimisation algorithm BESO, I conducted the topology optimisation to design the microstructure of a nanoporous material with extreme bulk and shear modulus to utilized the size effects in Chapter 6. Both the structures optimised to have the maximal shear modulus and maximal bulk modulus exhibit some extent of size effects, namely these values increase with the decrease of structural scale. However, the former responds more actively to the change of size in comparison with the later.

The anti-intutive size effects which have been predicted in theoretical analysis and validated in experiments could bring a revolution to areas like sensor, lightweight structure, high-performance material, catalysis, and actuating, and has great potential to be utilized in the design of novel, versatile materials, which has promising applications in micro- and nano-electrical and mechanical system (M/NEMS). However, the mechanisms and property of the material behaviour at low dimension still need further study.

The integration of surface elasticity with generalized Young-Laplace equation do provides a powerful tool to study the size effects, and have been successfully adopted in the analysis of material with both simple geometry and complex topology.

However, to my best knowledge, the size effects have not been embedded into the finite element analysis, which has been widely applied in many fields of engineering. The main difficulty of this application is attributed to the integration of curvature item, the main feature of Young-Laplace equation, into the solid element. Fortunately, the curvature is an inherent item in beam, plate and shell element, which inspires me to develop a new curvature-related element to account for the size effects for general 3D continuum problems. The integration of Young-Laplace equation with the solid element is more useful and will be solved in further study.

The theory of surface elasticity in the size-dependence of material properties is applicable to structured single-phase materials and composites materials. For simplicity, only nanoporous materials composed of void phase and solid phase are studied in this thesis Though some benchmarked characterisaiton of size effects can be predicted in accordance with the findings of this thesis, further studies are still in need as they could be caused by other complex factors which have not considered in this research.

Appendices

Appendix A

Implementation of iterative finite element analysis

The detailed implementation of the iterative algorithm proposed in Chapter 3 as Abaqus user subroutine.

```
subroutine initialAnalysis
    use ShareInfo
    character*256 tmp
    integer i,e
    integer kitau, kiEs, kiunit
    CALL GETJOBNAME( JOBNAME, LENJOBNAME )
    kitau = index(jobname,'tau')
    kiEs = index(jobname,'Es')
    kiunit = index(jobname,'Unit')
    tmp = jobname(kitau+3:kiEs-2)
    READ(tmp,*,IOSTAT=e) ktau0
    tmp = jobname(kiEs+2:kiunit-2)
    READ(tmp,*,IOSTAT=e) kEs
    tmp = jobname(kiunit+4:lenjobname)
    READ(tmp,*,IOSTAT=e) kunit
    write(*,*)
    write(*,*)
    write(*,*) '
   ********************************************************************************
   '
```

```
19      write(*,*) '                                Start Analysis !
                    '
        write(*,*) '    Initail condition:
                    '
21      write(*,'(a48f13.5)') '           Inital Surface Tension (ktau0 N/m):
        ',ktau0
        write(*,'(a49f13.5)') '           Inital Surface Elesticity ( kEs N/m)
        : ',kEs
23      write(*,'(a41f13.5)') '          RVE unit length(1 = kunit nm): ',
        kunit
        write(*,*) '
        ********************************************************************
        '
25      write(*,*)
        write(*,*)
27      write(7,*)
        write(7,*)
29      write(7,*) '
        ********************************************************************
        '
        write(7,*) '                                Start Analysis !
                    '
31      write(7,*) '    Initail condition:
                    '
        write(7,'(a42f13.5)') '           Inital Surface Tension (ktau0 N/m):
        ',ktau0
33      write(7,'(a44f13.5)') '           Inital Surface Elesticity ( kEs N/m)
        : ',kEs
        write(7,'(a41i8)') '          RVE unit length(1 = kunit nm): ',kunit
35      write(7,*) '
        ********************************************************************
        '
        write(7,*)
37      write(7,*)
        return
39  endsubroutine initialAnalysis
```

```
41 subroutine writeNodeSet(stnm)
       use ShareInfo
43     character(*) :: stnm
       character*80 :: filename
45     integer :: i,j
       logical :: setexit
47     setexit = .false.
       do i = 1, size(kLabelList,dim=1)
49         if (trim(adjustl(kLabelList(i))) == trim(adjustl(stnm))) then
               setexit = .true.
51             exit
           endif
53     enddo
       if (setexit) then
55         filename = 'ndSet_'//trim(adjustl(stnm))//'.txt'
           open(kfunit,file=fileplace//trim(adjustl(filename)),status='
      replace',recl=250)
57         do j = 1,kNodeSetNds(i)
               write(kfunit,*) kNodeSet(i)%kNodeList(j), kNode(kNodeSet(i)%
      kNodeList(j),1:3)
59         enddo
           close(kfunit)
61         kfunit = kfunit + 1
       else
63         write(*,*) 'Error! Node Set', setnum,'Not Founded !'
       endif
65     return
   endsubroutine writeNodeSet
67
   subroutine writeElementSet(stnm)
69     use ShareInfo
       character(*) :: stnm
71     character*80 :: filename
       integer :: i,j,k
73     logical :: setexit
       setexit = .false.
75     do i = 1, size(kLabelList,dim=1)
```

```
        if (trim(adjustl(kLabelList(i))) == trim(adjustl(stnm))) then
77          setexit = .true.
            exit
79      endif
    enddo
81  if (setexit) then
        filename = 'eleSet_'//trim(adjustl(stnm))//'.txt'
83      open(kfunit,file=fileplace//trim(adjustl(filename)),status='
    replace',recl=250)
        do j = 1,size(kElementSet,dim=1)
85          if (kElementSet(j)%ksetNum == i) then
                exit
87          endif
        enddo
89      do k = 1,kElementSetEles(j)
            write(kfunit,*) kElementSet(j)%kElementList(k),kElement(
    kElementSet(j)%kElementList(k),1:4)
91      enddo
        close(kfunit)
93      kfunit = kfunit + 1
    else
95      write(*,*) 'Error! Element Set', setnum,'Not Founded !'
    endif
97  return
endsubroutine writeElementSet
99
subroutine writeDload(knstep)
101 use ShareInfo
    include 'aba_param.inc'
103 integer :: knstep
    character*80 :: kflnm,filename
105 dimension array(513),jrray(nprecd,513),time(2)
    integer realNdNum, mapNdNum, knsrf
107 integer :: i
    kflnm = 'DLOAD_'
109 write (filename, *) knstep
    filename = adjustl(filename)
```

```
111     open(kfunit,file=fileplace//trim(adjustl(kflnm))//trim(adjustl(
        filename))//'.txt',status='replace',recl=250)
        do i = 1, size(kCurrentLoad,dim=1)
113         write(kfunit,*) i,kCurrentLoad(i)
        enddo
115     close(kfunit)
        kfunit = kfunit + 1
117     return
    endsubroutine
119
    subroutine writeSurfaceData(infokey,knstep,knsrf,ldsf_index)
121     use ShareInfo
        include 'aba_param.inc'
123     integer :: knstep
        character(*) :: infokey
125     character*80 :: kflnm,filename
        dimension array(513),jrray(nprecd,513),time(2)
127     integer realNdNum, mapNdNum, knsrf
        integer realEleNum, mapEleNum
129     integer :: i,l
        integer :: ldsf_index
131     if (trim(adjustl(infokey)) == 'ELEM') then
            filename = trim(adjustl(kLabelList(knsrf)))//'_ELE'
133         open(kfunit,file=fileplace//trim(adjustl(filename))//'.txt',status
        ='replace',recl=250)
            do i = 1, size(kLoadSurface(ldsf_index)%kSurfaceTri,dim=1)
135             realEleNum = kLoadSurface(ldsf_index)%kSurfaceTri(i,1)
                mapEleNum  = kLoadSurface(ldsf_index)%kEleMap(realEleNum)
137             write(kfunit,*) realEleNum,mapEleNum,kElement(realEleNum,:),&
                    kLoadSurface(ldsf_index)%kSurfaceTri(i,4:6),&
139                 kLoadSurface(ldsf_index)%kFV_faces(i,1:3)
            enddo
141         close(kfunit)
            kfunit = kfunit + 1
143     elseif (trim(adjustl(infokey)) == 'ELESTRN') then
            kflnm = trim(adjustl(kLabelList(knsrf)))//'_EEL_E_'
145         write (filename, *) knstep
```

```
        filename = adjustl(filename)
147     open(kfunit,file=fileplace//trim(adjustl(kflnm))//trim(adjustl(
    filename))//'.txt',status='replace',recl=250)
        do i = 1, size(kLoadSurface(ldsf_index)%kSurfaceTri,dim=1)
149         write(kfunit,*) kLoadSurface(ldsf_index)%kSurfaceTri(i,1),
    kLoadsurface(ldsf_index)%kgS_Tensor(i,1:6)
        enddo
151     close(kfunit)
        kfunit = kfunit + 1
153  elseif (trim(adjustl(infokey)) == 'NDSTRN') then
        kflnm = trim(adjustl(kLabelList(knsrf)))//'_ND_E_'
155     write (filename, *) knstep
        filename = adjustl(filename)
157     open(kfunit,file=fileplace//trim(adjustl(kflnm))//trim(adjustl(
    filename))//'.txt',status='replace',recl=250)
        do i = 1, kNodeSetNds(knsrf)
159         realNdNum = kNodeSet(knsrf)%kNodeList(i)
            mapNdNum  = kLoadSurface(ldsf_index)%kNdMap(realNdNum)
161         write(kfunit,*) realNdNum,mapNdNum,kLoadsurface(ldsf_index)%
    klS_Tensor(i,1:6)
        enddo
163     close(kfunit)
        kfunit = kfunit + 1
165  elseif (trim(adjustl(infokey)) == 'NDDISP') then
        kflnm = trim(adjustl(kLabelList(knsrf)))//'_ND_U_'
167     write (filename, *) knstep
        filename = adjustl(filename)
169     open(kfunit,file=fileplace//trim(adjustl(kflnm))//trim(adjustl(
    filename))//'.txt',status='replace',recl=250)
        do i = 1, kNodeSetNds(knsrf)
171         realNdNum = kNodeSet(knsrf)%kNodeList(i)
            mapNdNum  = kLoadSurface(ldsf_index)%kNdMap(realNdNum)
173         write(kfunit,*) realNdNum,mapNdNum,kLoadsurface(ldsf_index)%
    kX0Y0Z0(i,1:3),kLoadsurface(ldsf_index)%kdxdydz(i,1:3)
        enddo
175     close(kfunit)
        kfunit = kfunit + 1
```

```
177     elseif (trim(adjustl(infokey)) == 'CURVATURE') then
            kflnm = trim(adjustl(kLabelList(knsrf)))//'_CURVATURE_'
179         write (filename, *) knstep
            filename = adjustl(filename)
181         open(kfunit,file=fileplace//trim(adjustl(kflnm))//trim(adjustl(
    filename))//'.txt',status='replace',recl=250)
            do i = 1, kNodeSetNds(knsrf)
183             realNdNum = kNodeSet(knsrf)%kNodeList(i)
                mapNdNum  = kLoadSurface(ldsf_index)%kNdMap(realNdNum)
185             write(kfunit,*) realNdNum,mapNdNum,kLoadsurface(ldsf_index)%
    kLambda1(i),kLoadsurface(ldsf_index)%kLambda2(i),&
                    kLoadsurface(ldsf_index)%kDir1(i,1:3),kLoadsurface(
    ldsf_index)%kDir2(i,1:3)
187         enddo
            close(kfunit)
189         kfunit = kfunit + 1
        endif
191 endsubroutine

193 subroutine getMesh()
        use ShareInfo
195     include 'aba_param.inc'
        dimension array(513),jrray(nprecd,513),time(2)
197     equivalence (array(1),jrray(1,1))
        integer ndCntr, eleCntr
199     integer ndSetCntr, lblCntr, eleSetCntr
        integer knNum
201     character*8 kaNum
        ndCntr     = 0
203     eleCntr    = 0
        lblCntr    = 0
205     ndSetCntr  = 0
        eleSetCntr = 0
207     call dbfile(0,array,jrcd)
        do while (jrcd == 0)
209         call dbfile(0,array,jrcd)
        enddo
```

```
211     call dbfile(2,array,jrcd)
        do while (jrcd == 0)
213         call dbfile(0,array,jrcd)
            NW= jrray(1,1) ! Record length (NW)
215         key = jrray(1,2) ! Record key
            if (key == 1901) then
217             ndCntr = ndCntr + 1
            elseif (key == 1900) then
219             eleCntr = eleCntr + 1
            elseif (key == 1931) then !'Test of kNode Set definition'
221             ndSetCntr = ndSetCntr + 1
            elseif (key == 1933) then !'Test of kElement Set definition'
223             eleSetCntr = eleSetCntr + 1
            elseif (key == 1940) then !'Test of label cross reference'
225             lblCntr = lblCntr + 1
            endif
227     enddo
        allocate(kElementSetEles(eleSetCntr))
229     kElementSetEles = 0
        allocate(kNodeSetNds(ndSetCntr))
231     kNodeSetNds    = 0
        allocate(kLabelList(lblCntr))
233     lblCntr = 0
        ndSetCntr = 0
235     eleSetCntr = 0
        call dbfile(2,array,jrcd)
237     do while (jrcd == 0)
            call dbfile(0,array,jrcd)
239         NW= jrray(1,1) ! Record length (NW)
            key = jrray(1,2) ! Record key
241         if (key == 1931) then !'Test of kNode Set definition'
                ndSetCntr = ndSetCntr + 1
243             kNodeSetNds(ndSetCntr) = kNodeSetNds(ndSetCntr) + NW -4 + 1
            elseif (key == 1932) then !'Test of kNode Set continuation'
245             kNodeSetNds(ndSetCntr) = kNodeSetNds(ndSetCntr) + NW -3 + 1
            elseif (key == 1933) then !'Test of kElement Set definition'
247             eleSetCntr = eleSetCntr + 1
```

```
            kElementSetEles(eleSetCntr) = kElementSetEles(eleSetCntr) + NW
    - 4 + 1
        elseif (key == 1934) then !'Test of kElement Set continuation'
            kElementSetEles(eleSetCntr) = kElementSetEles(eleSetCntr) + NW
    - 3 + 1
        elseif (key == 1940) then !'Test of label cross reference'
            lblCntr = lblCntr + 1
            write(kLabelList(lblCntr),'(<NW>a8)') array(4:NW)
        endif
    enddo
    call dbfile(2,array,jrcd)
    allocate(kNode(ndCntr,3))
    allocate(kElement(eleCntr,4))
    allocate(kNodeSet(ndSetCntr))
    do k = 1, ndSetCntr
        allocate(kNodeSet(k)%kNodeList(kNodeSetNds(k)))
    enddo
    allocate(kElementSet(eleSetCntr))
    do k = 1, eleSetCntr
        allocate(kElementSet(k)%kElementList(kElementSetEles(k)))
    enddo
    ndCntr    = 0
    eleCntr   = 0
    ndSetCntr = 0
    eleSetCntr = 0
    do while (jrcd == 0)
        call dbfile(0,array,jrcd)
        NW= jrray(1,1) ! Record length (NW)
        key = jrray(1,2) ! Record key
        if (key == 1901) then !'Test of kNode definition'
            ndCntr          = ndCntr + 1
            kNode(ndCntr,1) = array(4)
            kNode(ndCntr,2) = array(5)
            kNode(ndCntr,3) = array(6)
        elseif (key == 1900) then !'Test of kElement definition'
            eleCntr             = eleCntr + 1
            kElement(eleCntr,1) = jrray(1,5)
```

```
283             kElement(eleCntr,2) = jrray(1,6)
                kElement(eleCntr,3) = jrray(1,7)
285             kElement(eleCntr,4) = jrray(1,8)
            elseif (key == 1931) then !'Test of kNode Set definition'
287             ndSetCntr = ndSetCntr + 1
                write(kaNum,'(a8)') array(3)
289             read(kaNum,'(i8)') knNum
                kNodeSet(ndSetCntr)%ksetNum = knNum
291             do k = 1,NW - 4 + 1
                    kNodeSet(ndSetCntr)%kNodeList(k) = jrray(1,k + 4 - 1)
293             enddo
            elseif (key == 1932) then !'Test of kNode Set continuation'
295             do l = k, k + NW - 3
                    kNodeSet(ndSetCntr)%kNodeList(l) = &
297                     jrray(1,l+ 3 - k)
                enddo
299             k = l ! update counter
            elseif (key == 1933) then !'Test of kElement Set definition'
301             eleSetCntr = eleSetCntr + 1
                write(kaNum,'(a8)') array(3)
303             read(kaNum,'(i8)') knNum
                kElementSet(eleSetCntr)%ksetNum = knNum
305             do i = 1,NW - 4 + 1
                    kElementSet(eleSetCntr)%kElementList(i) = &
307                     jrray(1,i + 4 - 1)
                enddo
309         elseif (key == 1934) then !'Test of kElement Set continuation'
                do j = i, i + NW - 3
311                 kElementSet(eleSetCntr)%kElementList(j) = &
                        jrray(1,j+ 3 - i)
313             enddo
                i = j ! update counter
315         endif
        enddo
317     return
    endsubroutine getMesh
319
```

```
subroutine getSurface()
    use ShareInfo
    include 'aba_param.inc'
    dimension array(513),jrray(nprecd,513),time(2)
    equivalence (array(1),jrray(1,1))
    integer srfCntr
    integer knNum,nSrfNum,facetNum
    integer mx,i,j,k,l
    character*8 kaNum
    character*8 aSrfNum
    srfCntr = 0
    call dbfile(0,array,jrcd)
    do while (jrcd == 0)
        call dbfile(0,array,jrcd)
    enddo
    call dbfile(2,array,jrcd)
    do while (jrcd == 0)
        call dbfile(0,array,jrcd)
        NW= jrray(1,1) ! Record length (NW)
        key = jrray(1,2) ! Record key
        if (key == 1501) then !'Test of Surface definition '
            srfCntr = srfCntr + 1
        endif
    enddo
    allocate(kLoadSurfaceLabelNumList(srfCntr))
    allocate(kLoadSurface(srfCntr))
    srfCntr   = 0
    call dbfile(0,array,jrcd)
    do while (jrcd == 0)
        call dbfile(0,array,jrcd)
    enddo
    call dbfile(2,array,jrcd)
    do while (jrcd == 0)
        call dbfile(0,array,jrcd)
        NW= jrray(1,1) ! Record length (NW)
        key = jrray(1,2) ! Record key
        if (key == 1501) then !'Test of Surface definition '
```

```
357             srfCntr = srfCntr + 1
                write(aSrfNum,'(a8)') array(3)
359             read(aSrfNum,'(i8)') nSrfNum
                kLoadSurfaceLabelNumList(srfCntr) = nSrfNum
361             facetNum = jrray(1,6)
                allocate(kLoadSurface(srfCntr)%kSurfaceTri(facetNum,6))
363             do i = 1,facetNum
                    call dbfile(0,array,jrcd)
365                 do j = 1,6
                        kLoadSurface(srfCntr)%kSurfaceTri(i,j) = jrray(1,j+2)
367                 enddo
                enddo
369             mx = 0
                do i = 1, kNodeSetNds(nSrfNum)
371                 if (kNodeSet(nSrfNum)%kNodeList(i) > mx) then
                        mx = kNodeSet(nSrfNum)%kNodeList(i)
373                 endif
                enddo
375             allocate(kLoadSurface(srfCntr)%kNdMap(mx))
                kLoadSurface(srfCntr)%kNdMap = -1
377             do i = 1, kNodeSetNds(nSrfNum)
                    kLoadSurface(srfCntr)%kNdMap(kNodeSet(nSrfNum)%kNodeList(i
    )) =i
379             enddo
                mx = 0
381             do j = 1,size(kElementSet)
                    if (kElementSet(j)%ksetNum == nSrfNum) then
383                     exit
                    endif
385             enddo
                do i = 1, kElementSetEles(j)
387                 if (kElementSet(j)%kElementList(i) > mx) then
                        mx = kElementSet(j)%kElementList(i)
389                 endif
                enddo
391             allocate(kLoadSurface(srfCntr)%kEleMap(mx))
                kLoadSurface(srfCntr)%kEleMap = -1
```

```
393             do i = 1, kElementSetEles(j)
                    kLoadSurface(srfCntr)%kEleMap(kElementSet(j)%kElementList(
    i)) =i
395             enddo
                Allocate(kLoadSurface(srfCntr)%kFV_faces(facetNum,3))
397             Allocate(kLoadSurface(srfCntr)%kX0Y0Z0(kNodeSetNds(nSrfNum),3)
    )
                Allocate(kLoadSurface(srfCntr)%kdxdydz(kNodeSetNds(nSrfNum),3)
    )
399             kLoadSurface(srfCntr)%kdxdydz = 0.D0
                Allocate(kLoadSurface(srfCntr)%kXYZ(kNodeSetNds(nSrfNum),3))
401             kLoadSurface(srfCntr)%kXYZ = 0.D0
                do i = 1,size(kElementSet)
403                 if (kElementSet(i)%ksetNum == nSrfNum) then
                        exit
405                 endif
                enddo
407             Allocate(kLoadSurface(srfCntr)%kgS_Tensor(kElementSetEles(i)
    ,6))
                Allocate(kLoadSurface(srfCntr)%kAvS_Tensor(kNodeSetNds(nSrfNum
    ),6))
409             kLoadSurface(srfCntr)%kAvS_Tensor(kNodeSetNds(nSrfNum),6) = 0.
    D0
                Allocate(kLoadSurface(srfCntr)%klS_Tensor(kNodeSetNds(nSrfNum)
    ,6))
411             kLoadSurface(srfCntr)%klS_Tensor(kNodeSetNds(nSrfNum),6) = 0.
    D0
                Allocate(kLoadSurface(srfCntr)%kDLoad(kNodeSetNds(nSrfNum)))
413         endif
        enddo
415     mx = 0
        do k = 1,size(kLoadSurface)
417         nSrfNum = kLoadSurfaceLabelNumList(k)
            do i = 1, kNodeSetNds(nSrfNum)
419             if (kNodeSet(nSrfNum)%kNodeList(i)>mx) then
                    mx = kNodeSet(nSrfNum)%kNodeList(i)
421             endif
```

```
            enddo
423       enddo
          allocate(kCurrentLoad(mx))
425       kCurrentLoad = 0.D0
          allocate(kPreviousLoad(mx))
427       kPreviousLoad = 0.D0
          do k = 1,size(kLoadSurface)
429           nSrfNum = kLoadSurfaceLabelNumList(k)
              n = kNodeSetNds(nSrfNum)
431           allocate(kLoadSurface(k)%kSharedElement(n,21))
              kLoadSurface(k)%kSharedElement = -1
433           do j = 1,size(kLoadSurface(k)%kSurfaceTri,dim = 1)
                  do l = 1,3
435                   realNdNum = kLoadSurface(k)%kSurfaceTri(j,l+3)
                      mapNdNum  = kLoadSurface(k)%kNdMap(realNdNum)
437                   m = kLoadSurface(k)%kSharedElement(mapNdNum,1) + 3
                      kLoadSurface(k)%kSharedElement(mapNdNum,m) = kLoadSurface(
      k)%kSurfaceTri(j,1)
439                   kLoadSurface(k)%kSharedElement(mapNdNum,1) = kLoadSurface(
      k)%kSharedElement(mapNdNum,1) + 1
                  enddo
441           enddo
          enddo
443       return
    endsubroutine getSurface
445
    subroutine updatSurface(nstep,ninc)
447       use ShareInfo
          include 'aba_param.inc'
449       dimension array(513),jrray(nprecd,513),time(2)
          equivalence (array(1),jrray(1,1))
451       integer mx,i,j,k,l,nstep,ninc
          double precision,dimension(6) :: tSTnsr! temp strain tensor
453       double precision,dimension(3,3) :: tgSTnsr! temp strain tensor
          double precision,dimension(3,3) :: tlSTnsr! temp strain tensor
455       double precision,dimension(3,3) :: tMatrix ! transformation matrix
          integer realNdNum, mapNdNum
```

```
457     integer labelNum
        character*8 aSrfNum
459     logical isSrf
        call dbfile(0,array,jrcd)
461     do while (jrcd == 0)
            call dbfile(0,array,jrcd)
463     enddo
        call dbfile(2,array,jrcd)
465     call posfil(nstep,ninc,array,jrcd)
        do while (jrcd == 0)
467         call dbfile(0,array,jrcd)
            NW= jrray(1,1) ! Record length (NW)
469         key = jrray(1,2) ! Record key
            if (key == 1911) then
471             isSrf = .false. ! flag that this labelnum is a kLoadSurface
                write(aSrfNum,'(a8)') array(4)
473             read(aSrfNum,'(i8)') labelNum ! set Num
                do k = 1,size(kLoadSurfaceLabelNumList,dim=1)
475                 if (kLoadSurfaceLabelNumList(k) == labelNum) then
                        l = k
477                     isSrf=.true.
                    endif
479             enddo
                if (isSrf) then
481                 if (jrray(1,3) == 1) then ! Flag for nodal output
                        call dbfile(0,array,jrcd)
483                     if (jrray(1,2) == 101) then ! key: 101 U displacement
                            do j = 1,3
485                             kLoadSurface(l)%kdxdydz(1,j) = array(j+3)
                            enddo
487                         do i = 2,kNodeSetNds(labelNum)
                                call dbfile(0,array,jrcd)
489                             do j = 1,3
                                    kLoadSurface(l)%kdxdydz(i,j) = array(j+3)
491                             enddo
                            enddo
493                     endif
```

```
                elseif (jrray(1,3) == 0) then ! ! Flag for kElement output
495                 do i = 1,size(kElementSet)
                        if (kElementSet(i)%ksetNum == labelNum) then
497                         labelNum = i
                            exit
499                     endif
                    enddo
501                 do i = 1,kElementSetEles(labelNum)
                        call dbfile(0,array,jrcd)
503                     call dbfile(0,array,jrcd)
                        if (jrray(1,2) == 21) then ! Flag for strain E
505                         do j = 1,6
                                kLoadSurface(1)%kgS_Tensor(i,j) = array(j
+2)
507                         enddo
                        endif
509                 enddo
                endif
511         endif
        endif
513 enddo
    do k = 1,size(kLoadSurface)
515     nSrfNum = kLoadSurfaceLabelNumList(k)
        do i = 1,size(kLoadSurface(k)%kSurfaceTri,dim=1)
517         do j = 1,3
                realNdNum = kLoadSurface(k)%kSurfaceTri(i,j+3)
519             mapNdNum  = kLoadSurface(k)%kNdMap(realNdNum)
                kLoadSurface(k)%kFV_faces(i,j) = mapNdNum
521         enddo
        enddo
523     do i = 1, kNodeSetNds(nSrfNum)
            do j = 1,3
525             kLoadSurface(k)%kX0Y0Z0(i,j)= kNode(kNodeSet(nSrfNum)%
kNodeList(i),j)
                kLoadSurface(k)%kXYZ(i,j)= kLoadSurface(k)%kX0Y0Z0(i,j) +
kLoadSurface(k)%kdxdydz(i,j)
527         enddo
```

```
        enddo
529     call patchcurvature(kLoadsurface(k)%kFV_faces,kLoadSurface(k)%kXYZ
,kLoadSurface(k)%kLambda1, &
        & kLoadSurface(k)%kLambda2,kLoadSurface(k)%kDirN,kLoadSurface(
k)%kDir1,kLoadSurface(k)%kDir2,kLoadSurface(k)%kMeanC, &
531     & kLoadSurface(k)%kGaussianC)
        do i = 1, kNodeSetNds(nSrfNum)
533         tSTnsr = 0.D0
            realNdNum = kNodeSet(nSrfNum)%kNodeList(i)
535         mapNdNum  = kLoadSurface(k)%kNdMap(realNdNum)
            do j = 2,kLoadsurface(k)%kSharedElement(mapNdNum,1) + 2
537             realEleNum = kLoadSurface(k)%kSharedElement(mapNdNum,j)
                mapEleNum  = kLoadSurface(k)%kEleMap(realEleNum)
539             do l = 1,6
                    tSTnsr(l) = tSTnsr(l) + kLoadsurface(k)%kgS_Tensor(
mapEleNum,l)
541             enddo
            enddo
543         if (j > 2) then
                tSTnsr = tSTnsr / (j - 2) ! average
545         endif
            kLoadsurface(k)%kAvS_Tensor(mapNdNum,1:6) = tSTnsr
547         tMatrix(1,1) = kLoadsurface(k)%kDir2(i,1)
            tMatrix(1,2) = kLoadsurface(k)%kDir1(i,1)
549         tMatrix(1,3) = kLoadsurface(k)%kDirN(i,1)
            tMatrix(2,1) = kLoadsurface(k)%kDir2(i,2)
551         tMatrix(2,2) = kLoadsurface(k)%kDir1(i,2)
            tMatrix(2,3) = kLoadsurface(k)%kDirN(i,2)
553         tMatrix(3,1) = kLoadsurface(k)%kDir2(i,3)
            tMatrix(3,2) = kLoadsurface(k)%kDir1(i,3)
555         tMatrix(3,3) = kLoadsurface(k)%kDirN(i,3)
            tgSTnsr(1,1) = kLoadsurface(k)%kAvS_Tensor(i,1)
557         tgSTnsr(2,2) = kLoadsurface(k)%kAvS_Tensor(i,2)
            tgSTnsr(3,3) = kLoadsurface(k)%kAvS_Tensor(i,3)
559         tgSTnsr(1,2) = kLoadsurface(k)%kAvS_Tensor(i,4)
            tgSTnsr(1,3) = kLoadsurface(k)%kAvS_Tensor(i,5)
561         tgSTnsr(2,3) = kLoadsurface(k)%kAvS_Tensor(i,6)
```

```
            tgSTnsr(2,1) = tgSTnsr(1,2)
            tgSTnsr(3,1) = tgSTnsr(1,3)
            tgSTnsr(3,2) = tgSTnsr(2,3)
            call transform(tlSTnsr,tgSTnsr,tMatrix)
            kLoadsurface(k)%klS_Tensor(i,1) = tlSTnsr(1,1)
            kLoadsurface(k)%klS_Tensor(i,2) = tlSTnsr(2,2)
            kLoadsurface(k)%klS_Tensor(i,3) = tlSTnsr(3,3)
            kLoadsurface(k)%klS_Tensor(i,4) = tlSTnsr(1,2)
            kLoadsurface(k)%klS_Tensor(i,5) = tlSTnsr(1,3)
            kLoadsurface(k)%klS_Tensor(i,6) = tlSTnsr(2,3)
        enddo
    enddo
    return
endsubroutine updatSurface

subroutine dload(f, kstep, kinc, time, noel, npt, layer, kspt, coords,&
    jltyp, sname)
    use ShareInfo
    include 'ABA_PARAM.INC'
    dimension array(513),jrray(nprecd,513)
    equivalence (array(1),jrray(1,1))
    dimension time(2), coords(3)
    character*80 sname
    if (kstep == 1) then
        f= 0.D0
    else
        if (jltyp == 21) then ! P1NU
            write(7,*) 'P1NU'
            if (npt == 1) then
                f = kCurrentLoad(kElement(noel,1))
                write(7,*) f,' E ',noel,' N ', kElement(noel,1)
            elseif (npt == 2) then
                f = kCurrentLoad(kElement(noel,2))
                write(7,*) f,' E ',noel,' N ', kElement(noel,2)
            elseif (npt == 3) then
                f = kCurrentLoad(kElement(noel,3))
                write(7,*) f,' E ',noel,' N ', kElement(noel,3)
```

```
599             endif
            elseif (jltyp == 22) then ! P2NU
601             write(7,*) 'P2NU'
                if (npt == 1) then
603                 f = kCurrentLoad(kElement(noel,1))
                    write(7,*) f,' E ',noel,' N ', kElement(noel,1)
605             elseif (npt == 2) then
                    f = kCurrentLoad(kElement(noel,4))
607                 write(7,*) f,' E ',noel,' N ', kElement(noel,4)
                elseif (npt == 3) then
609                 f = kCurrentLoad(kElement(noel,2))
                    write(7,*) f,' E ',noel,' N ', kElement(noel,2)
611             endif
            elseif (jltyp == 23) then ! P2NU
613             write(7,*) 'P3NU'
                if (npt == 1) then
615                 f = kCurrentLoad(kElement(noel,2))
                    write(7,*) f,' E ',noel,' N ', kElement(noel,2)
617             elseif (npt == 2) then
                    f = kCurrentLoad(kElement(noel,4))
619                 write(7,*) f,' E ',noel,' N ', kElement(noel,4)
                elseif (npt == 3) then
621                 f = kCurrentLoad(kElement(noel,3))
                    write(7,*) f,' E ',noel,' N ', kElement(noel,3)
623             endif
            elseif (jltyp == 24) then ! P2NU
625             write(7,*) 'P4NU'
                if (npt == 1) then
627                 f = kCurrentLoad(kElement(noel,3))
                    write(7,*) f,' E ',noel,' N ', kElement(noel,3)
629             elseif (npt == 2) then
                    f = kCurrentLoad(kElement(noel,4))
631                 write(7,*) f,' E ',noel,' N ', kElement(noel,4)
                elseif (npt == 3) then
633                 f = kCurrentLoad(kElement(noel,1))
                    write(7,*) f,' E ',noel,' N ', kElement(noel,1)
635             endif
```

```
        endif
637     endif
        if (abs(f) < 1.0E-20) then
639         f = 0.D0
        endif
641     return
    endsubroutine
643
    subroutine getDload()
645     use ShareInfo
        include 'aba_param.inc'
647     dimension array(513),jrray(nprecd,513),time(2)
        equivalence (array(1),jrray(1,1))
649     double precision:: tau11, tau22,ktLoad
        integer realNdNum, mapNdNum
651     do k = 1,size(kLoadSurface)
            nSrfNum = kLoadSurfaceLabelNumList(k)
653         do i = 1, kNodeSetNds(nSrfNum)
                realNdNum = kNodeSet(nSrfNum)%kNodeList(i)
655             mapNdNum  = kLoadSurface(k)%kNdMap(realNdNum)
                tau11 = ktau0 + kEs * kLoadsurface(k)%klS_Tensor(mapNdNum,1)
657             tau22 = ktau0 + kEs * kLoadsurface(k)%klS_Tensor(mapNdNum,2)
                ktLoad = (tau11*kLoadsurface(k)%kLambda1(mapNdNum)+tau22*
        kLoadsurface(k)%kLambda2(mapNdNum))/kunit
659             if (abs(ktLoad) < 1.0D-20) then
                    ktLoad = 0.D0
661             endif
                kCurrentLoad(realNdNum) = ktLoad
663         enddo
        enddo
665 endsubroutine getDload

667 subroutine urdfil(lstop,lovrwrt,kstep,kinc,dtime,time)
        use ShareInfo
669     include 'aba_param.inc'
        dimension array(513),jrray(nprecd,513),time(2)
671     equivalence (array(1),jrray(1,1))
```

```
      integer i,j,k,l,m,n,mx,knNum,eof
673   integer p1,p2,p3
      integer nSrfNum, facetNum, labelNum
675   integer ndCntr, eleCntr,srfCntr
      integer ndSetCntr, lblCntr, eleSetCntr
677   integer surfaceRefNum
      integer realNdNum, mapNdNum
679   integer realEleNum, mapEleNum
      character*80 Label
681   character*8 aSrfNum,kaNum ! surface corss reference num in character
      logical isSrf
683   double precision,dimension(6) :: tSTnsr! temp strain tensor
      double precision :: ktLoad! temp area
685   double precision,dimension(3,3) :: tgSTnsr! temp strain tensor
      double precision,dimension(3,3) :: tlSTnsr! temp strain tensor
687   double precision,dimension(3,3) :: tMatrix ! transformation matrix
      character*80 :: infokey,kflnm,filename,krtsetName
689   kfunit = 1000+kstep
      if (kstep==1) then
691       call initialAnalysis
          write(*,*) '            Operation in Step ',kstep,'...'
693       call getMesh
          call getSurface
695       call updatSurface(kstep,kinc)
          call getDload
697   else !Operation after Step 1
          write(*,*) '            Operation in Step ',kstep,'...'
699       call updatSurface(kstep,kinc)
          call getDload
701   endif
      return
703 endsubroutine
```

References

N. Aage, N. A. Mortensen, and O. Sigmund. Topology optimization of metallic devices for microwave applications. *International Journal for Numerical Methods in Engineering*, 83(2): 228–248, 2010. ISSN 1097-0207. doi: 10.1002/nme.2837.

Amir Musa Abazari, Seyed Mohsen Safavi, Ghader Rezazadeh, and Luis Guillermo Villanueva. Modelling the size effects on the mechanical properties of micro/nano structures. *Sensors*, 15 (11):28543–28562, 2015. ISSN 1424-8220. doi: 10.3390/s151128543.

Grégoire Allaire, François Jouve, and Anca-Maria Toader. A level-set method for shape optimization. *Comptes Rendus Mathematique*, 334(12):1125–1130, 2002. ISSN 1631-073X. doi: http://dx.doi.org/10.1016/S1631-073X(02)02412-3.

W. McFarland Andrew and S. Colton Jonathan. Role of material microstructure in plate stiffness with relevance to microcantilever sensors. *Journal of Micromechanics and Microengineering*, 15(5):1060, 2005. ISSN 0960-1317.

Boisen Anja, Dohn Søren, Keller Stephan Sylvest, Schmid Silvan, and Tenje Maria. Cantilever-like micromechanical sensors. *Reports on Progress in Physics*, 74(3):036101, 2011. ISSN 0034-4885.

B. Arash and Q. Wang. A review on the application of nonlocal elastic models in modeling of carbon nanotubes and graphenes. *Computational Materials Science*, 51(1):303–313, 2012. ISSN 0927-0256. doi: http://dx.doi.org/10.1016/j.commatsci.2011.07.040.

J. L. Arlett, E. B. Myers, and M. L. Roukes. Comparative advantages of mechanical biosensors. *Nat Nano*, 6(4):203–215, 2011. ISSN 1748-3387.

Patrick Armstrong and Wolfgang Peukert. Size effects in the elastic deformation behavior of metallic nanoparticles. *Journal of Nanoparticle Research*, 14(12):1288, 2012. ISSN 1572-896X. doi: 10.1007/s11051-012-1288-4.

C. Bradford Barber, David P. Dobkin, and Hannu Huhdanpaa. The quickhull algorithm for convex hulls. *ACM Trans. Math. Softw.*, 22(4):469–483, 1996. ISSN 0098-3500. doi: 10.1145/235815.235821.

Klaus-Jurgen Bathe. *Finite element procedures*. Klaus-Jurgen Bathe, 2006.

M. P. Bendsøe. Optimal shape design as a material distribution problem. *Structural optimization*, 1(4):193–202, 1989. ISSN 0934-4373. doi: 10.1007/BF01650949.

M. P. Bendsøe and N. Kikuchi. Generating optimal topologies in structural design using a homogenization method. *Computer Methods in Applied Mechanics and Engineering*, 71(2): 197–224, 1988. doi: 10.1016/0045-7825(88)90086-2.

Martin Philip Bendsoe and Ole Sigmund. *Topology optimization: theory, methods, and applications*. Springer Science and Business Media, 2013. ISBN 3662050862.

Alain Bensoussan, Jacques-Louis Lions, and George Papanicolaou. Asymptotic methods in periodic structures. *Studies in Applied Mathematics*, 5, 1978.

Juergen Biener, Andrea M. Hodge, Alex V. Hamza, Luke M. Hsiung, and Joe H. Satcher. Nanoporous au: A high yield strength material. *Journal of Applied Physics*, 97(2):024301, 2005. doi: doi:http://dx.doi.org/10.1063/1.1832742.

Juergen Biener, Andrea M. Hodge, Joel R. Hayes, Cynthia A. Volkert, Luis A. Zepeda-Ruiz, Alex V. Hamza, and Farid F. Abraham. Size effects on the mechanical behavior of nanoporous au. *Nano Letters*, 6(10):2379–2382, 2006. ISSN 1530-6984. doi: 10.1021/nl061978i.

Akram I. Boukai, Yuri Bunimovich, Jamil Tahir-Kheli, Jen-Kan Yu, William A. Goddard Iii, and James R. Heath. Silicon nanowires as efficient thermoelectric materials. *Nature*, 451 (7175):168–171, 2008. ISSN 0028-0836. doi: 10.1038/nature06458.

R. C. Cammarata and K. Sieradzki. Surface and interface stresses. *Annual Review of Materials Science*, 24(1):215–234, 1994. ISSN 0084-6600. doi: 10.1146/annurev.ms.24.080194.001243.

Robert C. Cammarata. Surface and interface stress effects in thin films. *Progress in Surface Science*, 46(1):1–38, 1994. ISSN 0079-6816. doi: http://dx.doi.org/10.1016/0079-6816(94)90005-1.

Guoxin Cao and Xi Chen. The size effect of nanoindentation on zno nanofilms. *Journal of Applied Physics*, 102(12):123513, 2007. doi: doi:http://dx.doi.org/10.1063/1.2826722.

VJ Challis, AP Roberts, and AH Wilkins. Design of three dimensional isotropic microstructures for maximized stiffness and conductivity. *International Journal of Solids and Structures*, 45(14):4130–4146, 2008.

ChasteJ, EichlerA, MoserJ, CeballosG, RuraliR, and BachtoldA. A nanomechanical mass sensor with yoctogram resolution. *Nat Nano*, 7(5):301–304, 2012. ISSN 1748-3387. doi: 10.1038/nnano.2012.42.

C. Q. Chen and J. Zhu. Bending strength and flexibility of zno nanowires. *Applied Physics Letters*, 90(4):043105, 2007. doi: doi:http://dx.doi.org/10.1063/1.2432289.

C. Q. Chen, Y. Shi, Y. S. Zhang, J. Zhu, and Y. J. Yan. Size dependence of young's modulus in zno nanowires. *Physical Review Letters*, 96(7):075505, 2006a. doi: http://dx.doi.org/10.1103/PhysRevLett.96.075505.

T. Chen, G. J. Dvorak, and C. C. Yu. Size-dependent elastic properties of unidirectional nano-composites with interface stresses. *Acta Mechanica*, 188(1-2):39–54, 2007a. ISSN 0001-5970. doi: 10.1007/s00707-006-0371-2.

Tungyang Chen, Min Sen Chiu, and Chung Ning Weng. Derivation of the generalized young-laplace equation of curved interfaces in nanoscaled solids. *Journal of Applied Physics*, 100(7):074308, 2006b. doi: doi:http://dx.doi.org/10.1063/1.2356094.

Yunxia Chen, Brian L. Dorgan, David N. McIlroy, and D. Eric Aston. On the importance of boundary conditions on nanomechanical bending behavior and elastic modulus determination of silver nanowires. *Journal of Applied Physics*, 100(10):104301, 2006c. doi: doi:http://dx.doi.org/10.1063/1.2382265.

Yunxia Chen, Ian Stevenson, Rebecca Pouy, Lidong Wang, David N McIlroy, Tyler Pounds, M Grant Norton, and D Eric Aston. Mechanical elasticity of vapour-liquid-solid grown gan nanowires. *Nanotechnology*, 18(13):135708, 2007b. ISSN 0957-4484.

E Cosserat and F Cosserat. General mechanics. *Comptes Rendus Hebdomadaires Des Seances De L Academie Des Sciences*, 145:1139–1142, 1907.

G. R. Cowper. The shear coefficient in timoshenko's beam theory. *Journal of Applied Mechanics*, 33(2):335–340, 1966. ISSN 0021-8936. doi: 10.1115/1.3625046.

StÃ©phane Cuenot, Christian FrÃ©tigny, Sophie Demoustier-Champagne, and Bernard Nysten. Surface tension effect on the mechanical properties of nanomaterials measured by atomic force microscopy. *Physical Review B*, 69(16):165410, 2004.

Jiankuai Diao, Ken Gall, and Martin L. Dunn. Surface stress driven reorientation of gold nanowires. *Physical Review B*, 70(7):075413, 2004.

William S Dorn. Automatic design of optimal structures. *Journal de mecanique*, 3:25–52, 1964.

Rui Dou, Bojun Xu, and Brian Derby. High-strength nanoporous silver produced by inkjet printing. *Scripta Materialia*, 63(3):308–311, 2010. ISSN 1359-6462. doi: http://dx.doi.org/10.1016/j.scriptamat.2010.04.021.

C. Durkan and M. E. Welland. Size effects in the electrical resistivity of polycrystalline nanowires. *Physical Review B*, 61(20):14215–14218, 2000.

EichlerA, MoserJ, ChasteJ, ZdrojekM, I. Wilson Rae, and BachtoldA. Nonlinear damping in mechanical resonators made from carbon nanotubes and graphene. *Nat Nano*, 6(6):339–342, 2011. ISSN 1748-3387. doi: 10.1038/nnano.2011.71.

A Cemal Eringen. Linear theory of micropolar elasticity. Report, DTIC Document, 1965.

A. Cemal Eringen. Linear theory of nonlocal elasticity and dispersion of plane waves. *International Journal of Engineering Science*, 10(5):425–435, 1972. ISSN 0020-7225. doi: http://dx.doi.org/10.1016/0020-7225(72)90050-X.

A. Cemal Eringen. On differential equations of nonlocal elasticity and solutions of screw dislocation and surface waves. *Journal of Applied Physics*, 54(9):4703–4710, 1983. doi: doi:http://dx.doi.org/10.1063/1.332803.

A. Cemal Eringen. *Nonlocal Continuum Field Theories*. Springer, New York, 2002.

Mehdi Farsad, Franck J. Vernerey, and Harold S. Park. An extended finite element/level set method to study surface effects on the mechanical behavior and properties of nanomaterials. *International Journal for Numerical Methods in Engineering*, 84(12):1466–1489, 2010. ISSN 1097-0207. doi: 10.1002/nme.2946.

X. Q. Feng, R. Xia, X. Li, and B. Li. Surface effects on the elastic modulus of nanoporous materials. *Applied Physics Letters*, 94(1):011916, 2009. ISSN 0003-6951. doi: Artn011916Doi10.1063/1.3067999.

N. A. Fleck, G. M. Muller, M. F. Ashby, and J. W. Hutchinson. Strain gradient plasticity: Theory and experiment. *Acta Metallurgica et Materialia*, 42(2):475–487, 1994. ISSN 0956-7151. doi: http://dx.doi.org/10.1016/0956-7151(94)90502-9.

NA Fleck and JW Hutchinson. A reformulation of strain gradient plasticity. *Journal of the Mechanics and Physics of Solids*, 49(10):2245–2271, 2001. ISSN 0022-5096.

Wei Gao, Shouwen Yu, and Ganyun Huang. Finite element characterization of the size-dependent mechanical behaviour in nanosystems. *Nanotechnology*, 17(4):1118, 2006. ISSN 0957-4484.

Khashayar Babaei Gavan, Hidde JR Westra, Emile WJM van der Drift, Warner J Venstra, and Herre SJ van der Zant. Size-dependent effective young's modulus of silicon nitride cantilevers. *Applied Physics Letters*, 94(23):233108, 2009. ISSN 0003-6951.

J.M. Gere and S. Timoshenko. *Mechanics of materials*. PWS-KENT Pub. Co., 1990. ISBN 9780534921743.

Josiah Willard Gibbs, Henry Andrews Bumstead, and William Raymond Longley. *The collected works of J. Willard Gibbs*, volume 1. Longmans, Green and Company, 1928.

Leonid V. Gibiansky. Bounds on the effective moduli of composite materials. Technical report, Princeton University, 1993.

L. J. Gibson and M. F. Ashby. The mechanics of three-dimensional cellular materials. *Proceedings of the Royal Society of London A: Mathematical, Physical and Engineering Sciences*, 382(1782):43–59, 1982. doi: 10.1098/rspa.1982.0088.

L.J. Gibson and M.F. Ashby. *Cellular Solids: Structure and Properties*. Cambridge University Press, 1999. ISBN 9780521499118.

T. Goudarzi, R. Avazmohammadi, and R. Naghdabadi. Surface energy effects on the yield strength of nanoporous materials containing nanoscale cylindrical voids. *Mechanics of Materials*, 42(9):852–862, 2010. ISSN 0167-6636. doi: http://dx.doi.org/10.1016/j.mechmat.2010.07.006.

M. E. Gurtin, J. Weissmuller, and F. Larche. A general theory of curved deformable interfaces in solids at equilibrium. *Philosophical Magazine A*, 78(5):1093–1109, 1998. ISSN 0141-8610. doi: 10.1080/01418619808239977.

MortonE Gurtin and A. Ian Murdoch. A continuum theory of elastic material surfaces. *Archive for Rational Mechanics and Analysis*, 57(4):291–323, 1975. ISSN 0003-9527. doi: 10.1007/BF00261375.

T. Hagishita and M. Ohsaki. Topology optimization of trusses by growing ground structure method. *Structural and Multidisciplinary Optimization*, 37(4):377–393, 2009. ISSN 1615-1488. doi: 10.1007/s00158-008-0237-4. URL `http://dx.doi.org/10.1007/s00158-008-0237-4`.

M. S. Hanay, KelberS, A. K. Naik, ChiD, HentzS, E. C. Bullard, ColinetE, DuraffourgL, and M. L. Roukes. Single-protein nanomechanical mass spectrometry in real time. *Nat Nano*, 7 (9):602–608, 2012. ISSN 1748-3387. doi: 10.1038/nnano.2012.119.

Zvi Hashin and Shmuel Shtrikman. A variational approach to the theory of the elastic behaviour of multiphase materials. *Journal of the Mechanics and Physics of Solids*, 11(2): 127–140, 1963. ISSN 0022-5096.

B Hassani and E Hinton. A review of homogenization and topology opimization ii—analytical and numerical solution of homogenization equations. *Computers and structures*, 69(6): 719–738, 1998a.

B Hassani and E Hinton. A review of homogenization and topology optimization iii—topology optimization using optimality criteria. *Computers and structures*, 69(6):739–756, 1998b.

Behrooz Hassani and Ernest Hinton. A review of homogenization and topology optimization i—homogenization theory for media with periodic structure. *Computers and Structures*, 69 (6):707–717, 1998c.

J. He and C. M. Lilley. Surface effect on the elastic behavior of static bending nanowires. *Nano Letters*, 8(7):1798–1802, 2008. ISSN 1530-6984. doi: Doi10.1021/Nl0733233.

Jin He and CarmenM Lilley. The finite element absolute nodal coordinate formulation incorporated with surface stress effect to model elastic bending nanowires in large deformation. *Computational Mechanics*, 44(3):395–403, 2009. ISSN 0178-7675. doi: 10.1007/s00466-009-0380-9.

William S Hemp. *Optimum structures*. Clarendon Press, 1973.

A. M. Hodge, J. Biener, J. R. Hayes, P. M. Bythrow, C. A. Volkert, and A. V. Hamza. Scaling equation for yield strength of nanoporous open-cell foams. *Acta Materialia*, 55(4):1343–1349, 2007. ISSN 1359-6454. doi: http://dx.doi.org/10.1016/j.actamat.2006.09.038.

X. Huang and Y. M. Xie. Convergent and mesh-independent solutions for the bi-directional evolutionary structural optimization method. *Finite Elements in Analysis and Design*, 43(14): 1039–1049, 2007. doi: 10.1016/j.finel.2007.06.006.

X. Huang and Y. M. Xie. Bi-directional evolutionary topology optimization of continuum structures with one or multiple materials. *Computational Mechanics*, 43(3):393–401, 2009. ISSN 0178-7675. doi: DOI10.1007/s00466-008-0312-0.

X. Huang and Yi-Min Xie. Evolutionary topology optimization of continuum structures including design-dependent self-weight loads. *Finite Elements in Analysis and Design*, 47(8): 942–948, 2011. ISSN 0168874X. doi: 10.1016/j.finel.2011.03.008.

X. Huang, A. Radman, and Y. M. Xie. Topological design of microstructures of cellular materials for maximum bulk or shear modulus. *Computational Materials Science*, 50(6): 1861–1870, 2011. ISSN 0927-0256. doi: http://dx.doi.org/10.1016/j.commatsci.2011.01.030.

X. Huang, Yi-Min Xie, B. Jia, Q. Li, and S. W. Zhou. Evolutionary topology optimization of periodic composites for extremal magnetic permeability and electrical permittivity. *Structural and Multidisciplinary Optimization*, 46(3):385–398, 2012. ISSN 1615-147X 1615-1488. doi: 10.1007/s00158-012-0766-8.

X. Huang, S. W. Zhou, Yi-Min Xie, and Q. Li. Topology optimization of microstructures of cellular materials and composites for macrostructures. *Computational Materials Science*, 67: 397–407, 2013. ISSN 09270256. doi: 10.1016/j.commatsci.2012.09.018.

X. Huang, Y. Li, S. W. Zhou, and Yi-Min Xie. Topology optimization of compliant mechanisms with desired structural stiffness. *Engineering Structures*, 79:13–21, 2014. ISSN 01410296. doi: 10.1016/j.engstruct.2014.08.008.

Xiaodong Huang and Y. M. Xie. *Evolutionary Topology Optimization of Continuum Structures: Methods and Applications*. Willey, 2010. ISBN 978-0-470-74653-0.

Xiaodong Huang, Shiwei Zhou, Guangyong Sun, Guangyao Li, and Yi-Min Xie. Topology optimization for microstructures of viscoelastic composite materials. *Computer Methods in Applied Mechanics and Engineering*, 283:503–516, 2015. ISSN 00457825. doi: 10.1016/j.cma.2014.10.007.

J. S. Jensen and O. Sigmund. Topology optimization for nano-photonics. *Laser and Photonics Reviews*, 5(2):308–321, 2011. ISSN 1863-8899. doi: 10.1002/lpor.201000014.

G. Y. Jing, H. L. Duan, X. M. Sun, Z. S. Zhang, J. Xu, Y. D. Li, J. X. Wang, and D. P. Yu. Surface effects on elastic properties of silver nanowires: Contact atomic-force microscopy. *Physical Review B*, 73(23):235409, 2006.

Y. Jung, K. T. Chu, and S. Torquato. A variational level set approach for surface area minimization of triply-periodic surfaces. *J. Comput. Phys.*, 223(2):711–730, 2007. ISSN 0021-9991. doi: 10.1016/j.jcp.2006.10.007.

RB Karabalin, XL Feng, and ML Roukes. Parametric nanomechanical amplification at very high frequency. *Nano letters*, 9(9):3116–3123, 2009. ISSN 1530-6984.

Vadim Komkov, Kyung K Choi, and Edward J Haug. *Design sensitivity analysis of structural systems*, volume 177. Academic press, 1986.

Michael J Lachut and John E Sader. Effect of surface stress on the stiffness of cantilever plates: Influence of cantilever geometry. *Applied Physics Letters*, 95(19):193505, 2009. ISSN 0003-6951.

Michael J Lachut and John E Sader. Effect of surface stress on the stiffness of thin elastic plates and beams. *Physical Review B*, 85(8):085440, 2012.

R Lakes. Experimental micro mechanics methods for conventional and negative poisson's ratio cellular solids as cosserat continua. *Journal of Engineering Materials and Technology*, 113(1):148–155, 1991. ISSN 0094-4289.

D. C. C. Lam, F. Yang, A. C. M. Chong, J. Wang, and P. Tong. Experiments and theory in strain gradient elasticity. *Journal of the Mechanics and Physics of Solids*, 51(8):1477–1508, 2003. ISSN 0022-5096. doi: http://dx.doi.org/10.1016/S0022-5096(03)00053-X.

Cornelius Lanczos. *The variational principles of mechanics*, volume 4. Courier Corporation, 1970. ISBN 0486650677.

Pierre Simon Laplace. *Traité de mécanique céleste/par PS Laplace...; tome premier [-quatrieme]*, volume 4. de l'Imprimerie de Crapelet, 1805.

Dongyun Lee, Xiaoding Wei, Manhong Zhao, Xi Chen, Seong C. Jun, James Hone, and Jeffry W. Kysar. Plastic deformation in nanoscale gold single crystals and open-celled nanoporous gold. *Modelling and Simulation in Materials Science and Engineering*, 15(1): S181, 2007a. ISSN 0965-0393.

Kyumin Lee, Branimir Lukić, Arnaud Magrez, Jin Won Seo, G. Andrew D. Briggs, Andrzej J. Kulik, and László Forró. Diameter-dependent elastic modulus supports the metastable-catalyst growth of carbon nanotubes. *Nano Letters*, 7(6):1598–1602, 2007b. ISSN 1530-6984. doi: 10.1021/nl070502b.

Xian-Fang Li, Hua Zhang, and Kang Yong Lee. Dependence of young's modulus of nanowires on surface effect. *International Journal of Mechanical Sciences*, 81:120–125, 2014. ISSN 0020-7403. doi: http://dx.doi.org/10.1016/j.ijmecsci.2014.02.018.

Yang Li, Xiaodong Huang, and Shiwei Zhou. Topological design of cellular phononic band gap crystals. *Materials*, 9(3):186, 2016. ISSN 1996-1944.

Jie Lian, Seok-Woo Lee, Lorenzo Valdevit, Michael I Baskes, and Julia R Greer. Emergence of film-thickness-and grain-size-dependent elastic properties in nanocrystalline thin films. *Scripta Materialia*, 68(5):261–264, 2013. ISSN 1359-6462.

Sun Liang, P. S. Han Ray, Wang Jun, and C. T. Lim. Modeling the size-dependent elastic properties of polymeric nanofibers. *Nanotechnology*, 19(45):455706, 2008. ISSN 0957-4484.

O. Lourie and H. D. Wagner. Evaluation of young's modulus of carbon nanotubes by micro-raman spectroscopy. *Journal of Materials Research*, 13(09):2418–2422, 1998. ISSN 2044-5326. doi: doi:10.1557/JMR.1998.0336.

Dingjie Lu, Yi Min Xie, Qing Li, Xiaodong Huang, and Shiwei Zhou. Towards ultra-stiff materials: Surface effects on nanoporous materials. *Applied Physics Letters*, 105(10):101903, 2014. doi: doi:http://dx.doi.org/10.1063/1.4895582.

Dingjie Lu, Yi Min Xie, Qing Li, Xiaodong Huang, and Shiwei Zhou. Investigating size effects of complex nanostructures through young-laplace equation and finite element analysis. *Journal of Applied Physics*, 118(20):204301, 2015. doi: doi:http://dx.doi.org/10.1063/1.4935819.

Marcel Lucas, Ken Gall, and Elisa Riedo. Tip size effects on atomic force microscopy nanoindentation of a gold single crystal. *Journal of Applied Physics*, 104(11):113515, 2008. doi: doi:http://dx.doi.org/10.1063/1.3039511.

Branimir Lukic, Jin Won Seo, Revathi R. Bacsa, Sandrine Delpeux, François Béguin, Geoffroy Bister, Antonio Fonseca, Janos B. Nagy, András Kis, Sylvia Jeney, Andrzej J. Kulik, and László Forró. Catalytically grown carbon nanotubes of small diameter have a high young's modulus. *Nano Letters*, 5(10):2074–2077, 2005. ISSN 1530-6984. doi: 10.1021/nl051034d.

Anant Mathur and Jonah Erlebacher. Size dependence of effective young's modulus of nanoporous gold. *Applied Physics Letters*, 90(6):–, 2007. doi: doi:http://dx.doi.org/10.1063/1.2436718.

Fei Meng, Xiaodong Huang, and Baohua Jia. Bi-directional evolutionary optimization for photonic band gap structures. *Journal of Computational Physics*, 302:393–404, 2015. ISSN 0021-9991. doi: http://dx.doi.org/10.1016/j.jcp.2015.09.010.

Lucas R. Meza, Satyajit Das, and Julia R. Greer. Strong, lightweight, and recoverable three-dimensional ceramic nanolattices. *Science*, 345(6202):1322–1326, 2014. doi: 10.1126/science.1255908.

Changwen Mi, Sukky Jun, Demitris A. Kouris, and Sung Youb Kim. Atomistic calculations of interface elastic properties in noncoherent metallic bilayers. *Physical Review B*, 77(7):075425, 2008.

JC Michel, H Moulinec, and P Suquet. Effective properties of composite materials with periodic microstructure: a computational approach. *Computer methods in applied mechanics and engineering*, 172(1):109–143, 1999.

R. E. Miller and V. B. Shenoy. Size-dependent elastic properties of nanosized structural elements. *Nanotechnology*, 11(3):139–147, 2000. ISSN 0957-4484. doi: Doi10.1088/0957-4484/11/3/301.

Raymond David Mindlin. Micro-structure in linear elasticity. *Archive for Rational Mechanics and Analysis*, 16(1):51–78, 1964. ISSN 0003-9527.

Amir K. Miri, Reza Avazmohammadi, and Fuqian Yang. Effect of surface stress on the deformation of an elastic half-plane containing a nano-cylindrical hole under a surface loading. *Journal of Computational and Theoretical Nanoscience*, 8(2):231–236, 2011. doi: 10.1166/jctn.2011.1683.

Nicolas Moes, John Dolbow, and Ted Belytschko. A finite element method for crack growth without remeshing. *International Journal for Numerical Methods in Engineering*, 46(1):131–150, 1999. ISSN 1097-0207. doi: 10.1002/(SICI)1097-0207(19990910)46:1⟨131::AID-NME726⟩3.0.CO;2-J.

MoserJ, GuttingerJ, EichlerA, M. J. Esplandiu, D. E. Liu, M. I. Dykman, and BachtoldA. Ultrasensitive force detection with a nanotube mechanical resonator. *Nat Nano*, 8(7):493–496, 2013. ISSN 1748-3387. doi: 10.1038/nnano.2013.97.

Sara G Nilsson, X Borrise, and Lars Montelius. Size effect on young's modulus of thin chromium cantilevers. *Applied physics letters*, 85:3555, 2004. ISSN 0003-6951.

Makoto Ohsaki. *Optimization of finite dimensional structures*. CRC Press, 2016. ISBN 143982004X.

Atsuyuki Okabe, Barry Boots, Kokichi Sugihara, and Sung Nok Chiu. *Spatial tessellations: concepts and applications of Voronoi diagrams*, volume 501. John Wiley Sons, 2009. ISBN 047031785X.

Stanley Osher and James A. Sethian. Fronts propagating with curvature-dependent speed: Algorithms based on hamilton-jacobi formulations. *Journal of Computational Physics*, 79(1): 12–49, 1988. ISSN 0021-9991. doi: http://dx.doi.org/10.1016/0021-9991(88)90002-2.

Harold S. Park and Patrick A. Klein. A surface cauchy-born model for silicon nanostructures. *Computer Methods in Applied Mechanics and Engineering*, 197(41–42):3249–3260, 2008. ISSN 0045-7825. doi: http://dx.doi.org/10.1016/j.cma.2007.12.004.

Bei Peng, Mark Locascio, Peter Zapol, Shuyou Li, Steven L. Mielke, George C. Schatz, and Horacio D. Espinosa. Measurements of near-ultimate strength for multiwalled carbon nanotubes and irradiation-induced crosslinking improvements. *Nat. Nano.*, 3(10):626–631, 2008. ISSN 1748-3387.

Valerio Pini, Javier Tamayo, Eduardo Gil-Santos, Daniel Ramos, Priscila Kosaka, Hien-Duy Tong, Cees van Rijn, and Montserrat Calleja. Shedding light on axial stress effect on resonance frequencies of nanocantilevers. *Acs Nano*, 5(6):4269–4275, 2011. ISSN 1936-0851.

Philippe Poncharal, ZL Wang, Daniel Ugarte, and Walt A De Heer. Electrostatic deflections and electromechanical resonances of carbon nanotubes. *science*, 283(5407):1513–1516, 1999. ISSN 0036-8075.

Charles P Poole Jr and Frank J Owens. *Introduction to nanotechnology*. John Wiley Sons, 2003. ISBN 0471079359.

S. C. Pradhan and T. Murmu. Small scale effect on the buckling analysis of single-layered graphene sheet embedded in an elastic medium based on nonlocal plate theory. *Physica E: Low-dimensional Systems and Nanostructures*, 42(5):1293–1301, 2010. ISSN 1386-9477. doi: http://dx.doi.org/10.1016/j.physe.2009.10.053.

O. M. Querin, G. P. Steven, and Y. M. Xie. Evolutionary structural optimisation (eso) using a bidirectional algorithm. *Engineering Computations (Swansea, Wales)*, 15(8):1031–1048, 1998.

Xia Re, Li Xide, Qin Qinghua, Liu Jianlin, and Feng Xi-Qiao. Surface effects on the mechanical properties of nanoporous materials. *Nanotechnology*, 22(26):265714, 2011. ISSN 0957-4484.

H. Rösner, S. Parida, D. Kramer, C. A. Volkert, and J. Weissmüller. Reconstructing a nanoporous metal in three dimensions: An electron tomography study of dealloyed gold leaf. *Advanced Engineering Materials*, 9(7):535–541+519, 2007. doi: 10.1002/adem.200700063.

Jean Paul Salvetat, G. Andrew D. Briggs, Jean Marc Bonard, Revathi R. Bacsa, Andrzej J. Kulik, Thomas Stöckli, Nancy A. Burnham, and László Forró. Elastic and shear moduli of single-walled carbon nanotube ropes. *Physical Review Letters*, 82(5):944–947, 1999.

T. A. Schaedler, A. J. Jacobsen, A. Torrents, A. E. Sorensen, J. Lian, J. R. Greer, L. Valdevit, and W. B. Carter. Ultralight metallic microlattices. *Science*, 334(6058):962–965, 2011. ISSN 0036-8075. doi: DOI10.1126/science.1211649.

S Schmid and C Hierold. Damping mechanisms of single-clamped and prestressed double-clamped resonant polymer microbeams. *Journal of Applied Physics*, 104(9):093516, 2008. ISSN 0021-8979.

A. Sears and R. C. Batra. Macroscopic properties of carbon nanotubes from molecular-mechanics simulations. *Physical Review B*, 69(23):235406, 2004.

A.A. Shabana. *An Absolute Nodal Coordinate Formulation for the Large Rotation and Deformation Analysis of Flexible Bodies*. Department of Mechanical and Industrial Engineering, University of Illinois at Chicago, 1996.

P. Sharma, S. Ganti, and N. Bhate. Effect of surfaces on the size-dependent elastic state of nano-inhomogeneities. *Applied Physics Letters*, 82(4):535–537, 2003. doi: doi:http://dx.doi.org/10.1063/1.1539929.

Vijay B. Shenoy. Atomistic calculations of elastic properties of metallic fcc crystal surfaces. *Physical Review B*, 71(9):094104, 2005.

Min Kyoon Shin, Sun I. Kim, Seon Jeong Kim, Sung-Kyoung Kim, Haiwon Lee, and Geoffrey M. Spinks. Size-dependent elastic modulus of single electroactive polymer nanofibers. *Applied Physics Letters*, 89(23):231929, 2006. doi: doi:http://dx.doi.org/10.1063/1.2402941.

O. Sigmund. A 99 line topology optimization code written in matlab. *Structural and Multidisciplinary Optimization*, 21(2):120–127, 2001. ISSN 1615-147X.

Ole Sigmund. Tailoring materials with prescribed elastic properties. *Mechanics of Materials*, 20(4):351–368, 1995. ISSN 0167-6636. doi: http://dx.doi.org/10.1016/0167-6636(94)00069-7.

Ole Sigmund and Kristian Hougaard. Geometric properties of optimal photonic crystals. *Physical Review Letters*, 100(15):153904, 2008.

G Stan, CV Ciobanu, PM Parthangal, and RF Cook. Diameter-dependent radial and tangential elastic moduli of zno nanowires. *Nano Letters*, 7(12):3691–3697, 2007. ISSN 1530-6984.

N. A. Stelmashenko, M. G. Walls, L. M. Brown, and Yu V. Milman. Microindentations on w and mo oriented single crystals: An stm study. *Acta Metallurgica et Materialia*, 41(10):2855–2865, 1993. ISSN 0956-7151. doi: http://dx.doi.org/10.1016/0956-7151(93)90100-7.

Stefan Sturm, Shiwei Zhou, Yiu-Wing Mai, and Qing Li. On stiffness of scaffolds for bone tissue engineering-a numerical study. *Journal of Biomechanics*, 43(9):1738–1744, 2010. ISSN 0021-9290. doi: http://dx.doi.org/10.1016/j.jbiomech.2010.02.020.

C Sun, N Fang, DM Wu, and X Zhang. Projection micro-stereolithography using digital micro-mirror dynamic mask. *Sensors and Actuators A:Physical*, 121(1):113–120, 2005. ISSN 0924-4247.

Liang Sun, Ray PS Han, Jun Wang, and CT Lim. Modeling the size-dependent elastic properties of polymeric nanofibers. *Nanotechnology*, 19(45):455706, 2008. ISSN 0957-4484.

Dassault Systemes. Abaqus, 2013.

Thomas W. Tombler, Chongwu Zhou, Leo Alexseyev, Jing Kong, Hongjie Dai, Lei Liu, C. S. Jayanthi, Meijie Tang, and Shi Yu Wu. Reversible electromechanical characteristics of carbon nanotubes under local-probe manipulation. *Nature*, 405(6788):769–772, 2000. ISSN 0028-0836.

Scott S Verbridge, Daniel Finkelstein Shapiro, Harold G Craighead, and Jeevak M Parpia. Macroscopic tuning of nanomechanics: substrate bending for reversible control of frequency and quality factor of nanostring resonators. *Nano Letters*, 7(6):1728–1735, 2007. ISSN 1530-6984.

L. G Villanueva and S. Schmid. Evidence of surface loss as ubiquitous limiting damping mechanism in sin micro- and nanomechanical resonators. *Physical Review Letters*, 113(22): 227201, 2014.

L. G. Villanueva, R. B. Karabalin, M. H. Matheny, D. Chi, J. E. Sader, and M. L. Roukes. Nonlinearity in nanomechanical cantilevers. *Physical Review B*, 87(2):024304, 2013.

C. A. Volkert, E. T. Lilleodden, D. Kramer, and J. Weissmuller. Approaching the theoretical strength in nanoporous au. *Applied Physics Letters*, 89(6):–, 2006. doi: doi:http://dx.doi.org/10.1063/1.2240109.

C. M. Wang, Y. Y. Zhang, and X. Q. He. Vibration of nonlocal timoshenko beams. *Nanotechnology*, 18(10):105401, 2007. ISSN 0957-4484.

Fengwen Wang, Jakob S. Jensen, and Ole Sigmund. Robust topology optimization of photonic crystal waveguides with tailored dispersion properties. *Journal of the Optical Society of America B*, 28(3):387–397, 2011. doi: 10.1364/JOSAB.28.000387.

Gang-Feng Wang and Xi-Qiao Feng. Effects of surface elasticity and residual surface tension on the natural frequency of microbeams. *Applied Physics Letters*, 90(23):231904, 2007. ISSN 0003-6951.

Jian-Shan Wang, Xi-Qiao Feng, Gang-Feng Wang, and Shou-Wen Yu. Twisting of nanowires induced by anisotropic surface stresses. *Applied Physics Letters*, 92(19):–, 2008. doi: doi:http://dx.doi.org/10.1063/1.2928221.

Lifeng Wang and Haiyan Hu. Flexural wave propagation in single-walled carbon nanotubes. *Physical Review B*, 71(19):195412, 2005.

Jorg Weissmuller, Roger C. Newman, Hai Jun Jin, Andrea M. Hodge, and Jeffrey W. Kysar. Nanoporous metals by alloy corrosion: Formation and mechanical properties. *MRS Bulletin*, 34(08):577–586, 2009.

Wikipedia. Curvature — wikipedia, the free encyclopedia, 2016.

Carl W Wilmsen, Erik G Thompson, and George H Meissner. Buckling of thermally-grown sio 2 thin films. *IEEE Transactions on Electron Devices*, 19(1):122–122, 1972. ISSN 0018-9383.

DJ Wilson, CA Regal, SB Papp, and HJ Kimble. Cavity optomechanics with stoichiometric sin films. *Physical review letters*, 103(20):207204, 2009.

Bin Wu, Andreas Heidelberg, and John J Boland. Mechanical properties of ultrahigh-strength gold nanowires. *Nature materials*, 4(7):525–529, 2005. ISSN 1476-1122.

R. Xia, X. Q. Feng, and G. F. Wang. Effective elastic properties of nanoporous materials with hierarchical structure. *Acta Materialia*, 59(17):6801–6808, 2011. ISSN 1359-6454. doi: DOI10.1016/j.actamat.2011.07.039.

Y. M. Xie and G. P. Steven. A simple evolutionary procedure for structural optimization. *Computers & Structures*, 49(5):885–896, 1993. ISSN 0045-7949. doi: http://dx.doi.org/10.1016/0045-7949(93)90035-C.

Yi Min Xie and Grant P Steven. *Basic evolutionary structural optimization*. Springer, 1997. ISBN 1447112504.

Zheng Xiu-Peng, Cao Yan-Ping, Li Bo, Feng Xi-Qiao, and Wang Gang-Feng. Surface effects in various bending-based test methods for measuring the elastic property of nanowires. *Nanotechnology*, 21(20):205702, 2010. ISSN 0957-4484.

Thomas Young. An essay on the cohesion of fluids. *Philosophical Transactions of the Royal Society of London*, 95:65–87, 1805. doi: 10.1098/rstl.1805.0005.

M.F. Yu, Oleg Lourie, Mark J. Dyer, Katerina Moloni, Thomas F. Kelly, and Rodney S. Ruoff. Strength and breaking mechanism of multiwalled carbon nanotubes under tensile load. *Science*, 287(5453):637–640, 2000. doi: 10.1126/science.287.5453.637.

J. Yvonnet, H. Le Quang, and Q. C. He. An xfem/level set approach to modelling surface/interface effects and to computing the size-dependent effective properties of nanocomposites. *Computational Mechanics*, 42(1):119–131, 2008. ISSN 0178-7675. doi: 10.1007/s00466-008-0241-y.

H. F. Zhan and Y. T. Gu. Modified beam theories for bending properties of nanowires considering surface/intrinsic effects and axial extension effect. *Journal of Applied Physics*, 111(8):084305, 2012. doi: doi:http://dx.doi.org/10.1063/1.3703673.

Tong-Yi Zhang, Miao Luo, and Wing Kin Chan. Size-dependent surface stress, surface stiffness, and young's modulus of hexagonal prism [111] β-sic nanowires. *Journal of Applied Physics*, 103(10):–, 2008. doi: doi:http://dx.doi.org/10.1063/1.2927453.

Y. Q. Zhang, G. R. Liu, and X. Y. Xie. Free transverse vibrations of double-walled carbon nanotubes using a theory of nonlocal elasticity. *Physical Review B*, 71(19):195404, 2005.

Y. Y. Zhang, C. M. Wang, W. H. Duan, Y. Xiang, and Z. Zong. Assessment of continuum mechanics models in predicting buckling strains of single-walled carbon nanotubes. *Nanotechnology*, 20(39):395707, 2009. ISSN 0957-4484.

Xiaoyu Zheng, Howon Lee, Todd H. Weisgraber, Maxim Shusteff, Joshua DeOtte, Eric B. Duoss, Joshua D. Kuntz, Monika M. Biener, Qi Ge, Julie A. Jackson, Sergei O. Kucheyev, Nicholas X. Fang, and Christopher M. Spadaccini. Ultralight, ultrastiff mechanical metamaterials. *Science*, 344(6190):1373–1377, 2014. doi: 10.1126/science.1252291.

Shiwei Zhou and Qing Li. Computational design of multi-phase microstructural materials for extremal conductivity. *Computational Materials Science*, 43(3):549–564, 2008a.

Shiwei Zhou and Qing Li. A microstructure diagram for known bounds in conductivity. *Journal of Materials Research*, 23(03):798–811, 2008b.

Olgierd Cecil Zienkiewicz, Robert Leroy Taylor, Olgierd Cecil Zienkiewicz, and Robert Lee Taylor. *The finite element method*, volume 3. McGraw-hill London, 1977.

Zhi Hao Zuo, Xiaodong Huang, Jian Hua Rong, and Yi-Min Xie. Multi-scale design of composite materials and structures for maximum natural frequencies. *Materials & Design*, 51: 1023–1034, 2013. ISSN 02613069. doi: 10.1016/j.matdes.2013.05.014.